Multiloop functional renormalization group in the Keldysh formalism — A study of the single-impurity Anderson model

Santiago Aguirre Lamus

Munich 2020

Multiloop functional renormalization group in the Keldysh formalism — A study of the single-impurity Anderson model

Santiago Aguirre Lamus

Master's Thesis for the TMP-Program
at the Faculty of Physics
of the Ludwig–Maximilians–Universität
München

authored by
Santiago Aguirre Lamus
of Bogota, Colombia

Munich, the 14$^{\text{th}}$ of October 2020

Advisor: Prof. Jan von Delft
2nd corrector: Prof. Matthias Punk

Abstract

A major challenge for studies of strongly interacting systems is the computation of dynamical correlators as a function of real frequencies (as opposed to imaginary frequencies, requiring analytical continuation). One strategy for achieving this goal is the multiloop functional Renormalization Group (mfRG) [1, 2], formulated within the real-frequency Keldysh formalism. mfRG is a generalization of standard 1-loop fRG, a popular RG scheme which has been applied to a wide range of interacting condensed matter systems. mfRG overcomes numerous technical limitations of 1-loop fRG, but has so far been employed only in the imaginary-frequency Matsubara formalism [3, 4].

In this work we perform the first real-frequency mfRG calculations of the full real-frequency dependence of the four-point vertex of the single-impurity Anderson model (SIAM). This model has trivial position or momentum dependence, allowing us to develop the methodology necessary for a detailed treatment of the frequency dependence of the self-energy and four-point vertex. The main technical challenge was to write a Keldysh-mfRG code capable of accurately and efficiently track the evolution of this frequency dependence during the RG flow.

We make use of the frequency parametrization and diagrammatic decomposition of the vertex of Ref. [5] to be able to reduce the four-point vertex to its independent components. We present results for the conventional fRG using only the $\mathcal{K}_1$ class of diagrams, for the static-feedback approximation as used in Ref. [6] and for flows with the $\mathcal{K}_2$ class of diagrams up to 2-loop order. As these are only preliminary results, we do not include the $\mathcal{K}_3$ class.

We implement a hybridization flow for the SIAM. For it, we are able to stably reach interaction strengths of $U/\Delta = 5.6$ ($U/\Gamma = 2.8$) for all kinds of flows. Results agree well with those provided by NRG, our benchmark method. We see an improvement in the fulfillment of Ward identities and the solution of the equations of the parquet formalism.

Our method allows us to flexibly perform both equilibrium and non-equilibrium calculations at essentially no extra expense. We hence present results for variable bias voltages. We also explore the behavior of the model at different temperatures. Our work extends that of Ref. [7], which had studied the SIAM with standard 1-loop fRG in the Keldysh formalism. We elucidate the effect of and necessity for including higher loop orders. Our work sets the stage for future Keldysh-mfRG studies of richer models, involving nontrivial behavior as functions of both frequency and momentum.

Acknowledgments

First of all, I would like to thank Jan von Delft for his supervision of this thesis. I profited greatly from his attentiveness to detail and his great "hands-off" approach to supervising. Each and every one of his comments were always constructive and aimed not only at improving the quality of this work but also at helping me become a better researcher.

I also would like to express my deepest gratitude to Elias Walter, with whom I worked side-by-side on many aspects of this work. Without his patience, support and willingness to help and guide me with the more technical aspects, this thesis would have been a much bigger challenge. A very special thank you goes also to Fabian Kugler, specially for his always remarkably insightful comments in our discussions on physics and programming. I learned a lot thanks to him. I am extremely grateful to the three aforementioned people for proofreading this work and sparing no constructive feedback.

I also thank Julian Thönniß for our discussions on the caveats and difficulties of implementing an mfRG code. His always cheerful mood helped me stay motivated and focused when the code was not working. We acknowledge his help with data formatting and HDF5.

I am also deeply thankful for my colleagues of Office A415, David Moser, Gianni del Bimbo and Felix Palm, for the rich physical discussions as well as non-physics related conversations had and enjoyed in our office.

I am thankful to the Konrad Adenauer Foundation for their support and funding of my studies.

Last but not least, I am grateful to my family and friends, both here and back home, for their continuous support.

Gracias.

Contents

List of Figures

List of Tables

Chapter 1

Introduction

Strongly correlated systems in condensed matter physics are of very high interest due to the diverse behaviors they show. Electron-electron interactions give rise to a zoo of different systems with a plethora of characteristics as are magnetically frustrated systems, topological phases, spin liquids, superconducting systems and many-body localized states. Of particular interest in the field is the calculation of dynamical quantities, like the excitation spectrum or the dynamical susceptibility of a given system, as functions of real frequencies.

A popular tool for tackling interacting systems is the functional renormalization group [8, 9, 10]. This is a widely used renormalization scheme with some technical advantages over less mathematically formal methods as e.g. the Wilsonian method [11, 12]. The violation of regulator independence and of conservation laws are however some major setbacks of this method. The newly developed multiloop functional renormalization group [1, 2], overcomes these two issues, which makes it an attractive tool to study and the main focus of the present work.

Many of the modern techniques are based on the Matsubara formalism, a very powerful tool to describe systems in thermodynamic equilibrium. However, the usage of this formalism poses a very fundamental problem with the analytic continuation of the imaginary-time functions to real-time dynamical quantities, as this is an ill-defined numerical problem. This means it cannot be used to treat systems outside of the very special case of thermodynamic equilibrium. In contrast, the Keldysh formalism [13, 14] is formulated on a real-time contour, which offers a way to overcome this problem of analytical continuation, while simultaneously providing a framework for equilibrium and non-equilibrium calculations alike.

In this work, we seek to study the applicability of the multiloop functional renormalization group within the Keldysh formalism. For this purpose, we choose to study Anderson's single-impurity model [15], which has been thoroughly studied before [12, 16, 17, 18]. This allows us to have a perfect testing ground for our method, as there are tools readily available for benchmarking.

We begin this work with a review and recap of the relevant theoretical tools needed to fulfill our goal. This includes a thorough revision of the functional renormalization group

as well as an introduction to the Keldysh formalism. We also show how the conventional fRG can be expanded into a more consistent version of it, the mutliloop functional renormalization group (mfRG), following Refs. [1] and [19]. We then continue to explain how these two methods can be merged together into a coherent Keldysh mfRG framework, that we use to study the SIAM.

After the theoretical tools have been presented, we dedicate a major part of this work to the study of the internal structure of the vertex function. We present a thorough analysis of the internal symmetries this object possesses, as well as the interplay these have on the different decompositions that can be readily done with the vertex. These include a decomposition into interaction channels [1, 2, 5, 7, 20] as well as an asymptotic treatment of the real frequency dependence, based mainly on Ref. [5].

To actually test the capabilities of the mfRG, we implement a C++ code to carry out the numerical computations. We give details and caveats on the implementation of our code in Chapter 4. We also present a summarized "recipe" for it in Appendix B. We also present consistency checks that can be implemented either as unit or inclusion tests during the implementation or safety checks to be checked at runtime.

We finalize this work with the presentation and subsequent analysis of the results our code is currently able to produce. We pay special attention to the fulfillment of parquet equations and adherence to conditions imposed by fundamental physical constraints like causality and the fluctuation-dissipation theorem, and agreement of our results with the theory. We present results for equilibrium and non-equilibrium calculations.

Chapter 2

Theoretical background

In the present Chapter, we present the two main theoretical tools for the present work, the multiloop functional renormalization group and the Keldysh formalism, and then a way in which one can combine them for the computational study of non-equilibrium systems. We first give a brief introduction to the physical system studied in this thesis, the single-impurity Anderson model, which has the advantage of being made up of simple components, yet it shows rich physics. It has been thoroughly studied and is well understood and is therefore a perfect tool for benchmarking the development of a new, potentially very successful and widely-applicable method.

2.1 The single-impurity Anderson model

The study of the transport properties of physical systems has been of interest for quite a long time. Of late, particular attention has gone into mesoscopic systems, which show notoriously diverse physics for the relatively simple components they are made of. A typical set-up for these systems consist of a confined region of nano-scale which is generally coupled to several macroscopic conducting leads as in quantum dots, quantum wires or quantum point contacts. Due to the smallness of the confined region, a quantum-mechanical description of the system is needed. Furthermore, the transport characteristics of these kinds of systems are heavily affected by interactions, be it of Coulomb type between electrons, electron-phonon scattering or spin-orbit coupling. We focus on the first one, specializing it directly to the case of two metallic reservoirs and a single-electron level, called dot, in the confined region. This is the single-impurity Anderson model [15].

The Hailtonian describing this system is [6]

$$H = H_{\text{dot}}^{(0)} + V_{\text{dot}} + \sum_{r=\text{L,R}} H_{\text{res}}^{(r)} + \sum_{r=\text{L,R}} H_{\text{coup}}^{(r)} \tag{2.1}$$

with

$$\begin{aligned} H_{\text{dot}}^{(0)} &= \sum_{\sigma} \left(eV_{\text{g}} - \sigma B - \frac{U}{2} \right) d_{\sigma}^{\dagger} d_{\sigma} \\ V_{\text{dot}} &= U d_{\uparrow}^{\dagger} d_{\uparrow} d_{\downarrow}^{\dagger} d_{\downarrow} \\ H_{\text{res}}^{(r)} &= \sum_{\sigma} \int \mathrm{d}k_r \epsilon_{k_r} a_{k_r\sigma}^{\dagger} a_{k_r\sigma} \\ H_{\text{coup}}^{(r)} &= \sum_{\sigma} \int \mathrm{d}k_r \left(t_{k_r} d_{\sigma}^{\dagger} a_{k_r\sigma} + \text{h.c.} \right) \end{aligned} \tag{2.2}$$

In these equations $\sigma = \pm\frac{1}{2}$ denotes the spin of the single-particle states of the impurity, $d_{\sigma}^{(\dagger)}$ annihilate (create) a particle in the impurity site, $a_{k_r,\sigma}^{(\dagger)}$ create (annihilate) states in the reservoirs, labeled by $r = L,\ R$ for "left" and "right". The on-site energy is denoted by U.

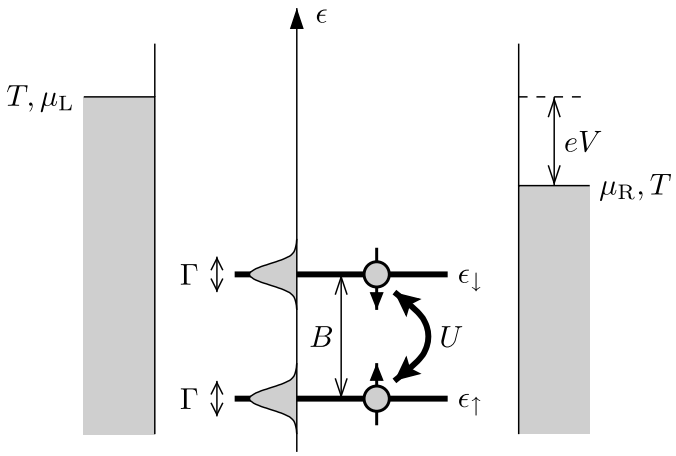

Figure 2.1: Sketch of the model with single-particle energy in the vertical direction. Taken from [6].

The single-particle energies of the dot,

$$\epsilon_{\sigma} = eV_{\text{g}} - \sigma B - U/2 \tag{2.3}$$

which depend on the bias voltage V_g between the two leads and the magnetic field B through the dot, have been shifted by $-(U/2)$ so that the particle-hole symmetric case is reached when $eV_g = \mu$, with μ being the chemical potential. In this thesis we are only interested in conductive transport and thus assume that the temperature of both reservoirs is the same $T_R = T_L = T$. We also set $B = 0$ throughout. Since we only study the transport properties through the dot, we also gross over the band structure and the interaction details of the reservoirs and make use of the wide band limit. We further take both lead-couplings $t_{k_r}^{(r)}$ to be independent of k_r. Thus, the hybridizations,

$$\Gamma_{(r)} = 2\pi \frac{|t^{(r)}|^2}{v_r},\ r = L,\ R\,, \tag{2.4}$$

do not depend on spin. We also assume symmetric coupling $\Gamma_L = \Gamma_R$, which simplifies calculations. Finally, the total hybridization is defined as

$$\Gamma = \Gamma_L + \Gamma_R \tag{2.5}$$

in accordance with [6].

This concludes the brief introduction of the model we will be looking at. Now, we present the first of our main theoretical tools to tackle it: the multiloop functional renormalization group.

2.2 The multiloop functional renormalization group

The analytic description of interacting systems has been a long sought-after goal in theoretical physics. Not only restricted to the field of condensed matter physics but also including the areas of high-energy physics, statistical physics and even cosmology, renormalization is currently the best tool we have for trying to better understand these kinds of systems. More than a theory, the renormalization group has become a meta-theory, a set of concepts and methods that can be used to understand phenomena through all of physics. In the context of solid state theory, the functional renormalization group (fRG) is a very popular tool, which builds up on Wilson's idea and mathematically formalizes its implementation. However, the applicability of this scheme is not restricted to only this area. The present section of this work is dedicated to presenting the basics of the fRG, discussing some of its shortcomings and giving a quick introduction to the newly developed multiloop version of it [1, 2, 19]. We assume the reader has a good understanding of field theoretical as well as of functional methods.

2.2.1 The functional renormalization group

As noted above, the functional renormalization group is based upon the Wilsonian idea of renormalization, which is, in essence, a controlled, step-wise elimination of the faster modes of a system. The way in which this is rigorously achieved is through the inclusion of a functional dependency on an arbitrary energy scale Λ, so that the interacting theory is effectively free at $\Lambda \to \infty$ and the full theory is recovered at $\Lambda \to 0$. Then one uses the functional representation of generating functionals to obtain exact differential equations in Λ, which then one can hope to solve. The initial condition at $\Lambda \to \infty$ is the analytically known set of bare quantities describing the system. Then, the flow according to the ODEs in Λ yields the full characterization of the interacting system.

The functional dependency on Λ is achieved through the inclusion of a regulator in the bare propagator, G_0, of the free theory,

$$G_0 \to G_0^\Lambda \,. \tag{2.6}$$

The regulator must be included so that G_0^Λ vanishes as $\Lambda \to \infty$ and is fully restored as $\Lambda \to 0$. The idea is that modes of scale smaller than Λ are frozen, not yet integrated

out. The choice of regulator in Eq. (2.6) is completely arbitrary, as long as the boundary conditions

$$G_0^\Lambda \sim \begin{cases} G_0 \text{ for } \Lambda \to 0\,, \\ 0 \text{ for } \Lambda \to \infty\,, \end{cases} \tag{2.7}$$

are fulfilled. The easiest way to implement this would be with a multiplicative step-function $\theta(|\omega| - \Lambda)$, but this is not the only possibility. Due to analytic considerations it may sometimes be better to opt for a different regulator with nicer analytical properties and which does not generate discontinuities. The best approach depends strongly on the physical system at hand.

Once G_0 is replaced by G_0^Λ, every object in the theory automatically inherits a Λ-dependency. To see this, let us study a general interacting system, whose action $S[\bar{\psi}, \psi] = S_0[\bar{\psi}, \psi] + S_1[\bar{\psi}, \psi]$ is composed of a free (S_0) and an interacting part (S_1). With the inclusion of the regulator, the action becomes

$$S_0 \to S_0^\Lambda = -\frac{1}{2} \int_\alpha \int_{\alpha'} \psi_\alpha \left[\left(G_0^\Lambda \right)^{-1} \right]_{\alpha\alpha'} \psi_\alpha \,, \tag{2.8}$$

where we use the super-index and super-field notation introduced in [11]. Thus α is a multi-index, encoding type of field, energy, momentum, spin and whatever other label or quantum number is necessary and $\int_\alpha$ stands for an integration over the continuous variables and a sum over the discrete indices.

Equation (2.6) has no effect on S_1, since G_0 never appears in those terms of the action. Hence, for any expectation value calculation of the form

$$\langle \hat{\mathcal{O}} \rangle_0 = \frac{\int \mathcal{D}[\bar{\psi}, \psi] e^{-S_0[\bar{\psi}, \psi]} \hat{\mathcal{O}}}{\int \mathcal{D}[\bar{\psi}, \psi] e^{-S_0[\bar{\psi}, \psi]}} \to \langle \hat{\mathcal{O}}^\Lambda \rangle_0 = \frac{\int \mathcal{D}[\bar{\psi}, \psi] e^{-S_0^\Lambda[\bar{\psi}, \psi]} \hat{\mathcal{O}}}{\int \mathcal{D}[\bar{\psi}, \psi] e^{-S_0^\Lambda[\bar{\psi}, \psi]}} \,, \tag{2.9}$$

i.e. the expectation values of operators become Λ-dependent, and this dependency comes exclusively from the inclusion of the regulator. Now, the kinds of objects we are interested in are one- and two-particle irreducible n-particle vertices (1PI and 2PI, respectively), which can be obtained through functional derivatives of the action. These objects then inherit this Λ-dependency only through the inclusion of the regulator. This implies that the vertices, to all orders, become Λ dependent. The derivation of these equations is textbook material, see Chapter 7 of reference [11].

The most important result of this derivation for our purposes is the flow equations of the n-particle vertices $\Gamma^{(n)}$, whose exact form is however irrelevant for us. What interests us is that these are an infinite hierarchy of coupled integro-differential equations, which

can be schematically represented as

$$\dot{\Gamma}^{(2)} = f_2\left(\Gamma^{(4)}\right) \tag{2.10a}$$
$$\dot{\Gamma}^{(4)} = f_4\left(\Gamma^{(4)}, \Gamma^{(6)}\right) \tag{2.10b}$$
$$\dot{\Gamma}^{(6)} = f_6\left(\Gamma^{(4)}, \Gamma^{(6)}, \Gamma^{(8)}\right) \tag{2.10c}$$
$$\vdots$$
$$\dot{\Gamma}^{(n)} = f_n\left(\Gamma^{(4)}, \ldots, \Gamma^{(n)}, \Gamma^{(n+2)}\right) \tag{2.10d}$$

Here, $\Gamma^{(n)} := \partial_\Lambda[\Gamma^{(n)}]^\Lambda$. Eq. (2.10) is particular for a fermionic system with a two-body interaction with fermionic statistics exclusively. These kinds of models automatically have zero interaction vertices for an odd number of particles, since these kinds of interactions would violate conservation rules. The hierarchy presented in Eq. (2.10) constitutes an intractably complicated set of equations for the f_i's. Furthermore the exact form the f_i's take depends on what regulator is chosen.

Flow equations for a two-fermion interaction

For fermions with spin, the interaction part of the action is SU(2)-spin invariant. Thus, it must take the form [11]

$$\begin{aligned} S_1[\bar{\psi}, \psi] =& \frac{1}{(2!)^2} \int_{K'\sigma_1'} \int_{K_2'\sigma_2'} \int_{K_1\sigma_1} \int_{K_2\sigma_2} \delta_{K_1'+K_2', K_1+K_2} \\ & \times \Gamma^{(4)}\left(K_1'\sigma_1', K_2'\sigma_2'; K_1\sigma_1, K_2\sigma_2\right) \bar{\psi}_{K_1'\sigma_1'} \bar{\psi}_{K_2'\sigma_2'} \psi_{K_1\sigma_1} \psi_{K_2\sigma_2} \,, \end{aligned} \tag{2.11}$$

where $(K\sigma)$ has replaced α as a multi-index, now particularly standing for energy, momentum and spin to be able to write momentum conservation explicitly, and $\Gamma_0^{(4)}$ is antisymmetric with respect to the exchange of its first two and its second two labels.

The flow equations for the vertices are presented next. The first one we consider is the two-point vertex $\Gamma^{(2)}(K\sigma, K\sigma) \equiv \Sigma(K\sigma)$. Starting from now, we will refer to the two-point vertex as the *self-energy*. Its RG-flow equation is

$$\partial_\Lambda \Sigma^\Lambda(K\sigma) = -\int_{K'\sigma'} S^\Lambda\left(K'\sigma'\right) \left[\Gamma^{(4)}\right]^\Lambda \left(K\sigma, K'\sigma; K'\sigma', K\sigma\right) \tag{2.12}$$

where $S^\Lambda = \partial_\Lambda G^\Lambda\big|_{\Sigma^\Lambda=\text{const}}$ is the single-scale propagator.

The respective equation for the four-point vertex $\Gamma^{(6)}$ is

$$\begin{aligned}
\partial_\Lambda \left[\Gamma^{(4)}\right]^\Lambda (K_1'\sigma_1', K_2'\sigma_2'; K_1\sigma_1, K_2\sigma_2) &= \int_K \sum_\sigma \dot{G}^\Lambda(K\sigma) \left[\Gamma^{(6)}\right]^\Lambda (K_1'\sigma_1', K_2'\sigma_2', K\sigma; K\sigma, K_1\sigma_1, K_2\sigma_2) \\
&+ \int_K \sum_{\sigma\sigma'} \dot{G}^\Lambda(K\sigma) G^\Lambda\left(K_2 + K_1 - K\sigma'\right) \\
&\quad \times \left[\Gamma^{(4)}\right]^\Lambda (K_1'\sigma_1', K_2'\sigma_2'; K_2 + K_1 - K\sigma', K\sigma) \left[\Gamma^{(4)}\right]^\Lambda (K\sigma, K_2 + K_1 - K\sigma'; K_1\sigma_1, K_2\sigma_2) \\
&- \int_K \sum_{\sigma\sigma'} \left[\dot{G}^\Lambda(K\sigma) G^\Lambda\left(K + K_2 - K_1'\sigma'\right) + G'(K\sigma)\dot{G}'\left(K + K_2 - K_1'\sigma'\right)\right] \\
&\quad \times \left[\Gamma^{(4)}\right]^\Lambda (K_1'\sigma_1', K + K_2 - K_1'\sigma'; K\sigma, K_2\sigma_2) \left[\Gamma^{(4)}\right]^\Lambda (K_2'\sigma_2', K\sigma; K + K_2 - K_1'\sigma', K_1\sigma_1) \\
&+ \int_K \sum_{\sigma\sigma'} \left[\dot{G}^\Lambda(K\sigma) G^\Lambda\left(K + K_1 - K_1'\sigma'\right) + G'(K\sigma)\dot{G}'\left(K + K_1 - K_1'\sigma'\right)\right] \\
&\quad \times \left[\Gamma^{(4)}\right]^\Lambda (K_1'\sigma_1', K + K_1 - K_1'\sigma'; K\sigma, K_1\sigma_1) \left[\Gamma^{(4)}\right]^\Lambda (K_2'\sigma_2', K\sigma, K + K_1 - K_1'\sigma', K_2\sigma_2)
\end{aligned} \tag{2.13}$$

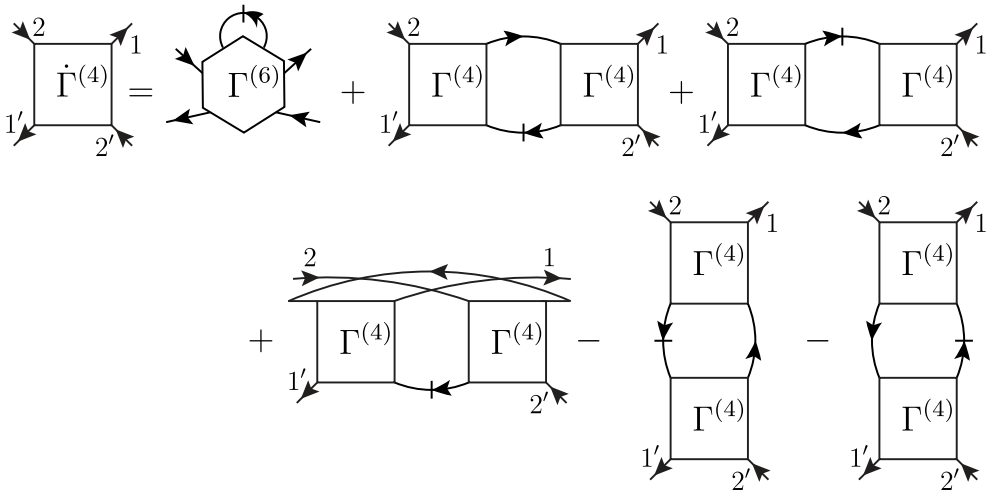

Figure 2.2: Graphical representation of Eq. (2.13). In Eq. (2.13) we already assume a fully fermionic theory, thus setting $\zeta = -1$.

In Eq. (2.13) $\dot{G}^\Lambda = \partial_\Lambda G^\Lambda = S^\Lambda + G^\Lambda \cdot \dot{\Sigma}^\Lambda \cdot G^\Lambda$, where the second term is commonly named the Katanin extension [1, 21]. This equation is much more complicated than Eq. (2.12). This trend would continue with increasing n, with more and more combinations of lower order vertices contributing to the overall result.

The $\Gamma^{(6)}$ term in Eq. (2.13) can be neglected as long as $\Lambda \gtrsim \Lambda_6$, where Λ_6 is the scale at which the contributions of the $\Gamma^{(6)}$ vertex become important. A common approximation to solve Eq. (2.13) is then to set $\Gamma^{(6)} = 0$, which implies that $\Lambda_6 = 0$. This translates to saying that at no scale is $\Gamma^{(6)}$ ever important. Since $\Lambda_6 > \Lambda_n$ for all $n \geq 6$, this assumption

implies that all higher order vertices are also set to zero, which effectively truncates the infinite hierarchy and yields a two-equation system for the self-energy and the four-point vertex. In this case one must only solve these two coupled equations, which is still a task easier said than done.

Now we take a closer look at Eqs. (2.12) and (2.13). First, notice that the propagator that appears in both equations is G^Λ and not G_0^Λ. This means that, indirectly, the derivatives of both quantities depend on both the self-energy and the four-point vertex itself, i.e. both equations depend on both quantities. Also, by just looking at the momenta combinations of Eq. (2.13) and the way these can be represented graphically (see Fig. 2.2), it is clear that the vertex can be decomposed and studied in *interaction channels*, based on the reducibility of the diagrams and the natural frequency-momenta combinations that appear. These aspects will be discussed in more depth later on, since these also affect the way in which the vertex is computed numerically. Hence, we continue with a discussion of the shortcomings of the fRG, particularly in the case of the truncated hierarchy we present here.

Shortcomings of the fRG

In the derivation of Eqs. (2.12) and (2.13) two major assumptions come into play. The first one is that the interactions are fairly weak. The use of Eq. (2.9) in a numerical calculation implies the utilization of a series in the coupling constant or, effectively, on the interaction strength U. As usual with a diagrammatic method resulting in a series expansion in the interaction strength, the convergence of said series depends on the weakness of the characteristic interaction strength U compared to the other energy scales of the system. This is a subtle point to keep in mind, because it implies that no matter how much effort one puts into a *numeric* fRG-calculation, the method will remain perturbative, even if the fRG is not, in itself, perturbative. Notably, fRG is much better than regular perturbation theory, since in the flow it implicitly generates and adds diagrams to infinite order in U.

The second aspect to take into account is the assumption $\Gamma^{(6)} \to 0$. Though the assumption may seem very reasonable for weak interactions, one must be careful with the ramifications it has. Therefore, we recall the infinite hierarchy presented schematically in Eq. (2.10). Here, all f_i are exact derivatives, meaning that, together with a set of initial conditions for the values of the n-particle vertices at $\Lambda \to \infty$, a simultaneous integration yields the exact solution. The truncation of the hierarchy that arises by setting $\Gamma^{(6)} = 0$ throughout the flow breaks the full-derivative structure of f_4. This means that the flow of the vertex with the truncated $\tilde{f}_4 \neq f_4$ deviates from the exact solution [22]. This leads to the breaking down of fundamental, one-particle conservation laws and the violation of Ward identities. Noticeably, although f_4 is affected by this assumption directly, the functional form of f_2 remains unaltered. Thus, since the flow according to $\tilde{f}_4$ yields a truncated version of the four-point vertex, f_2 must be corrected to compensate for the non-exact objects used as arguments. Notice that f_4 depends explicitly only on $\Gamma^{(4)}$ and $\Gamma^{(6)}$. Hence, a silver lining appears: if somehow the contributions of $\Gamma^{(6)}$ could be mimicked,

the truncated system of equations (i.e. only f_2 and f_4) could more closely resemble the exact problem.

Another point in which the fRG fails is in regulator independence. As noted above, there is complete freedom in choosing the regulator, as long as it fulfills the required boundary conditions at $\Lambda \to \infty$ and $\Lambda \to 0$ and cuts off the right modes in its flow towards 0. Since the form the f_i's take in Eq. (2.10) depend on the choice of regulator, the resulting flow is different for every choice. However, since there need not be physical information in the regulator (it is a mathematical aid to formally integrate out modes in a controlled manner), the predictions delivered by the flow should not depend on its choice. The fact that in this scheme they do is a major limitation of the fRG.

Because of these shortcomings of the functional renormalization group is that the multiloop functional renormalization group (mfRG) was developed. It deals with and improves on the problems mentioned here. To begin our discussion of the mfRG, we first turn our attention to the parquet formalism, since the mfRG is based on it.

2.2.2 The parquet formalism

A fundamental part of the multiloop fRG (mfRG) is that it is formulated on the parquet formalism, which is a series of equations to break up the four-point vertex and exploit the natural decomposition that is depicted in Fig. 2.2. Here we follow the conventions of [1]:

- Labels regarding quantum numbers, momentum or energy dependencies are summarized in multi-indices, noted as sub-indices.

- The super-index Λ indicates a scale-dependent quantity. The index may be omitted when there is no risk of confusion.

- A derivative with respect to Λ is denoted by a dot: $\dot{X}^\Lambda := \partial_\Lambda X^\Lambda$.

- The two-point vertex is denoted by Σ^Λ and is referred to as the self-energy.

- The four-point vertex is denoted by Γ^Λ and is referred to as the vertex.

- The bare four-point vertex is denoted by Γ_0, is antisymmetric in its first and last two arguments, and has trivial momentum and frequency dependence.

- The strength of the interaction is given by U.

- Propagators G and bubbles Π (introduced and defined below) carry primed indices in the incoming legs and unprimed in the outgoing ones.
- Vertices (e.g. Γ and Σ) carry unprimed indices in the incoming legs and primed indices in the outgoing ones.

As noted in [1], the parquet formalism yields a decomposition of the vertex into *antiparallel* (a), *parallel* (p) and *transverse* (t) reducible diagrams. This turns out to be exclusive, with no diagram possibly being in two different categories, yet not exhaustive, with there also existing completely irreducible contributions. The term reducibility here makes reference to the specific case of two-particle reducibility of a diagram: a 2-PR diagram is one that becomes disconnected after snipping two propagator lines. The names of the decomposition channels come from the way the propagator lines that need to be cut to render the diagram disconnected lie with respect to one another, as illustrated in Fig. 2.4. Thus, the equation for the full vertex Γ can be written as

$$\Gamma = R + \sum_{r\in\{a,p,t\}} \gamma_r \,, \tag{2.14}$$

where R stands for the completely irreducible part of the vertex (see Fig. 2.3) and γ_r for the 2-PR part of the vertex in channel r. Some other common nomenclatures for the channels a, p and t include, respectively, x, p, d, standing for *exchange*, *pairing* and *direct*, common in high energy physics contexts, and ph, pp and $\bar{ph}$ for (longitudinal) particle-hole, particle-particle, and transverse particle-hole, mostly used within the condensed matter community. The physical reason behind this decomposition is the fact that each one of these processes describes a different kind of scattering process (more notorious in the ph, pp, $\bar{ph}$ nomenclature). This channel analysis yields a way for analyzing leading scattering processes in a model, as one channel may present a singularity where the other ones do not, signaling an instability driven solely by interactions through the corresponding channel.

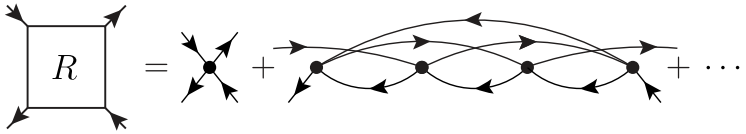

Figure 2.3: Diagrammatic representation of the irreducible vertex. Notice that $R - \Gamma_0 = \mathcal{O}(U^4)$.

Now, since a diagram can only be reducible in one channel, all diagrams irreducible in a particular channel r can be bunched together into an irreducible vertex I_r in that particular channel:

$$I_r = R + \sum_{r'\neq r} \gamma_{r'} \,. \tag{2.15}$$

This definition allows for an important way to calculate γ_r, namely

$$\gamma_r = I_r \circ \Pi \circ \Gamma \tag{2.16}$$

or, written out explicitly,

$$[\gamma_a]_{x_{1'},x_{2'}|x_1,x_2} = \sum_{y_{1'},y_1,y_{2'},y_2} [I_a]_{x_{1'},y_{2'}|y_1,x_2} \underbrace{\left(G_{y_1|y_{1'}} G_{y_2|y_{2'}}\right)}_{[\Pi_a]_{y_1 y_2|y_{1'} y_{2'}}} \Gamma_{y_{1'},x_{2'}|x_1,y_2} \tag{2.17a}$$

$$[\gamma_p]_{x_{1'},x_{2'},|x_1,x_2} = \sum_{y_{1'},y_1,y_{2'},y_2} [I_p]_{x_1,x_2|y_1,y_2} \underbrace{\left(\frac{1}{2} G_{y_1|y_{1'}} G_{y_2|y_{2'}}\right)}_{[\Pi_p]_{y_1 y_2|y_{1'} y_{2'}}} \Gamma_{y_{1'},y_{2'}|x_1,x_2} \quad \text{and} \tag{2.17b}$$

$$[\gamma_t]_{x_{1'},x_{2'}|x_1,x_2} = \sum_{y_{1'},y_1,y_{2'},y_2} [I_t]_{y_{1'},x_{2'}|y_1,x_2} \underbrace{\left(-G_{y_2|y_{1'}} G_{y_1|y_{2'}}\right)}_{[\Pi_t]_{y_1 y_2|y_{1'} y_{2'}}} \Gamma_{x_{1'},y_{2'}|x_1,y_2} \tag{2.17c}$$

These are known as the Bethe–Salpeter equations. These relate the irreducible vertices to the reducible ones in a self-consistent way. Eq. (2.17) sees also the definition of a propagator-like object, which we call a bubble (Π_r in channel r). More than being a pair of propagators, it is the way these connect to the vertices which make them useful.

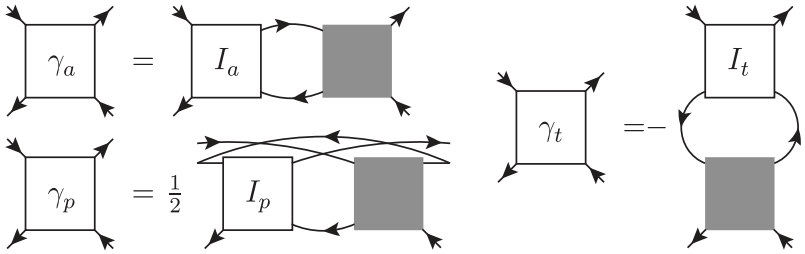

Figure 2.4: Bethe–Salpeter equations in the three two-particle channels. Taken directly from [1].

Abstracting the structure of Eqs. (2.16) and (2.17) allows us to define the bubble functions B_r as follows [1]

$$B_r(\Gamma, \Gamma') = \Gamma \circ \Pi_r \circ \Gamma' = \Gamma \circ (G \circ G) \circ \Gamma' \tag{2.18}$$

and, written out explicitly for every channel,

$$B_a(\Gamma, \Gamma')_{x_{1'},x_{2'}|x_1,x_2} = \sum_{y_{1'},y_1,y_{2'},y_2} \Gamma_{x_{1'},y_{2'}|y_1,x_2} \underbrace{\left(G_{y_1|y_{1'}} G_{y_2|y_{2'}}\right)}_{[\Pi_a]_{y_1 y_2|y_{1'} y_{2'}}} \Gamma'_{y_{1'},x_{2'}|x_1,y_2}\,, \tag{2.19a}$$

$$B_p(\Gamma, \Gamma')_{x_{1'},x_{2'}|x_1,x_2} = \sum_{y_{1'},y_1,y_{2'},y_2} \Gamma_{x_{1'},x_{2'}|y_1,y_2} \underbrace{\left(\frac{1}{2} G_{y_1|y_{1'}} G_{y_2|y_{2'}}\right)}_{[\Pi_p]_{y_1 y_2|y_{1'} y_{2'}}} \Gamma'_{y_{1'},y_{2'}|x_1,x_2} \text{ and} \tag{2.19b}$$

$$B_t(\Gamma, \Gamma')_{x_{1'},x_{2'}|x_1,x_2} = \sum_{y_{1'},y_1,y_{2'},y_2} \Gamma_{y_{1'},x_{2'}|y_1,x_2} \underbrace{\left(-G_{y_2|y_{1'}} G_{y_1|y_{2'}}\right)}_{[\Pi_t]_{y_1 y_2|y_{1'} y_{2'}}} \Gamma'_{x_{1'},y_{2'}|x_1,y_2}\,. \tag{2.19c}$$

Notice the difference between the indices of Π_t with respect to those of Π_a and Π_p. Thus, Eq. (2.16) can be written as

$$\gamma_r = B_r\left(I_r, \Gamma\right) . \tag{2.20}$$

A fact we will not prove here is that $\gamma_r = B_r\left(I_r, \Gamma\right) = B_r\left(\Gamma, I_r\right)$.

The calculation of the Bethe–Salpeter equations requires dressed propagators. Thus, the self-energy must also be determined, which can be self-consistently done according to the Schwinger–Dyson equation

$$\begin{aligned} \Sigma &= L\left(\Gamma_0, G\right) + L\left[B_p\left(\Gamma_0, \Gamma\right), G\right] \\ &= L\left(\Gamma_0, G\right) + \frac{1}{2} L\left[B_a\left(\Gamma_0, \Gamma\right), G\right] , \end{aligned} \tag{2.21}$$

where we have made use of the loop function

$$L(\Gamma, G)_{x',x} = -\sum_{y',y} \Gamma_{x',y'|x,y} G_{y|y'} \tag{2.22}$$

and both formulations in Eq. (2.21) are completely equivalent.

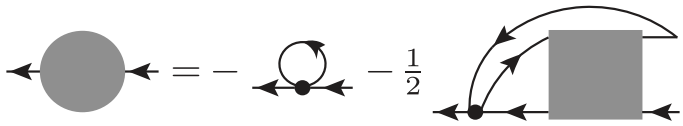

Figure 2.5: Schwinger–Dyson equation for the self-energy. Notice how one can think equivalently of the lines joinig the bare and the full vertices on the right as loop over an a or a p bubble.

This completes the set of, in total, 10 objects that the parquet formalism works with: the full vertex Γ, the completely irreducible part of it R, the three irreducible parts I_r, the three reducible parts γ_r, the self-energy Σ and the propagator G. As such, this system of equations only requires the input of the totally irreducible part of the vertex. Hence, we here introduce the first approximation we need within the parquet formalism.

The parquet approximation The parquet approximation (PA) corresponds to setting the irreducible part $R = \Gamma_0$, incurring in an error $\mathcal{O}(U^4)$. This approach is hence intrinsically perturbative and can be expected to break down for large values of the interaction strength.

Including multi-indices, Eq. (2.14) becomes

$$\Gamma_{x_{1'},x_{2'}|x_1,x_2} = [\Gamma_0]_{x_{1'},x_{2'}|x_1,x_2} + [\gamma_a]_{x_{1'},x_{2'}|x_1,x_2} + [\gamma_p]_{x_{1'},x_{2'}|x_1,x_2} + [\gamma_t]_{x_{1'},x_{2'}|x_1,x_2} \tag{2.23}$$

where we include a set of multi-indices for the bare vertex since it may have spin and other kinds of structure. This approximation allows us to, effectively, need no physical input other than the bare vertex to solve the equations of the parquet formalism. The irreducible part of the vertex cannot be determined within the parquet formalism alone.

The flow equations of the mfRG

We now return to the main idea of the fRG, namely the derivation of differential equations for the self-energy and the vertex in the infrared cutoff Λ, and combine it with the equations of the parquet formalism under the PA. Having analytic expressions for both the vertex and the self-energy, we begin by differentiating the former and including a diagrammatic classification in the number of loops present in a diagram (loops here is to be understood in the sense of nested integrals and not simply in the presence of two propagator lines joining two vertices).

$$\partial_\Lambda \Gamma = \sum_r \partial_\Lambda \gamma_r, \quad \partial_\Lambda \gamma_r = \sum_{\ell \geq 1} \dot{\gamma}_r^{(\ell)}, \quad \dot{\gamma}_{\bar{r}}^{(\ell)} = \sum_{r' \neq r} \dot{\gamma}_{r'}^{(\ell)} \tag{2.24}$$

Here, $\dot{\gamma}_r^{(\ell)}$ contains differentiated diagrams reducible in channel r, with ℓ nested loops. Notice that the nested loops can be constructed iteratively by the inclusion of lower loop-order diagrams into ones of higher order, in a channel-mixing fashion.

The multiloop recursive relations are [1]

$$\dot{\gamma}_r^{(1)} = \dot{B}_r(\Gamma, \Gamma)\,, \tag{2.25a}$$

$$\dot{\gamma}_r^{(2)} = B_r\left(\dot{\gamma}_{\bar{r}}^{(1)}, \Gamma\right) + B_r\left(\Gamma, \dot{\gamma}_{\bar{r}}^{(1)}\right)\,, \tag{2.25b}$$

$$\dot{\gamma}_r^{(\ell+2)} = B_r\left(\dot{\gamma}_{\bar{r}}^{(\ell+1)}, \Gamma\right) + \dot{\gamma}_{r,\mathrm{C}}^{(\ell+2)} + B_r\left(\Gamma, \dot{\gamma}_{\bar{r}}^{(\ell+1)}\right)\,, \tag{2.25c}$$

$$\dot{\gamma}_{r,\mathrm{C}}^{(\ell+2)} = B_r\left[\Gamma, B_r\left(\dot{\gamma}_{\bar{r}}^{(\ell)}, \Gamma\right)\right] = B_r\left[B_r\left(\Gamma, \dot{\gamma}_{\bar{r}}^{(\ell)}\right), \Gamma\right]\,. \tag{2.25d}$$

Here, $\dot{B}_r\left(\Gamma, \Gamma'\right) = \partial_\Lambda B_r\left(\Gamma, \Gamma'\right) \equiv \left[\Gamma \circ \partial_\Lambda (G \circ G) \circ \Gamma'\right]$ corresponds to the derivative of the bubble function, defined in Eq. (2.19), taking the vertices as Λ-independent. To fully characterize them, we need to study the derivatives of G^Λ with respect to Λ. The single-scale propagator fulfills

$$S^\Lambda \equiv \partial_\Lambda G^\Lambda_{|\Sigma=\mathrm{const}} = \left(1 + G^\Lambda \cdot \Sigma^\Lambda\right) \cdot \left(\partial_\Lambda G_0^\Lambda\right) \cdot \left(\Sigma^\Lambda \cdot G^\Lambda + 1\right)\,. \tag{2.26}$$

Thus,

$$\partial_\Lambda G^\Lambda = S^\Lambda + G^\Lambda \cdot \left(\partial_\Lambda \Sigma^\Lambda\right) \cdot G^\Lambda \tag{2.27}$$

includes the corrections originating from vertex diagrams containing differentiated self-energy contributions [21]. $\dot{G}$ can be inserted into Eq. (2.25a) to get a flow which includes these corrections. Another possibility is calculating Eq. (2.25a) with $\partial_\Lambda\left(G^\Lambda G^\Lambda\right) \approx S^\Lambda G^\Lambda + G^\Lambda S^\Lambda$, which is computationally cheaper.

We point out that the conventional fRG scheme in the parquet formalism corresponds to the truncation of the recursive relations presented above at first order, i.e. Eqs. (2.25b) through (2.25d) are simply not present. This absence prevents contributions of different channels from mixing and, thus, yields results which show a bias towards ladder diagrams. The mfRG improves on this by the recursive inclusion of nested loop integrals from different channels, thus yielding a complete computation of the diagrams, which in one-loop fRG

are computed only partially. This removes the bias which fRG has towards certain kinds of processes. The multiloop terms effectively simulate contributions of the higher-order vertex $\Gamma^{(6)}$, which help improve on restoring the full derivative structure of the right hand side of the flow equation of the vertex. Thus, the mfRG solves the issue conventional, one-loop fRG has with one-particle conservation laws and also solves the issue of regulator dependence.

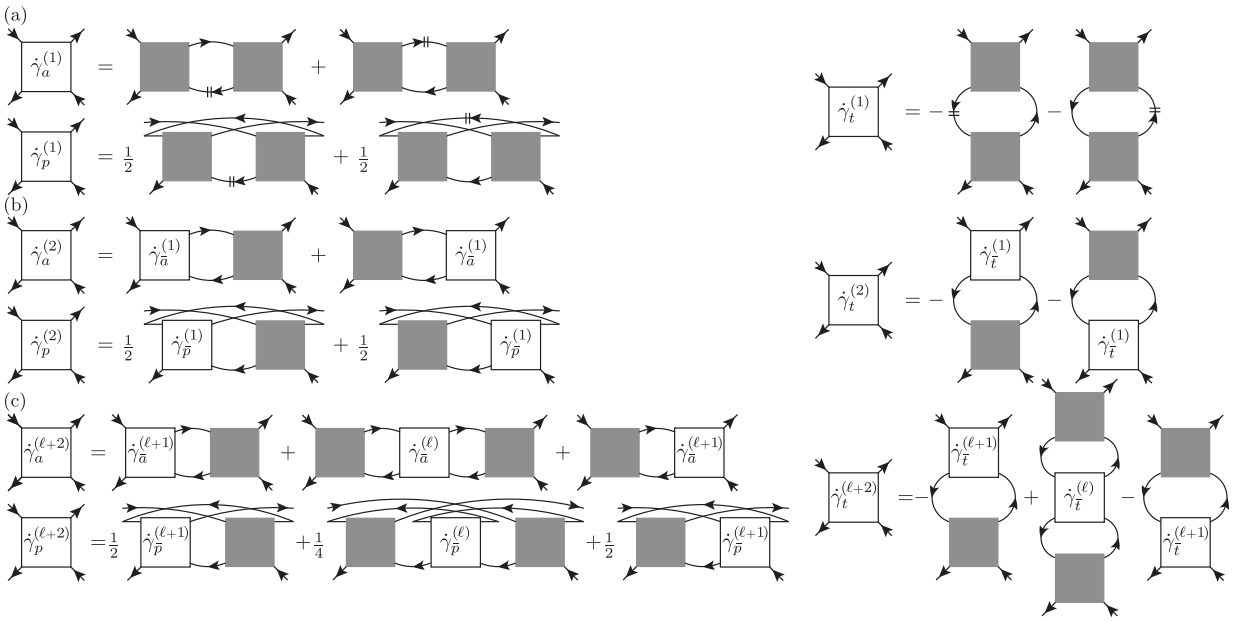

Figure 2.6: Multiloop flow equations for the vertex. (a) The standard, truncated, one-loop flow, where double dashed lines stand for $\partial_\Lambda G^\Lambda$. (b) The two-loop extension of (a). Notice the channel mixing already occurring at this stage. Thus, 2-loop fRG already includes diagrams that are partially computed in a standard fRG-flow. (c) Higher-loop corrections starting from $\ell + 2 = 3$, which include the extra contributions (the central part) where vertices from the complementary channels are connected by two bubbles. Taken directly from [1].

The fact that the flow of Γ is improved also means that the flow of the self-energy is improved, though there are also some caveats to pay attention to. The flow equation for the self-energy, Eq. (2.12), rewritten making use of the functions defined above, is

$$\dot{\Sigma}^\Lambda = \dot{L}(\Gamma, G) = L(\Gamma, S)\,, \tag{2.28}$$

i.e. making a closed loop over a vertex with a single-scale propagator.

If the vertex inserted into Eq. (2.28) was the exact, full vertex, with no truncations, the relation would be exact. However, if a vertex $\tilde{\Gamma}$ obtained from a truncated vertex flow is inserted into Eq. (2.28), it generates diagrams that are only partially differentiated and $L(\tilde{\Gamma}, S)$ does not yet form a full derivative. Thus, some multiloop corrections must be added to the self-energy flow to complete the derivative. These come from each one of the

channels, where the t channel must be handled in a slightly different way due to the way the propagator lines connect in the self-energy calculation. We therefore define first

$$\dot{\gamma}_{t,C} = \sum_{l\geq 1} \left(\dot{\gamma}^{(l)}_{a,C} + \dot{\gamma}^{(l)}_{p,C} \right) \tag{2.29}$$

and divide the flow equation of Σ^Λ in three parts, namely the standard flow (Eq. (2.28), now labeled Σ_{std}), the $\bar{t}$ corrections $\dot{\Sigma}_{\bar{t}}$ and the corrections in the t channel, $\dot{\Sigma}_t$. The last two are defined as follows

$$\dot{\Sigma}_{\bar{t}} = L\left(\dot{\gamma}_{\bar{t},C}, G\right) \tag{2.30}$$

$$\dot{\Sigma}_t = L\left(\Gamma, G \cdot \dot{\Sigma}_{\bar{t}} \cdot G\right) \tag{2.31}$$

and, thus,

$$\begin{aligned} \Sigma^\Lambda &= \dot{\Sigma}^\Lambda_{\text{std}} + \dot{\Sigma}_{\bar{t}} + \dot{\Sigma}_t \\ &= L(\Gamma, S) + L\left(\dot{\gamma}_{\bar{t},C}, G\right) + L\left(\Gamma, G \cdot \dot{\Sigma}_{\bar{t}} \cdot G\right) \end{aligned} \tag{2.32}$$

Notice that these corrections, as they include central loop terms, appear only in loop-order $\ell \geq 3$.

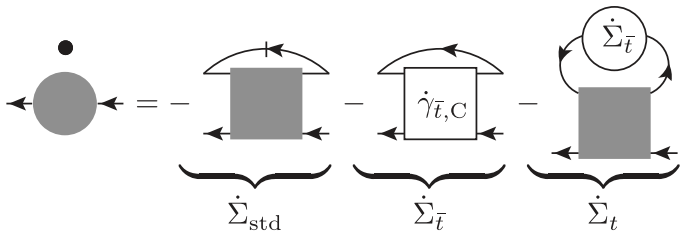

Figure 2.7: Diagrammatic representation of the self-energy flow including the multiloop correction terms. Taken from [1].

Much of the power of the mfRG scheme relies on the fact that the complexity of the objects used throughout is not larger than that of the usual fRG objects. This implies that the computational effort needed to compute an mfRG-flow increases only linearly with the number of loops included. Compared to how the vertex's complexity increases (something we will discuss in depth in the following Chapter), a linear increase in computational cost for loops is extremely good and promising for the predictive power and implementation potential of the method. However, the mfRG does require a full parametrization of the frequency dependence, whereas regular fRG implementations often use only rather simple parametrizations. This concludes our discussion of the functional renormalization group for the purposes of this work. Now we turn out attention to the second major theoretical tool to be used in this thesis: the Keldysh formalism. Formulated on a real-time contour instead of on an imaginary time axis, the formalism allows us to work with systems outside of thermodynamic equilibrium by paying a price in increased complexity.

2.3 Non-equilibrium field theory

Quantum field theoretical methods have long been proved to be some of the most versatile in all of physics. Based on the idea of particles being described by excitations in fields, methods of QFT have become powerful tools for describing interacting systems. In the context of condensed matter physics, condensed matter field theory is one of the most widely used tools for theorists. For most of this method's history thermodynamic equilibrium had to be assumed, since the ground state was taken to remain essentially unchanged or expectation values where calculated with respect to an ensemble of states in thermal equilibrium. However, the Keldysh formalism has allowed physicists to work around the assumption of equilibrium and describe much more general systems by formulating a field theory on a real time *contour*. We assume the reader has sufficient knowledge of zero-temperature and of equilibrium field theory and hence we move on to motivate the use of the Keldysh formalism in this context.

2.3.1 The Keldysh formalism

The Keldysh formalism presents a way to think about the problem of calculating expectation values in a many-body theory without requiring thermodynamic equilibrium or a Wick rotation. It is a real-time tool to handle, with field-theoretical methods, much more general systems than those that the Matsubara formalism can describe. This part of the text is based off A. Kamenev's book *Field Theory of Non-Equilibrium Systems* [14].

To start, consider a time-dependent Hamiltonian $\hat{H}(t)$ of an interacting quantum many-body system. We assume that in the distant past $t = -\infty$ the particles are non-interacting, and the interaction is adiabatically turned on. Also, through external fields or boundary conditions, the system can be driven out of equilibrium. The density matrix, with arbitrary initial condition $\hat{\rho}(-\infty)$, evolves according to the von Neumann equation

$$\partial_t \hat{\rho} = -i[\hat{H}(t), \hat{\rho}(t)]\,. \tag{2.33}$$

Together with a unitary time evolution operator $\hat{\mathcal{U}}_{t,t'} = \mathbb{T}\exp\left(-i\int_{t'}^{t}\hat{H}\left(t''\right)\mathrm{d}t''\right)$, where the $\mathbb{T}$ stands for time-ordered, one can calculate the expectation value of any operator $\hat{\mathcal{O}}$ like (recall Eq. (2.9))

$$\begin{aligned}\langle\hat{\mathcal{O}}\rangle(t) \equiv \frac{\mathrm{Tr}\{\hat{\mathcal{O}}\hat{\rho}(t)\}}{\mathrm{Tr}\{\hat{\rho}(t)\}} &= \frac{1}{\mathrm{Tr}\{\hat{\rho}(t)\}}\,\mathrm{Tr}\left\{\hat{\mathcal{U}}_{-\infty,t}\hat{\mathcal{O}}\hat{\mathcal{U}}_{t,-\infty}\hat{\rho}(-\infty)\right\} \\ &= \frac{1}{\mathrm{Tr}\{\hat{\rho}(-\infty)\}}\,\mathrm{Tr}\left\{\hat{\mathcal{U}}_{-\infty,+\infty}\hat{\mathcal{U}}_{+\infty,t}\hat{\mathcal{O}}\hat{\mathcal{U}}_{t,-\infty}\hat{\rho}(-\infty)\right\}\end{aligned} \tag{2.34}$$

Equation (2.34) includes the $\hat{\mathcal{U}}_{-\infty,+\infty}\hat{\mathcal{U}}_{+\infty,t}$, which means that, instead of simply evolving the system from $t = -\infty$ until t and then returning it to $t = -\infty$, the system is evolved first until time $t = \infty$ only to be brought back to $t = -\infty$. We also make use of the trivial $\hat{\mathcal{U}}_{t,+\infty}\hat{\mathcal{U}}_{+\infty,t} = \hat{1}$.

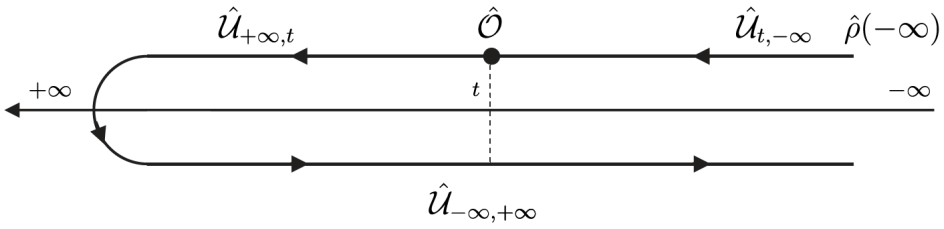

Figure 2.8: Time contour. Notice the evolution past time t to $t \to \infty$ to then return to the starting time $t = -\infty$. Taken from [14].

What is done in zero-temperature field theory, where the last time evolution is left out, is to assume that the ground state of the free theory evolves adiabatically and, hence, changes at most up to a phase during the whole evolution process from the time where the theory was free ($t \to -\infty$) to the time where it becomes free again ($t \to \infty$). The point to be made is that, since the inclusion of the interactions is done adiabatically, no extra change than the inclusion of a phase can be performed on the ground state of the theory and, hence,

$$\hat{\mathcal{U}}_{+\infty,-\infty}|0\rangle \stackrel{!}{=} e^{-iL}|0\rangle \tag{2.35}$$

where $|0\rangle$ is the ground state of the *free* theory. Thus, the expectation value of an operator for a zero-temperature field theory can be calculated as [14]

$$\begin{aligned}\langle \mathrm{GS}|\hat{\mathcal{O}}(t)|\mathrm{GS}\rangle &= \left\langle 0 \left| \hat{\mathcal{U}}_{-\infty,t}\hat{\mathcal{O}}\hat{\mathcal{U}}_{t,-\infty} \right| 0 \right\rangle = \mathrm{e}^{-iL} \left\langle 0 \left| \mathrm{e}^{iL}\hat{\mathcal{U}}_{-\infty,t}\hat{\mathcal{O}}\hat{\mathcal{U}}_{t,-\infty} \right| 0 \right\rangle \\ &= \mathrm{e}^{-iL} \left\langle 0 \left| \hat{\mathcal{U}}_{+\infty,-\infty}\hat{\mathcal{U}}_{-\infty,t}\hat{\mathcal{O}}\hat{U}_{t,-\infty} \right| 0 \right\rangle = \frac{\left\langle 0 \left| \hat{\mathcal{U}}_{+\infty,t}\hat{\mathcal{O}}\hat{\mathcal{U}}_{t,-\infty} \right| 0 \right\rangle}{\left\langle 0 \left| \hat{\mathcal{U}}_{+\infty,-\infty} \right| 0 \right\rangle}\end{aligned} \tag{2.36}$$

where $|\mathrm{GS}\rangle$ stands for the ground state of the interacting theory.

In other words, one is saved the need to close the contour by the fact that one can assume that the ground state emerges unchanged from the evolution. The argument also stands if one replaces $|0\rangle$ by an average over a thermal ensemble of states, since this remains closed under the time evolution. Thus, finite-temperature field theory is also limited to boundary conditions which preserve thermodynamic equilibrium.

Time evolution outside of equilibrium may transport $|0\rangle$ to a state $|0'\rangle$ such that $|| \langle 0, 0' \rangle || \neq 1$. However, a practical advantage that working with the closed time contour has over the zero temperature or the equilibrium formalisms is that time evolution along the contour $\hat{\mathcal{U}}_{\mathcal{C}} = \hat{\mathcal{U}}_{-\infty,+\infty}\hat{\mathcal{U}}_{+\infty,-\infty}$ yields a unit partition function $\mathcal{Z} \equiv \mathrm{Tr}\left\{\hat{\mathcal{U}}_c\hat{\rho}(-\infty)\right\} / \mathrm{Tr}\{\hat{\rho}(-\infty)\} = 1$.

Now, since the time contour can be traversed forwards as well as backwards in time, the Hamiltonian $\hat{H}(t)$ should be modified to include a source term $\hat{H}_V^{\pm}(t) \equiv \hat{H}(t) \pm \mathcal{O}V(t)$ where the plus stands for the forward part of the contour and vice versa. Through the

inclusion of V , $\hat{\mathcal{U}}_{\mathcal{C}} \neq 1$ and hence

$$\mathcal{Z}[V] \equiv \frac{\mathrm{Tr}\left\{\hat{\mathcal{U}}_{\mathcal{C}}[V]\hat{\rho}(-\infty)\right\}}{\mathrm{Tr}\{\hat{\rho}(-\infty)\}} \tag{2.37}$$

is the non-trivial generating functional for observables, since their expectation value can be calculated as $\langle\hat{\mathcal{O}}(t)\rangle = (\mathrm{i}/2)\delta\mathcal{Z}[V]/\delta V(t)|_{V=0}$.

Propagators in the Keldysh formalism

How one comes from here to a field theoretical, path integral description is, in essence, the standard time-slicing procedure used in the derivation of the usual path integral formulation of field theories. However, time is now a two-way contour and one-particle operators must include a time index, signaling in which branch of the contour they should be inserted. In field theory language, this translates to there existing the Grassmann fields $\psi^{\pm}$ and $\bar{\psi}^{\pm}$ for fermionic fields or complex-valued fields $\phi^{\pm}$ and $\bar{\phi}^{\pm}$ for bosonic fields, with the $+$-fields being inserted on the forward part of the contour and the $-$-fields on the other. Since we are interested in purely electronic systems, we will specialize the present discussion to Grassmann fields.

As with any field theoretical method, one is interested in calculating expectations values of the form

$$f\left(t_1', \ldots, t_n', t_1, \ldots, t_n\right) = \left\langle \psi\left(t_1\right) \ldots \psi\left(t_n\right) \bar{\psi}\left(t_1'\right) \ldots, \bar{\psi}\left(t_n'\right)\right\rangle \tag{2.38}$$

Including the $\pm$-indices of the time contour yields 2^{2n} possible combinations for each n-particle operator. In the case of the simplest one-particle operator in a single level, non-interacting fermion system in thermal equilibrium[1], one then obtains four different possibilities, namely

$$\left\langle \psi^{+}(t)\bar{\psi}^{-}\left(t'\right)\right\rangle \equiv iG^{<}\left(t,t'\right) = -n_{\mathrm{F}} \exp\left\{-i\epsilon_0\left(t-t'\right)\right\} \tag{2.39a}$$

$$\left\langle \psi^{-}(t)\bar{\psi}^{+}\left(t'\right)\right\rangle \equiv iG^{>}\left(t,t'\right) = \left(1-n_{\mathrm{F}}\right) \exp\left\{-i\epsilon_0\left(t-t'\right)\right\} \tag{2.39b}$$

$$\left\langle \psi^{+}(t)\bar{\psi}^{+}\left(t'\right)\right\rangle \equiv iG^{\mathbb{T}}\left(t,t'\right) = \theta\left(t-t'\right) iG^{>}\left(t,t'\right) + \theta\left(t'-t\right) iG^{<}\left(t,t'\right) \tag{2.39c}$$

$$\left\langle \psi^{-}(t)\bar{\psi}^{-}\left(t'\right)\right\rangle \equiv iG^{\tilde{\mathbb{T}}}\left(t,t'\right) = \theta\left(t'-t\right) iG^{>}\left(t,t'\right) + \theta\left(t-t'\right) iG^{<}\left(t,t'\right) \tag{2.39d}$$

These four combinations of are called, in order, lesser, greater, time-ordered and anti-time-ordered propagator because of the kind of correlations they describe. In these equations, $n_F \equiv \rho\left(\epsilon_0\right) / \left(1+\rho\left(\epsilon_0\right)\right)$ stands for the Fermi occupation number, $\rho\left(\epsilon_0\right) = \mathrm{e}^{(\epsilon_0-\mu)/T}$, ϵ_0 is the energy of the level and μ is the chemical potential with respect to which ϵ_0 is given.

Inspection of Eq. (2.39) yields that not all four combinations can be independent. As a matter of fact,

$$G^{\mathbb{T}}\left(t,t'\right) + G^{\tilde{\mathbb{T}}}\left(t,t'\right) - G^{>}\left(t,t'\right) - G^{<}\left(t,t'\right) = 0\,. \tag{2.40}$$

[1]The assumption of thermal equilibrium is needed to be able to assign a temperature to the system and use the Fermi distribution.

This suggests that a linear transformation in "Keldysh space" may benefit from this relation, and this is exactly what the famed Keldysh rotation achieves. Now, at this stage one has two possibilities when handling fermions: one can follow the not-too-widespread Larkin–Ovchinnikov convention of transforming the bar fields differently than the non-bared ones or transform them according to the transformation rules for bosons (remember that $\bar{\psi}$ and ψ are independent fields, but $\bar{\phi}$ and ϕ are not). The benefits of the Larkin–Ovchinnikov transformation are that the matrix structure of the Green's functions as well as their inverses and that of the self-energy is equal in every case, whereas in the bosonic case the order of the components is shifted in every case. However, since the convention of transforming bar and regular fields in the same way is more widespread and it also applies for bosons with no extra complication, we opt for the latter.

This means we define new fields

$$\begin{aligned} \psi^1(t) &= \frac{1}{\sqrt{2}}\left(\psi^+(t) - \psi^-(t)\right), \quad \psi^2(t) = \frac{1}{\sqrt{2}}\left(\psi^+(t) + \psi^-(t)\right) \\ \bar{\psi}^1(t) &= \frac{1}{\sqrt{2}}\left(\bar{\psi}^+(t) - \bar{\psi}^-(t)\right), \quad \bar{\psi}^2(t) = \frac{1}{\sqrt{2}}\left(\bar{\psi}^+(t) + \bar{\psi}^-(t)\right). \end{aligned} \tag{2.41}$$

In the particular case of bosons, the indices 2 and 1 are changed with the letters c and q respectively, which stand for *classical* and *quantum*, respectively. These names only apply in the bosonic case, since there is no such thing as a classical fermion.

Now, the power of this transformation can be seen when arranging the components in a propagator matrix,

$$\langle \bar{\psi}^\alpha(t)\psi^\beta(t')\rangle \equiv iG^{\alpha|\beta}(t,t') = i\begin{pmatrix} 0 & G^{1|2}(t,t') \\ G^{2|1}(t,t') & G^{2|2}(t,t') \end{pmatrix} \equiv i\begin{pmatrix} 0 & G^A(t,t') \\ G^R(t,t') & G^K(t,t') \end{pmatrix}. \tag{2.42}$$

The fact that $G^{1|1} = 0$ is a consequence of Eq. (2.40), which is interpreted as a causality condition [14]. The superscripts R, A, and K stand for *retarded*, *advanced* and *Keldysh* components of the Green's function. These three Green functions are the fundamental objects of the Keldysh technique. The retarded and advanced components get their name from their causality structure, whereas the Keldysh component does not have a clear interpretation in these terms. Notably,

$$\left[G^R\right]^\dagger = G^A \quad \left[G^K\right]^\dagger = -G^K \tag{2.43}$$

where we understand the propagators as matrices in the time domain. This means that the Keldysh component of the propagator must be purely imaginary.

Both retarded and advanced matrices have non-zero main diagonals, meaning that $G^{(R/A)}(t,t) \neq 0$ but

$$G^R(t,t) + G^A(t,t) = 0 \tag{2.44}$$

is satisfied for all t. This consideration is completely general and paramount to keep in mind.

For time-translation invariant systems, one may use the frequency representation of the Green's functions. For completeness, we state the energy-representation version of the previous equation, which reads

$$\int \frac{\mathrm{d}\nu}{2\pi} \left(G^R(\nu) + G^A(\nu) \right) = 0 \,. \tag{2.45}$$

Fourier transforming the analytic expressions of $G^{\alpha|\beta}$, one obtains

$$G^R\left(t,t'\right) = -\mathrm{i}\theta\left(t-t'\right) \mathrm{e}^{-\mathrm{i}\epsilon_0(t-t')} \overset{\mathrm{FT}}{\to} \left(\epsilon - \epsilon_0 + \mathrm{i}0\right)^{-1} \tag{2.46a}$$

$$G^A\left(t,t'\right) = \mathrm{i}\theta\left(t'-t\right) \mathrm{e}^{-\mathrm{i}\epsilon_0(t-t')} \overset{\mathrm{FT}}{\to} \left(\epsilon - \epsilon_0 - \mathrm{i}0\right)^{-1} \tag{2.46b}$$

$$G^K\left(t,t'\right) = -\mathrm{i}\left(1-2n_{\mathrm{F}}\right) \mathrm{e}^{-\mathrm{i}\epsilon_0(t-t')} \overset{\mathrm{FT}}{\to} -2\pi\mathrm{i}\left(1-2n_{\mathrm{F}}\right)\delta\left(\epsilon-\epsilon_0\right) \tag{2.46c}$$

Equation (2.46c) can be rewritten as

$$G^K(\nu) = \tanh\left(\frac{\nu-\mu}{2T}\right)\left[G^R(\nu) - G^A(\nu)\right] \tag{2.47}$$

This result is known as the fluctuation-dissipation theorem (FDT), which is a generic feature of systems in thermal equilibrium. Thus, it provides a check for the correctness of numerical calculations.

Until this point in this section we have considered a non-interacting system and, hence, G_0 has been equal to G the whole time and no need for distinction has been necessary. However, since we are interested in interacting systems, we start differentiating a free propagator (either G_0 or g) from a full, dressed one denoted by G, and we specialize this discussion to our case of study, Anderson's single-impurity model.

Keldysh bare propagators in the single-impurity Anderson model For the case of a model in which the single level is hybridized, as is the single-impurity Anderson model, the frequency representation of the dot propagator is modified to include the total hybridization Γ of the level, which comes from the interaction with the left and right reservoirs [7]

$$g^R(\nu) = \frac{1}{\nu - \epsilon + \mathrm{i}\Gamma/2} \tag{2.48a}$$

$$g^A(\nu) = \left[g^R\right]^* \tag{2.48b}$$

$$g^K(\nu) = \left[1 - 2n_{\mathrm{eff}}(\nu)\right]\left[g^R(\nu) - g^A(\nu)\right] \tag{2.48c}$$

where Γ_L and Γ_R are set to the same constant and $\Gamma = \Gamma_L + \Gamma_R$ (as in Sec. 2.1), the effective distribution of the dot is $n_{\mathrm{eff}}\left(\nu\right) = \frac{\Gamma_L n_L(\nu) + \Gamma_R n_R(\nu)}{\Gamma_L + \Gamma_R}$, and the ones from the reservoirs are defined as

$$n_r(\nu) = \frac{1}{e^{(\nu-\mu_r)/T}+1}, \quad r = L, R \tag{2.49}$$

for respective chemical potentials μ_r for each reservoir. We measure the energy with respect to the mean chemical potential, which means we set $\mu_L + \mu_R = 0$ and, although the temperature of the reservoirs are taken to be the same, their relative bias voltage is set by $eV_g = \mu_L - \mu_R$.

It is also common to write the retarded propagators of the SIAM expressed with $\Delta = \frac{\Gamma}{2}$ [16]

$$g^R(\nu) = \frac{1}{\nu - \epsilon + \mathrm{i}\Delta}\,. \tag{2.50}$$

Seemingly trivial as this point, the inclusion of Δ will later be of great importance when considering the mfRG solution of the model.

The self-energy and the dressed propagators in the Keldysh formalism

For interacting systems the propagators of the fields must be modified due to how the interactions change the way the excitations of the field behave. This is accounted for by the inclusion of the self-energy. As a one-particle object, the self-energy has two Keldysh indices. A very non-trivial fact is that it also inherits the causality structure of G_0^{-1}, which is different from that of G_0 [2]. The causality condition $G^{1|1} = 0$ implies $\Sigma^{2|2} = 0$. This yields

$$\Sigma^{\alpha|\beta} = \begin{pmatrix} \Sigma^{1|1} & \Sigma^{1|2} \\ \Sigma^{2|1} & \Sigma^{2|2} \end{pmatrix} = \begin{pmatrix} \Sigma^K & \Sigma^R \\ \Sigma^A & 0 \end{pmatrix}\,. \tag{2.51}$$

Indeed, similar equations as for the propagators are also fulfilled for the self-energy, namely

$$\left[\Sigma^R\right]^\dagger = \Sigma^A \quad \left[\Sigma^K\right]^\dagger = -\Sigma^K\,. \tag{2.52}$$

This again provides us with a check condition, namely that the real part of Keldysh component of the self-energy must always be zero. These properties make Eq. (2.43) apply also for dressed propagators.

To get the equations that determine the dressed propagators, one must solve the matrix equation

$$\left(G_0^{-1} - \Sigma\right) \circ G = \mathbf{1}\,, \tag{2.53}$$

which comes from establishing a Dyson series for the dressed propagator of the interacting theory. This equation implies that all the information of the dressed propagators is contained in the self-energy and vice versa. Furthermore, the retarded and advanced components of the self-energy are conventionally related to their respective propagators, i.e.

$$G^{R/A}(\nu) = \left(\nu - \epsilon - \Sigma^{R/A}(\nu) \pm i0^+\right)^{-1}\,. \tag{2.54}$$

The same cannot be about the Keldysh component of the dressed propagator. For it, one finds that

$$G^K(\nu) = G^R(\nu)\left(\Sigma^K(\nu)\right)G^A(\nu)\,. \tag{2.55}$$

[2] G_0^{-1} is the inverse matrix of G_0, and not the matrix of the inverses.

However, in thermal equilibrium, a version of the FDT applies for the Keldysh component and

$$G^K(\nu) = \tanh\left(\frac{\nu-\mu}{2T}\right)\left[G^R(\nu) - G^A(\nu)\right] , \tag{2.56}$$

which, in turn, yields

$$\Sigma^K(\nu) = \tanh\left(\frac{\nu-\mu}{2T}\right)\left[\Sigma^R(\nu) - \Sigma^A(\nu)\right] . \tag{2.57}$$

Dressed propagators in the single-impurity Anderson model For the particular case of the single-impurity Anderson model, the regulator $\mathrm{i}0^+$ is naturally replaced by one half of the level's hybridization. Hence, one has

$$G^{R/A}(\nu) = \left(\nu - \epsilon - \Sigma^{R/A}(\nu) \pm i\frac{\Gamma}{2}\right)^{-1} = \left(\nu - \epsilon - \Sigma^{R/A}(\nu) \pm i\Delta\right)^{-1} . \tag{2.58}$$

For the Keldysh propagator the inclusion of an extra term modifying Σ^K is also necessary, yielding

$$G^K(\nu) = G^R(\nu)\left(\Sigma^K(\nu) - \mathrm{i}\Gamma\right)G^A(\nu) = G^R(\nu)\left(\Sigma^K(\nu) - 2\mathrm{i}\Delta\right)G^A(\nu) . \tag{2.59}$$

Vertices in the Keldysh formalism

In the present work, motivated by the fRG-truncation of the infinite hierarchy of irreducible vertices, we only focus on how these two are treated in the Keldysh formalism. Clearly, a consistent treatment can be given to more complex objects within this formalism, but this is outside of the scope and need of this work.

The vertices are, in essence, objects of the form

$$\left[G^{(4)}\right]^{\alpha_{1'}\alpha_{2'}|\alpha_1\alpha_2} \sim \left\langle \bar{\psi}^{\alpha_1}\bar{\psi}^{\alpha_2}\psi^{\alpha_{1'}}\psi^{\alpha_{2'}}\right\rangle \tag{2.60}$$

whose exact derivation is done by diagrammatic methods and is left to the books. The appearance of a Keldysh index $\alpha_i \in \{1,2\}$ for every one of the four field operators raises the number of Keldysh components to a total of 16. In this case and, in general for all vertices,

$$G^{1\ldots|\ldots1} \Rightarrow \Gamma^{2\ldots|\ldots2} = 0 , \tag{2.61}$$

a generalization of Eq. (2.40).

Much of the complexity of the Keldysh formalism in this thesis has to do with dealing with $\Gamma^{(4)} \equiv \Gamma$. No general simplification other than that given by Eq. (2.61) can be said in general about any component of the vertex. Furthermore, the components themselves do not possess a clear analytical structure that can be identified with concepts like retarded or advanced, though progress is rapidly being done in our group in understanding the causality structure of these components. The analytic examination of this object is a topic of current research.

Numbering of the components To be able to refer to the components of the vertex $\Gamma^{\alpha_{1'}\alpha_{2'}|\alpha_1\alpha_2}$ in a more concrete way, we convert the indices $\alpha_{1'}\alpha_{2'} \mid \alpha_1\alpha_2$ to numbers in the set $\mathcal{N} := \{0, 1, \ldots, 15\}$ according to the following scheme

$$\begin{array}{ll} \Gamma^{11|11} \longleftrightarrow \Gamma^{0} & \Gamma^{21|11} \longleftrightarrow \Gamma^{8} \\ \Gamma^{11|12} \longleftrightarrow \Gamma^{1} & \Gamma^{21|12} \longleftrightarrow \Gamma^{9} \\ \Gamma^{11|21} \longleftrightarrow \Gamma^{2} & \Gamma^{21|21} \longleftrightarrow \Gamma^{10} \\ \Gamma^{11|22} \longleftrightarrow \Gamma^{3} & \Gamma^{21|22} \longleftrightarrow \Gamma^{11} \\ \Gamma^{12|11} \longleftrightarrow \Gamma^{4} & \Gamma^{22|11} \longleftrightarrow \Gamma^{12} \\ \Gamma^{12|12} \longleftrightarrow \Gamma^{5} & \Gamma^{22|12} \longleftrightarrow \Gamma^{13} \\ \Gamma^{12|21} \longleftrightarrow \Gamma^{6} & \Gamma^{22|21} \longleftrightarrow \Gamma^{14} \\ \Gamma^{12|22} \longleftrightarrow \Gamma^{7} & \Gamma^{22|22} \longleftrightarrow \Gamma^{15} = 0 \end{array} \tag{2.62}$$

This allows us to refer to the components in the matrix as, e.g. "the 7^{th} component", where now it is unambiguously clear that the element referred to is $\Gamma^{12|22}$.

The correspondence is implemented by the formula

$$\begin{aligned} i_{\mathcal{N}} &= 2^3 (\alpha_{1'} - 1) + 2^2 (\alpha_{2'} - 1) + 2^1 (\alpha_1 - 1) + 2^0 (\alpha_2 - 1) \\ &= 8 (\alpha_{1'} - 1) + 4 (\alpha_{2'} - 1) + 2 (\alpha_1 - 1) + (\alpha_2 - 1) \, . \end{aligned} \tag{2.63}$$

There is also an inverse function for this, which involves using both the floor and the mod functions:

$$\begin{aligned} \alpha_2 &= \left\lfloor \frac{(i_{\mathcal{N}} \bmod 2)}{1} \right\rfloor + 1 = (i_{\mathcal{N}} \bmod 2) + 1 \\ \alpha_1 &= \left\lfloor \frac{(i_{\mathcal{N}} \bmod 4)}{2} \right\rfloor + 1 \\ \alpha_{2'} &= \left\lfloor \frac{(i_{\mathcal{N}} \bmod 8)}{4} \right\rfloor + 1 \\ \alpha_{1'} &= \left\lfloor \frac{(i_{\mathcal{N}} \bmod 16)}{8} \right\rfloor + 1 \end{aligned} \tag{2.64}$$

Keldysh structure of the bare vertex in the single-impurity Anderson model

As we did above with the free propagators we do now for the bare vertex of the single-impurity Anderson model, and specify the discussion to this model. The important fact to point out here is that this object has non-trivial Keldysh as well as spin structure. This structure is as follows [7]:

$$[\Gamma_0]^{\alpha_{1'}\alpha_{2'}|\alpha_1\alpha_2}_{\sigma_1'\sigma_{2'}|\sigma_1\sigma_2} = \begin{cases} \frac{1}{2} [\Gamma_0]_{\sigma_{1'}\sigma_{2'}|\sigma_1\sigma_2} \, , & \text{if } \alpha_{1'} + \alpha_{2'} + \alpha_1 + \alpha_2 \text{ is odd,} \\ 0 \, , & \text{else,} \end{cases} \tag{2.65}$$

with

$$[\Gamma_0]_{\sigma_{1'}\sigma_{2'}|\sigma_1\sigma_2} = \begin{cases} U \, , & \text{if } \sigma_{1'} = \sigma_1 = \bar{\sigma}_{2'} = \bar{\sigma}_2 \, , \\ -U \, , & \text{if } \sigma_{1'} = \bar{\sigma}_1 = \bar{\sigma}_{2'} = \sigma_2 \, , \text{ and} \\ 0 \, , & \text{else.} \end{cases}$$

Compared to [7] we introduce a global minus sign in Γ_0. This is motivated from the Matsubara formalism where it is convenient to have $e^{-S} = e^{\cdots + \Gamma_0 \cdots}$. The fact that the sum of all the Keldysh indices must be odd is a consequence of the interaction being local in time. It is important to keep this fact in mind, since it will have a crucial impact in the decomposition analysis of the vertex, which we will present in Chapter 3.

This concludes the discussion of the Keldysh formalism to the extent needed in this work. In the next section we briefly discuss how one can join both the scheme of the mfRG and that of the Keldysh formalism. This will, in most cases, be a straightforward task thanks to our adopted multi-index notation, with a notable exception coming from the bubbles, whose Keldysh structure is worth exploiting as much as possible.

2.4 The Keldysh mfRG formalism

The unification of physical schemes and calculation methods is a common task in theoretical physics. Whenever a useful and widely applicable formalism allows for application with another, a generalized joint methodology may be fruitful. In this case, we want to perform this union of the functional renormalization group with the Keldysh formalism, motivated by the fact that the mfRG solves some of the issues of the fRG and working in the Keldysh formalism allows one to overcome problems of the Matsubara formalism. Most important is the fact that both ideas are compatible with one another: the fRG needs only a functional representation of the partition function and the inclusion of an arbitrary cut-off scale Λ, and the Keldysh formalism needs only a well-defined action to calculate expectation values on the time contour. The objects of this joint formalism will include both a Λ-dependency as well as Keldysh indices $\alpha_i \in \{1, 2\}$.

From Section 2.2 we already have the flow equations we need, namely Eq. (2.24) together with Eq. (2.25) and Eq. (2.32). Notice that the definitions of the functions B and L with sums over multi-indices allows us to expand the definition automatically to include a summation over Keldysh indices. This means that, with no extra theoretical effort, we have obtained the Keldysh mfRG equations! Now we study the structure of these equations and where some simplifications may be made.

2.4.1 Keldysh structure of the bubbles

In our discussion of the Keldysh formalism we showed the Keldysh structure of the propagator, the self-energy and the vertex. The Keldysh structure of bubbles Π_r is inherited from the propagators, which fulfill $G^{1|1} = 0$. Thus, if one expresses Π_r as a 4×4 matrix, many of the entries will automatically be zero. We therefore adopt the following convention

$$\Pi\left(\nu_1, \nu_2\right)^{\alpha_1\alpha_2|\alpha_{1'}\alpha_{2'}} = G^{\alpha_1|\alpha_{1'}}\left(\nu_1\right) G^{\alpha_2|\alpha_{2'}}\left(\nu_2\right) . \tag{2.66}$$

With this convention, written in matrix notation,

$$\Pi\left(\nu_1,\nu_2\right)^{\alpha_1\alpha_2|\alpha_{1'}\alpha_{2'}} = \begin{pmatrix} \Pi^0\left(\nu_1,\nu_2\right) & \Pi^1\left(\nu_1,\nu_2\right) & \Pi^2\left(\nu_1,\nu_2\right) & \Pi^3\left(\nu_1,\nu_2\right) \\ \Pi^4\left(\nu_1,\nu_2\right) & \Pi^5\left(\nu_1,\nu_2\right) & \Pi^6\left(\nu_1,\nu_2\right) & \Pi^7\left(\nu_1,\nu_2\right) \\ \Pi^8\left(\nu_1,\nu_2\right) & \Pi^9\left(\nu_1,\nu_2\right) & \prod^{10}\left(\nu_1,\nu_2\right) & \Pi^{11}\left(\nu_1,\nu_2\right) \\ \Pi^{12}\left(\nu_1,\nu_2\right) & \Pi^{13}\left(\nu_1,\nu_2\right) & \Pi^{14}\left(\nu_1,\nu_2\right) & \Pi^{15}\left(\nu_1,\nu_2\right) \end{pmatrix} \tag{2.67}$$

$$= \begin{pmatrix} 0 & 0 & 0 & G^A\left(\nu_1\right)G^A\left(\nu_2\right) \\ 0 & 0 & G^A\left(\nu_1\right)G^R\left(\nu_2\right) & G^A\left(\nu_1\right)G^K\left(\nu_2\right) \\ 0 & G^R\left(\nu_1\right)G^A\left(\nu_2\right) & 0 & G^K\left(\nu_1\right)G^A\left(\nu_2\right) \\ G^R\left(\nu_1\right)G^R\left(\nu_2\right) & G^R\left(\nu_1\right)G^K\left(\nu_2\right) & G^K\left(\nu_1\right)G^R\left(\nu_2\right) & G^K\left(\nu_1\right)G^K\left(\nu_2\right) \end{pmatrix}. \tag{2.68}$$

This structure is also inherited by $\dot{\Pi}_r$, replacing GG by $\partial_\Lambda(GG)$.

Notice that the causality condition automatically implies that seven out of the 16 total possibilities are zero. Hence, in an equation of the sort

$$\gamma_r \sim \Gamma \circ \Pi_r \circ \Gamma\,, \tag{2.69}$$

every combination of Keldysh indices of the left hand side implies a sum over only a total of 9 terms as opposed to 16. Also, it's important to point out that this simplification applies to all channels. Now, the only issue is that a channel-dependent way of determining the Keldysh indices of Eq. (2.69) is needed. In other words, if one writes the Keldysh indices of Eq. (2.69),

$$\gamma_r^{i_0} \sim \sum_{i_2\in BK} \Gamma^{i_1^r(i_0,i_2)} \circ \Pi_r^{i_2} \circ \Gamma^{i_3^r(i_0,i_2)}\,, \tag{2.70}$$

then determining the functions $i_1(i_0,i_2)$ and $i_3(i_0,i_2)$ is needed.

In the last equation, $BK := \{3,6,7,9,11,12,13,14,15\}$ is the set of Keldysh indices for which the bubbles are non-zero. Writing down the exact form of these functions is a straight-forward task, which requires the conversion of i_0 and i_2 into indices in the $\{11|11,\ldots,22|22\}$ set and then seeing which labels are connected with which in every channel. Thus, following our propagator-vertex primed-unprimed index convention for $i_0 = \alpha_{1'}\alpha_{2'} \mid \alpha_1\alpha_2$ and $i_2 = \alpha_3\alpha_4 \mid \alpha_{3'}\alpha_{4'}$, the functions are as follows:

$$\begin{aligned} i_1^a\left(\alpha_{1'}\alpha_{2'}|\alpha_1\alpha_2,\alpha_3\alpha_4|\alpha_{3'}\alpha_{4'}\right) &= \alpha_{1'}\alpha_{4'}|\alpha_3\alpha_2 \\ i_3^a\left(\alpha_{1'}\alpha_{2'}|\alpha_1\alpha_2,\alpha_3\alpha_4|\alpha_{3'}\alpha_{4'}\right) &= \alpha_{3'}\alpha_{2'}|\alpha_1\alpha_4 \\ i_1^p\left(\alpha_{1'}\alpha_{2'}|\alpha_1\alpha_2,\alpha_3\alpha_4|\alpha_{3'}\alpha_{4'}\right) &= \alpha_{1'}\alpha_{2'}|\alpha_3\alpha_4 \\ i_3^p\left(\alpha_{1'}\alpha_{2'}|\alpha_1\alpha_2,\alpha_3\alpha_4|\alpha_{3'}\alpha_{4'}\right) &= \alpha_{3'}\alpha_{4'}|\alpha_1\alpha_2 \\ i_1^t\left(\alpha_{1'}\alpha_{2'}|\alpha_1\alpha_2,\alpha_3\alpha_4|\alpha_{3'}\alpha_{4'}\right) &= \alpha_{4'}\alpha_{2'}|\alpha_3\alpha_2 \\ i_3^t\left(\alpha_{1'}\alpha_{2'}|\alpha_1\alpha_2,\alpha_3\alpha_4|\alpha_{3'}\alpha_{4'}\right) &= \alpha_{1'}\alpha_{3'}|\alpha_1\alpha_4\,. \end{aligned} \tag{2.71}$$

These can easily be read off of Fig. 2.9d, which is presented with the other diagrammatic representations in Subsection 2.4.2. This result also concludes the derivation of the Keldysh

mfRG since now we exactly know how to calculate the vertex and the self-energy in this framework. However, the difficulty of this task is understated in the harmless appearance of the equations. We will dedicate the coming chapter to developing a deeper understanding of the vertex function, how to best parametrize it and decompose it. However, we first present the diagrammatic tools we use for this purpose.

2.4.2 Diagrammatic representation

Since the appearance of Feynman diagrams in 1948, field theoretical methods have relied on diagrammatic methods to graphically represent both physical processes and complicated mathematical equations in an accessible manner. We do the same for the objects in this work and, thus, develop a diagrammatic representation, with some useful conventions, for this purpose. Thus, we specialize the multi-indices we have been using until now to our case, in which we have Λ-dependent quantities with Keldysh indices, spin and frequency dependency, making this discussion for zero-dimensional systems with time-translation invariance. Thus, for an n-particle quantity X_β labeled by a multi-index β, the following replacement works:

$$X_\beta \to \left[X^\Lambda\right]^{\alpha_1\ldots\alpha_n|\alpha_{1'}\ldots\alpha_{n'}}_{\sigma_1\ldots\sigma_n|\sigma'_1\ldots\sigma_{n'}} (\nu_1,\ldots\nu_n \mid \nu_{1'},\ldots,\nu_{n'}) \text{ or} \tag{2.72}$$

$$X_\beta \to \left[X^\Lambda\right]^{\alpha_{1'}\ldots\alpha_{n'}|\alpha_1\ldots\alpha_n}_{\sigma'_1\ldots\sigma_{n'}|\sigma_1\ldots\sigma_n} (\nu_{1'},\ldots\nu_{n'} \mid \nu_1,\ldots,\nu_n)\ , \tag{2.73}$$

depending on whether X is a propagator- or a vertex-like quantity, respectively. We note that the inclusion of momenta do not change the notation and would just add arguments in parenthesis.

Following the order presented in Sec. 2.3, we begin with the propagators. Due to energy conservation, it's clear that the propagators must be diagonal in frequency space. They must also be diagonal in spin space, since spin is also a conserved quantity.

$$G = G^{1|1'} = G^{\alpha_1|\alpha_{1'}}_\sigma(\nu)\,. \tag{2.74}$$

The self-energy is also trivially diagonal in frequency and spin space,

$$\Sigma = \Sigma^{1'|1} = \Sigma^{\alpha_{1'}|\alpha_1}_\sigma(\nu)\,. \tag{2.75}$$

As two-particle objects, the vertex has two incoming and two outgoing legs and, hence, four entries in each parameter. Since energy must be conserved, only three of the four frequencies are independent. Also spin must be conserved. Now, for the arrows' directions of the vertex we follow the convention of [1, 2, 19].

The general form of the vertex is

$$\Gamma = \Gamma^{1'2'|12} = \Gamma^{\alpha_{1'}\alpha_{2'}|\alpha_1\alpha_2}_{\sigma_{1'}\sigma_{2'}|\sigma_1\sigma_2} (\nu_{1'},\nu_{2'},\nu_1,\nu_2)\ . \tag{2.76}$$

The bubbles then appear as the connectors of the legs of two vertices. These are semi-diagonal in spin and frequency, since each propagator is,

$$\Pi = \Pi^{34|3'4'} = \Pi^{\alpha_3\alpha_4|\alpha_{3'}\alpha_{4'}}_{\sigma_1,\sigma_2} (\nu_1,\nu_2) \tag{2.77}$$

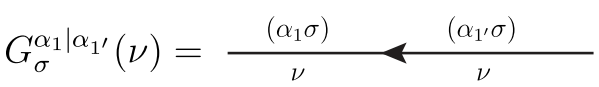

(a) Graphical representation of the propagator.

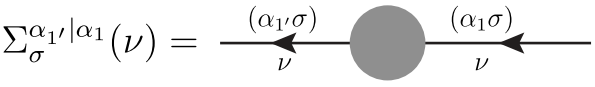

(b) Graphical representation of the self-energy.

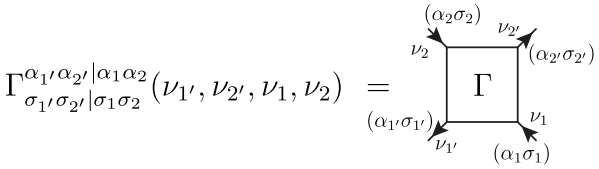

(c) Graphical representation of the vertex. Notice the chosen convention for the position of the incoming and outgoing legs, as well as indices.

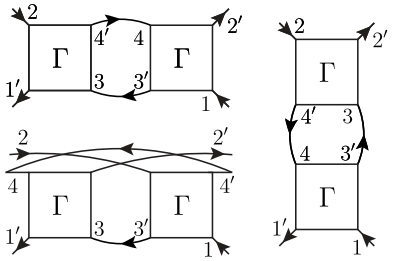

(d) Diagrammatic representation of the equation $\Gamma \circ \Pi \circ \Gamma$, depicting how the propagator lines of each bubble are respectively connected to the vertices depending on the channel.

Since the model we are considering is SU(2)-spin invariant, the spin indices will be omitted in all objects but the vertices.

This concludes the present Chapter. All theoretical tools have been presented and all diagrammatic methods and conventions have been explained. However, the main task of the present work remains, which consists of analyzing and decomposing the vertex into manageable parts. This task is what the coming Chapter is about.

Chapter 3

Parametrization of the vertex

In Chapter 2 we presented the multiloop functional renormalization group and the Keldysh formalism. We then combined these into a joint framework which, in principle, allows for a method to calculate dynamical quantities of non-equilibrium systems. But so much flexibility and wide-applicability does not come easy. The analytical solution of even the truncated system of equations for the self-energy and the vertex is out of question. Hence, the only way to tackle the problem is numerically. However, if this is done without analyzing and simplifying the problem, the task is unfeasible. Thus we dedicate this Chapter to the study of the most challenging part of the task: the calculation of the vertex. Hence, we dissect it into more manageable parts to be able to compute it as efficiently as possible. First, we will look at a channel decomposition, based on the two-particle reducibility of certain diagrams. Then we turn to a diagrammatic decomposition of the vertex, based on the number of arguments the vertex function effectively depends on, to then go further and explore the implications of certain symmetries that the bare vertex has, due to its Keldysh structure, on these diagrammatic classes. These dependencies will however be subject to some assumptions, which will be explained later on.

3.1 Channel-dependent frequency parametrization

To fully get the most of the channel decomposition, one has to define a corresponding frequency parametrization, which exploits the natural dependency of each channel on a specific argument combination (recall Eq. (2.13)). Each one of the three interaction channels is describing a two-fermion interaction so the exchange frequency will be bosonic (distinguished from the fermionic ones by using ω instead of ν). Also, since each interaction must separately conserve momentum, only a total of three frequencies is needed. Thus one has

$$\begin{aligned}\Gamma\left(\nu_{1'},\nu_{2'},\nu_1,\nu_2\right) = R\left(\nu_{1'},\nu_{2'},\nu_1\right) + \\ \sum_{r\in\{a,p,t\}} \gamma_r\left(\omega_r\left(\nu_{1'},\nu_{2'},\nu_1\right),\nu_r\left(\nu_{1'},\nu_{2'},\nu_1\right),\nu_r'\left(\nu_{1'},\nu_{2'},\nu_1\right)\right) .\end{aligned} \tag{3.1}$$

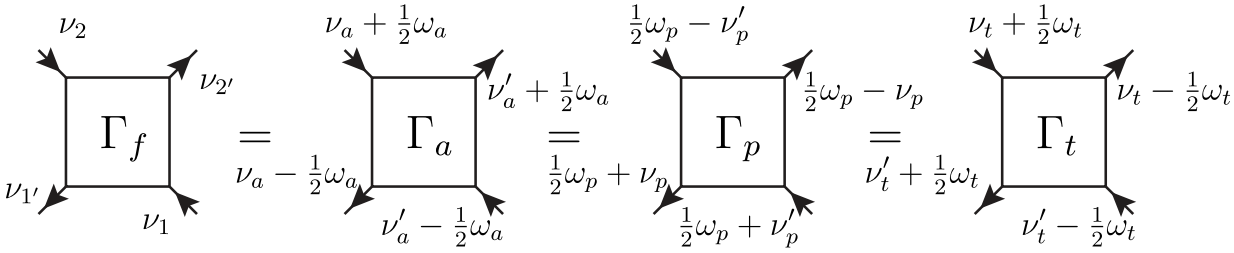

Figure 3.1: Frequency parametrization for each channel. Notice the conventions refer to the full vertex Γ, which can be parametrized in every channel r or expressed as function of the usual parameters. This latter form is denoted by Γ_f, where the f stands for "fermionic".

The frequencies in Fig. 3.1 lead then to the following conversion rules between the channels, where the conventional vertex depicted in Fig. 2.9c is referred to as the 'fermionic' vertex, Γ_f, and the vertex, parametrized in the r channel is denoted by Γ_r:

a **channel** From and to the fermionic channel:

$$\left.\begin{aligned}\nu_{1'} &= \nu_a - \tfrac{1}{2}\omega_a\\ \nu_{2'} &= \nu'_a + \tfrac{1}{2}\omega_a\\ \nu_1 &= \nu'_a - \tfrac{1}{2}\omega_a\end{aligned}\right\} \Longrightarrow \begin{cases}\omega_a = \nu_2 - \nu_{1'} = \nu_{2'} - \nu_1\\ \nu_a = \frac{1}{2}\left(\nu_{1'} + \nu_2\right) = \frac{1}{2}\left(2\nu_{1'} + \nu_{2'} - \nu_1\right)\\ \nu'_a = \frac{1}{2}\left(\nu_{2'} + \nu_1\right)\end{cases} \tag{3.2}$$

And from any other channel to the a channel:

$$\begin{array}{lll}\omega_a = \omega_a & \omega_a = -\nu_p - \nu'_p & \omega_a = \nu_t - \nu'_t\\ \nu_a = \nu_a & \nu_a = \frac{1}{2}\left(\omega_p + \nu_p - \nu'_p\right) & \nu_a = \frac{1}{2}\left(\omega_t + \nu_t + \nu'_t\right)\\ \nu'_a = \nu'_a & \nu'_a = \frac{1}{2}\left(\omega_p - \nu_p + \nu'_p\right) & \nu'_a = \frac{1}{2}\left(-\omega_t + \nu_t + \nu'_t\right)\end{array} \tag{3.3}$$

p **channel** From and to the fermionic channel:

$$\left.\begin{aligned}\nu_{1'} &= \tfrac{1}{2}\omega_p + \nu_p\\ \nu_{2'} &= \tfrac{1}{2}\omega_p - \nu_p\\ \nu_1 &= \tfrac{1}{2}\omega_p + \nu'_p\end{aligned}\right\} \Longrightarrow \begin{cases}\omega_p = \nu_1 + \nu_2 = \nu_{1'} + \nu_{2'}\\ \nu_p = \frac{1}{2}\left(\nu_{1'} - \nu_{2'}\right)\\ \nu'_p = \frac{1}{2}\left(\nu_1 - \nu_2\right) = \frac{1}{2}\left(2\nu_1 - \nu_{1'} - \nu_{2'}\right)\end{cases} \tag{3.4}$$

And from any other channel to the p channel:

$$\begin{array}{lll}\omega_p = \nu_a + \nu'_a & \omega_p = \omega_p & \omega_p = \nu_t + \nu'_t\\ \nu_p = \frac{1}{2}\left(-\omega_a + \nu_a - \nu'_a\right) & \nu_p = \nu_p & \nu_p = \frac{1}{2}\left(\omega_t - \nu_t + \nu'_t\right)\\ \nu'_p = \frac{1}{2}\left(-\omega_a - \nu_a + \nu'_a\right) & \nu'_p = \nu'_p & \nu'_p = \frac{1}{2}\left(-\omega_t - \nu_t + \nu'_t\right)\end{array} \tag{3.5}$$

t **channel** From and to the fermionic channel:

$$\left.\begin{aligned}\nu_{1'} &= \nu'_t + \tfrac{1}{2}\omega_t\\ \nu_{2'} &= \nu_t - \tfrac{1}{2}\omega_t\\ \nu_1 &= \nu'_t - \tfrac{1}{2}\omega_t\end{aligned}\right\} \Longrightarrow \begin{cases}\omega_t = \nu_{1'} - \nu_1 = \nu_2 - \nu_{2'}\\ \nu_t = \frac{1}{2}\left(\nu_{2'} + \nu_2\right) = \frac{1}{2}\left(2\nu_{2'} + \nu_{1'} - \nu_1\right)\\ \nu'_t = \frac{1}{2}\left(\nu_{1'} + \nu_1\right)\end{cases} \tag{3.6}$$

And from any other channel to the t channel:

$$\begin{array}{lll} \omega_t = \nu_a - \nu'_a & \omega_t = \nu_p - \nu'_p & \omega_t = \omega_t \\ \nu_t = \frac{1}{2}\left(\omega_a + \nu_a + \nu'_a\right) & \nu_t = \frac{1}{2}\left(\omega_p - \nu_p - \nu'_p\right) & \nu_t = \nu_t \\ \nu'_t = \frac{1}{2}\left(-\omega_a + \nu_a + \nu'_a\right) & \nu'_t = \frac{1}{2}\left(\omega_p + \nu_p + \nu'_p\right) & \nu'_t = \nu'_t \end{array} \tag{3.7}$$

3.2 Diagrammatic decomposition

The next decomposition strategy we follow is based on [5]. The basic idea is classifying the diagrams according to the number of input frequencies they effectively depend on. To motivate this discussion, we consider first the following fact: if all three frequency arguments are taken to infinity the contributions of any diagram must vanish (except that of the bare vertex, which will be hence excluded of the discussion). However, there are some diagrams which do not depend on all but only on a subset of the frequencies. This means that these will not vanish if the complementary subset of frequencies is taken to infinity. Hence, we first define for every channel $r \in \{a, p, t\}$ the class of diagrams which only depend on the bosonic exchange frequency, namely

$$\left(\mathcal{K}_1^r\right)^{\alpha_{1'}\alpha_{2'}|\alpha_1\alpha_2}_{\sigma_{1'}\sigma_{2'}|\sigma_1\sigma_2}\left(\omega_r\right) := \lim_{|\nu_r|\to\infty}\lim_{|\nu'_r|\to\infty}\left(\gamma_r\right)^{\alpha_{1'}\alpha_{2'}|\alpha_1\alpha_2}_{\sigma_{1'}\sigma_{2'}|\sigma_1\sigma_2}\left(\omega_r, \nu_r, \nu'_r\right) . \tag{3.8}$$

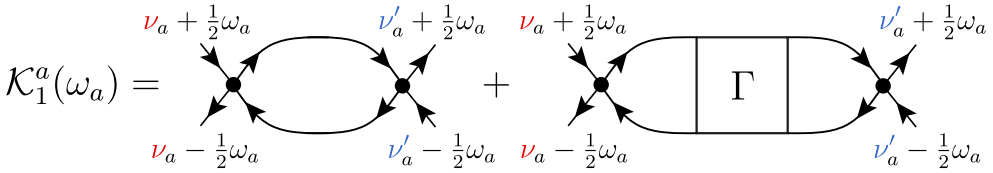

Figure 3.2: Schematic representation of the diagrammatic class $\mathcal{K}_1^a$. The diagrammatic definition for the other channels follows the same pattern, namely $\mathcal{K}_1^r = \Gamma_0 \circ \Pi_r \circ \Gamma_0 + \Gamma_0 \circ \Pi_r \circ \Gamma \circ \Pi_r \circ \Gamma_0$.

This class of diagrams corresponds to the ones in which the incoming and outgoing legs associated with ν_r and, in turn, with ν'_r are connected to the same bare vertex. In this diagrammatic sense, which can be appreciated in Fig. 3.2, both ν_a and ν'_a directly flow in and out of the diagram and, hence, the result cannot depend explicitly on either of them. Similar diagrams can be defined for the p and t channels.

In Eq. (3.8) the order the order in which the limits are taken does not matter. This leads us to the definition of the following two diagrammatic classes, $\mathcal{K}_2$ and $\mathcal{K}_{2'}$,

$$\left(\mathcal{K}_2^r\right)^{\alpha_{1'}\alpha_{2'}|\alpha_1\alpha_2}_{\sigma_{1'}\sigma_{2'}|\sigma_1\sigma_2}\left(\omega_r, \nu_r\right) := \lim_{|\nu'_r|\to\infty}\left(\gamma_r\right)^{\alpha_{1'}\alpha_{2'}|\alpha_1\alpha_2}_{\sigma_{1'}\sigma_{2'}|\sigma_1\sigma_2}\left(\omega_r, \nu_r, \nu'_r\right) - \left(\mathcal{K}_1^r\right)^{\alpha_{1'}\alpha_{2'}|\alpha_1\alpha_2}_{\sigma_{1'}\sigma_{2'}|\sigma_1\sigma_2}\left(\omega_r\right) , \tag{3.9a}$$

$$\left(\mathcal{K}_{2'}^r\right)^{\alpha_{1'}\alpha_{2'}|\alpha_1\alpha_2}_{\sigma_{1'}\sigma_{2'}|\sigma_1\sigma_2}\left(\omega_r, \nu'_r\right) := \lim_{|\nu_r|\to\infty}\left(\gamma_r\right)^{\alpha_{1'}\alpha_{2'}|\alpha_1\alpha_2}_{\sigma_{1'}\sigma_{2'}|\sigma_1\sigma_2}\left(\omega_r, \nu_r, \nu'_r\right) - \left(\mathcal{K}_1^r\right)^{\alpha_{1'}\alpha_{2'}|\alpha_1\alpha_2}_{\sigma_{1'}\sigma_{2'}|\sigma_1\sigma_2}\left(\omega_r\right) . \tag{3.9b}$$

The fact that the order in which the limits in Eq. (3.8) are taken is irrelevant yields then the consistency condition

$$\lim_{|\nu_r|\to\infty} \left(\mathcal{K}_2^r\right)_{\sigma_{1'}\sigma_{2'}|\sigma_1\sigma_2}^{\alpha_{1'}\alpha_{2'}|\alpha_1\alpha_2}(\omega_r,\nu_r) \overset{!}{=} \lim_{|\nu'|\to\infty} \left(\mathcal{K}_{2'}^r\right)_{\sigma_{1'}\sigma_{2'}|\sigma_1\sigma_2}^{\alpha_{1'}\alpha_{2'}|\alpha_1\alpha_2}(\omega_r,\nu_r') \overset{!}{=} 0\,. \tag{3.10}$$

Diagrammatically, the $\mathcal{K}_{2^{(\prime)}}$ classes look as in Fig. 3.3 and have the characteristic to have either the first or the second fermionic frequency flow right out of the diagram while the other one does not directly flow in and out, i.e. the pair of legs that depend on $\nu_r^{(\prime)}$ are connected to two *different* bare vertices. These two classes correspond to contributions to the vertex in order $\mathcal{O}(U^3)$ and all include at least one nested loop.

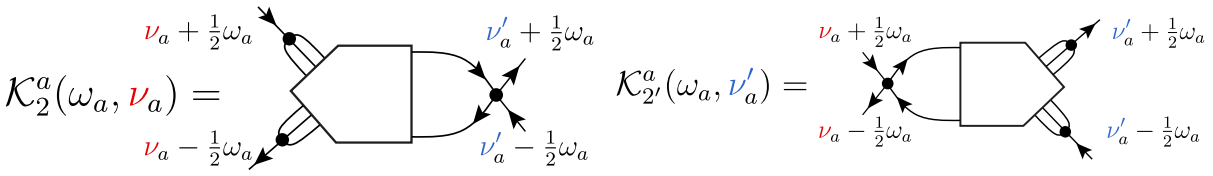

Figure 3.3: Diagrammatic representation of the $\mathcal{K}_{2^{(\prime)}}^a$ classes, where the legs which depend on ν_a and ν_a' respectively are connected to different bare vertices and, thus, the whole diagram depends on the fermionic frequency. Channels p and t follow the same convention.

The remaining class is defined through the subtraction of the $\mathcal{K}_1$- and $\mathcal{K}_{2^{(\prime)}}$ classes from the full vertex and, hence, it retains a full frequency dependence. It contains only diagrams of $\mathcal{O}(U^4)$ with at least two nested loops and, diagrammatically, is defined as the collection of diagrams in which each leg is connected to a different bare vertex, see Fig. 3.4

$$\begin{aligned}\left(\mathcal{K}_3^r\right)_{\sigma_{1'}\sigma_{2'}|\sigma_1\sigma_2}^{\alpha_{1'}\alpha_{2'}|\alpha_1\alpha_2}(\omega_r,\nu_r,\nu_r') := \Big[&\left(\gamma_r(\omega_r,\nu_r,\nu_r')\right)_{\sigma_{1'}\sigma_{2'}|\sigma_1\sigma_2}^{\alpha_{1'}\alpha_{2'}|\alpha_1\alpha_2} - \left(\mathcal{K}_1^r\right)(\omega_r)_{\sigma_{1'}\sigma_{2'}|\sigma_1\sigma_2}^{\alpha_{1'}\alpha_{2'}|\alpha_1\alpha_2} - \\ &- \left(\mathcal{K}_2^r\right)_{\sigma_{1'}\sigma_{2'}|\sigma_1\sigma_2}^{\alpha_{1'}\alpha_{2'}|\alpha_1\alpha_2}(\omega_r,\nu_r) - \left(\mathcal{K}_{2'}^r\right)_{\sigma_{1'}\sigma_{2'}|\sigma_1\sigma_2}^{\alpha_{1'}\alpha_{2'}|\alpha_1\alpha_2}(\omega_r,\nu_r')\Big]\end{aligned} \tag{3.11}$$

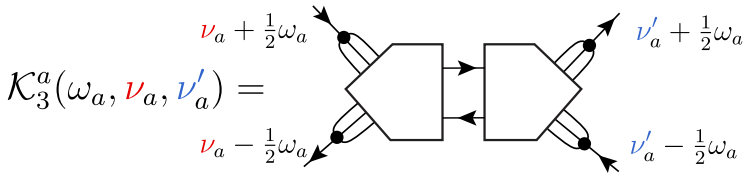

Figure 3.4: Diagrammatic representation of the $\mathcal{K}_3^a$ class, where each leg is connected to a different bare vertex and, hence, the diagram depends on all frequencies. Channels p and t follow the same convention.

All three[1] classes respect the channel decomposition of the parquet formalism of Sec. 2.2.1. This implies that there are, in total, 12 vertex functions to be determined, $\mathcal{K}_i^r$

[1] We are clustering $\mathcal{K}_2$ and $\mathcal{K}_{2'}$ into one kind of diagrammatic class.

with $i \in \{1, 2, 2', 3\}$ and $r \in \{a, p, t\}$. The above-mentioned fact also implies that this diagrammatic decomposition only applies to 2 -PR diagrams and hence does not help to improve on the PA. With all this taken into account, the full vertex fulfills

$$\Gamma(\nu_{1'}, \nu_{2'}, \nu_1, \nu_2) = R + \sum_{r\in\{a,p,t\}} [\mathcal{K}_1^r(\omega_r) + \mathcal{K}_2^r(\omega_r, \nu_r) + \mathcal{K}_{2'}^r(\omega_r, \nu_r') + \mathcal{K}_3^r(\omega_r, \nu_r, \nu_r')] \quad (3.12)$$

where $R = \Gamma_0$ in the PA and the bosonic and both fermionic frequencies, $\omega_r\left(\nu_{1'}, \nu_{2'}, \nu_1\right), \nu_r\left(\nu_{1'}, \nu_{2'}, \nu_1\right), \nu_r'\left(\nu\right.$ depend on the fermionic input frequencies following the channel conversion rules of the previous section.

Physical interpretation

A priori one could think that this diagrammatic decomposition of the vertex is performed purely for numerical gain. However, it is much more than that, since the $\mathcal{K}_i$'s have a physical interpretation [5].

First of all, each $\mathcal{K}_1$-object is a one-particle bosonic object, which turns out to be the susceptibility in the corresponding channel [20],

$$\mathcal{K}_1^r(\omega) = -U^2\chi^r(\omega)\,. \quad (3.13)$$

More notable is the fact that the charge and spin susceptibilities are also expressible in terms of $\mathcal{K}_1$ objects. Following [23],

$$\chi_{\mathrm{ch/sp}} = \chi_{\uparrow\uparrow} \pm \chi_{\uparrow\downarrow}\,, \quad (3.14)$$

$$\chi_{\sigma\sigma'} \simeq -\delta_{\sigma\sigma'}\Pi_t + \Pi_t \circ \Gamma \circ \Pi_t \mathrel{\hat{=}} -\frac{1}{U^2}\mathcal{K}_1^t\,. \quad (3.15)$$

where the last equality is best understood in the light of the graphical depiction of this equation (Fig. 3.5).

Hence,

$$U^2\chi_{\mathrm{ch/sp}} = \mathcal{K}_{\uparrow\uparrow}^t \mp \mathcal{K}_{1\uparrow\downarrow}^t\,. \quad (3.16)$$

Now, we state as a fact that, in the Keldysh formalism[2],

$$\mathcal{K}_{1\uparrow\uparrow}^t = \mathcal{K}_{1\uparrow\downarrow}^t - \mathcal{K}_{1\uparrow\downarrow}^a\,. \quad (3.17)$$

Thus,

$$\chi_{\mathrm{sp}} = -\frac{1}{U^2}\mathcal{K}_{1\uparrow\downarrow}^a \quad \chi_{\mathrm{ch}} = \frac{1}{U^2}\left(2\mathcal{K}_{1\uparrow\downarrow}^t - \mathcal{K}_{1\uparrow\downarrow}^a\right)\,, \quad (3.18)$$

and the spin and charge susceptibilities are directly related to the $\mathcal{K}_1$-objects in channels a and t.

[2]This applies only to an SU(2)-spin symmetric system and is a relation that can be derived with tools shown later.

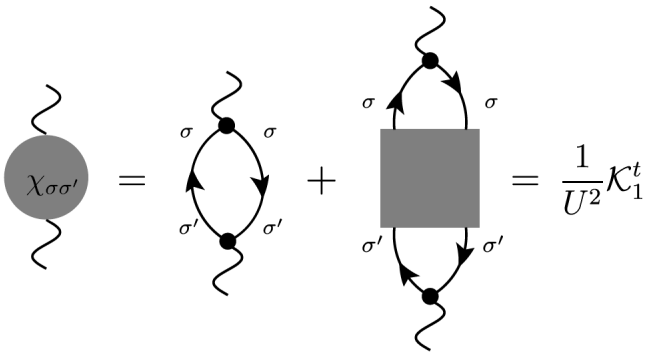

Figure 3.5: Susceptibility in the t channel. Notice this follows directly from the definition of $\mathcal{K}_1^t$.

In turn, the $\mathcal{K}_2$ and $\mathcal{K}_{2'}$ encode information on the coupling of the fermionic degrees of freedom with the bosonic ones. Returning to a setting with full generality (i.e. space-time four vectors), there is a relation for the generalized density in Fourier space

$$n_q = \sum\!\!\!\!\!\!\int \mathrm{d}k \sum_\sigma c_\sigma^\dagger(k) c(k+q) \tag{3.19}$$

relating it to the $\mathcal{K}_1$ and $\mathcal{K}_2$ classes:

$$U \times \left\langle \mathbb{T}\left\{ n_q c_\sigma(k+q) c_\sigma^\dagger(k) \right\} \right\rangle_c = G_\sigma(k) G_\sigma(k+q) \sum_{\sigma'} \left([\mathcal{K}_1^a]_{\sigma\sigma'|\sigma\sigma'}(q) + [\mathcal{K}_2^a]_{\sigma\sigma'|\sigma\sigma'}(q,k) \right) . \tag{3.20}$$

Here $\langle \ldots \rangle_c$ considers only connected diagrams. For theories which have electron-boson vertices, Eq. (3.20) identifies the expectation value of an operator directly related to this coupling with the sum of the $\mathcal{K}_1$ and $\mathcal{K}_2$ classes.

3.3 Keldysh structure of the $\mathcal{K}_i$'s

In the previous section we explained the decomposition of the vertex into diagrammatic classes and how that remains compatible with the channel decomposition, summarized in Eq. (3.12). A key observation is that the Keldysh and spin structure of the full vertex carries over to the individual components.

Spin structure of the vertex Up until now, we have tried to be as general as possible regarding indices and input frequencies. However, to delve deeper into the decomposition, we now study the possible spin interactions that are possible, in order to manage the *a priori* 16 different combinations for $\sigma_{1'}\sigma_{2'}|\sigma_1\sigma_2$.

The fact that spin must be conserved at the bare-vertex level implies overall spin conservation,

$$\sigma_{1'} + \sigma_{2'} = \sigma_1 + \sigma_2 \, . \tag{3.21}$$

This is satisfied by only three $\mathbb{Z}_2$-equivalent variants: $\sigma\sigma|\sigma\sigma$, $\sigma\bar{\sigma}|\sigma\bar{\sigma}$ and $\sigma\bar{\sigma}|\bar{\sigma}\sigma$, where $\bar{\sigma} = \downarrow$ if $\sigma = \uparrow$ and vice versa. SU(2)-spin-symmetry further implies that [20]

$$\Gamma_{\sigma\sigma|\sigma\sigma} = \Gamma_{\sigma\bar{\sigma}|\sigma\bar{\sigma}} + \Gamma_{\sigma\bar{\sigma}|\bar{\sigma}\sigma} \,. \tag{3.22}$$

Thus, a system which respects SU(2)-spin-symmetry needs only the calculation of two different spin components for its full characterization, for which we define specific symbols:

$$V^{\alpha_{1'}\alpha_{2'}|\alpha_1\alpha_2} := \Gamma^{\alpha_{1'}\alpha_{2'}|\alpha_1\alpha_2}_{\sigma\bar{\sigma}|\sigma\bar{\sigma}} \,, \tag{3.23}$$

$$(V_i^r)^{\alpha_{1'}\alpha_{2'}|\alpha_1\alpha_2} := (\mathcal{K}_i^r)^{\alpha_{1'}\alpha_{2'}|\alpha_1\alpha_2}_{\sigma\bar{\sigma}|\sigma\bar{\sigma}} \,, \tag{3.24}$$

$$\hat{V}^{\alpha_{1'}\alpha_{2'}|\alpha_1\alpha_2} := \Gamma^{\alpha_{1'}\alpha_{2'}|\alpha_1\alpha_2}_{\sigma\bar{\sigma}|\bar{\sigma}\sigma} \,, \tag{3.25}$$

$$(\hat{V}_i^r)^{\alpha_{1'}\alpha_{2'}|\alpha_1\alpha_2} := (\mathcal{K}_i^r)^{\alpha_{1'}\alpha_{2'}|\alpha_1\alpha_2}_{\sigma\bar{\sigma}|\bar{\sigma}\sigma} \,. \tag{3.26}$$

For non-SU(2)-symmetric systems this discussion would not be as easy and a more detailed analysis would be required. However, since we focus on a system respecting said symmetry, we consider this discussion sufficient for the present work.

The important takeaway is that through physical constraints and symmetries, the amount of components of the vertex that need to be determined can be reduced. The reduction in the case of the spin is from 16 to, effectively, 2.

3.3.1 Exchange symmetries and complex conjugation

To really begin our discussion of the Keldysh structure of the $\mathcal{K}_i$'s, we first define some transformations on the *full* vertex.

$$T_S\Gamma^{\alpha_{1'}\alpha_{2'}|\alpha_1\alpha_2}_{\sigma_{1'}\sigma_{2'}|\sigma_1\sigma_2}(\nu_{1'},\nu_{2'},\nu_1,\nu_2) := \Gamma^{\alpha_{1'}\alpha_{2'}|\alpha_1\alpha_2}_{\bar{\sigma}_{1'}\bar{\sigma}_{2'}|\bar{\sigma}_1\bar{\sigma}_2}(\nu_{1'},\nu_{2'},\nu_1,\nu_2) \tag{3.27a}$$

$$T_1\Gamma^{\alpha_{1'}\alpha_{2'}|\alpha_1\alpha_2}_{\sigma_{1'}\sigma_{2'}|\sigma_1\sigma_2}(\nu_{1'},\nu_{2'},\nu_1,\nu_2) := \Gamma^{\alpha_{1'}\alpha_{2'}|\alpha_2\alpha_1}_{\sigma_{1'}\sigma_{2'}|\sigma_2\sigma_1}(\nu_{1'},\nu_{2'},\nu_1,\nu_2) \tag{3.27b}$$

$$T_2\Gamma^{\alpha_{1'}\alpha_{2'}|\alpha_1\alpha_2}_{\sigma_{1'}\sigma_{2'}|\sigma_1\sigma_2}(\nu_{1'},\nu_{2'},\nu_1,\nu_2) := \Gamma^{\alpha_{2'}\alpha_{1'}|\alpha_1\alpha_2}_{\sigma_{2'}\sigma_{1'}|\sigma_1\sigma_2}(\nu_{1'},\nu_{2'},\nu_1,\nu_2) \tag{3.27c}$$

$$T_3\Gamma^{\alpha_{1'}\alpha_{2'}|\alpha_1\alpha_2}_{\sigma_{1'}\sigma_{2'}|\sigma_1\sigma_2}(\nu_{1'},\nu_{2'},\nu_1,\nu_2) := \Gamma^{\alpha_{2'}\alpha_{1'}|\alpha_2\alpha_1}_{\sigma_{2'}\sigma_{1'}|\sigma_2\sigma_1}(\nu_{1'},\nu_{2'},\nu_1,\nu_2) \tag{3.27d}$$

$$T_C\Gamma^{\alpha_{1'}\alpha_{2'}|\alpha_1\alpha_2}_{\sigma_{1'}\sigma_{2'}|\sigma_1\sigma_2}(\nu_{1'},\nu_{2'},\nu_1,\nu_2) := \Gamma^{\alpha_1\alpha_2|\alpha_{1'}\alpha_{2'}}_{\sigma_1\sigma_2|\sigma_{1'}\sigma_{2'}}(\nu_{1'},\nu_{2'},\nu_1,\nu_2) \tag{3.27e}$$

In words, T_S amounts to a spin flip, inverting all spins of the incoming and outgoing legs, the T_i 's for $i \in \{1,2,3\}$ exchange the Keldysh and spin indices of either the incoming (T_1), outgoing (T_2) or incoming and outgoing (T_3) legs and T_C exchanges the indices of the incoming with the ones of the outgoing legs. It is important to point out that these operations defined here do not have any effect on the input frequencies, just on the Keldysh and spin indices, and that these transformations form a group, $\mathcal{S}$. We study its structure in Appendix A.

The key observation we make is that some of these transformations (or combinations thereof) actually correspond to symmetries of the vertex itself, once one endows them with a physical interpretation[3].

We notice that the T_1 transformation is equivalent to the topologically trivial operation of exchanging both of the incoming legs of the diagram (as shown schematically in Fig. 3.6a, second equality.). This operation yields a vertex object with an added minus sign for the anti-commutative properties of fermions and switched frequency arguments for the incoming legs, which yields an actual, physical, symmetry relation between two combinations of Keldysh indices,

$$\begin{aligned} T_1\Gamma^{\alpha_{1'}\alpha_{2'}|\alpha_1\alpha_2}_{\sigma_{1'}\sigma_{2'}|\sigma_1\sigma_2}\left(\nu_{1'},\nu_{2'},\nu_1,\nu_2\right) &\overset{\text{Eq. (3.27b)}}{=} \Gamma^{\alpha_{1'}\alpha_{2'}|\alpha_2\alpha_1}_{\sigma_{1'}\sigma_{2'}|\sigma_2\sigma_1}\left(\nu_{1'},\nu_{2'},\nu_1,\nu_2\right) \\ &\overset{!}{=} -\Gamma^{\alpha_{1'}\alpha_{2'}|\alpha_1\alpha_2}_{\sigma'_{1'}\sigma_{2'}|\sigma_1\sigma_2}\left(\nu_{1'},\nu_{2'},\nu_2,\nu_1\right) . \end{aligned} \tag{3.28}$$

If the exchange is done with the outgoing legs (see Fig. 3.6b), one obtains the following relation

$$\begin{aligned} T_2\Gamma^{\alpha_{1'}\alpha_{2'}|\alpha_1\alpha_2}_{\sigma_{1'}\sigma_{2'}|\sigma_1\sigma_2}\left(\nu_{1'},\nu_{2'},\nu_1,\nu_2\right) &\overset{\text{Eq. (3.27c)}}{=} \Gamma^{\alpha_{2'}\alpha_{1'}|\alpha_1\alpha_2}_{\sigma_{2'}\sigma_{1'}|\sigma_1\sigma_2}\left(\nu_{1'},\nu_{2'},\nu_1,\nu_2\right) \\ &\overset{!}{=} -\Gamma^{\alpha_{1'}\alpha_{2'}|\alpha_1\alpha_2}_{\sigma_{1'}\sigma_{2'}|\sigma_1\sigma_2}\left(\nu_{2'},\nu_{1'},\nu_1,\nu_2\right) . \end{aligned} \tag{3.29}$$

Since T_3 is the composition of T_1 and T_2, it should come to no surprise that one obtains

$$\begin{aligned} T_3\Gamma^{\alpha_{1'}\alpha_{2'}|\alpha_1\alpha_2}_{\sigma_{1'}\sigma_{2'}|\sigma_1\sigma_2}\left(\nu_{1'},\nu_{2'},\nu_1,\nu_2\right) &\overset{\text{Eq. (3.27d)}}{=} \Gamma^{\alpha_{2'}\alpha_{1'}|\alpha_2\alpha_1}_{\sigma_{2'}\sigma_{1'}|\sigma_2\sigma_1}\left(\nu_{1'},\nu_{2'},\nu_1,\nu_2\right) \\ &\overset{!}{=} \Gamma^{\alpha_{1'}\alpha_{2'}|\alpha_1\alpha_2}_{\sigma_{1'}\sigma_{2'}|\sigma_1\sigma_2}\left(\nu_{2'},\nu_{1'},\nu_2,\nu_1\right) . \end{aligned} \tag{3.30}$$

For the interpretation of T_C, we rely on the derivation presented in Chap. 3 of [6] or Chap. 3 of [24]. There, the study of the complex conjugation of the vertex function is presented at second-quantized operator level, arriving at

$$\left(\Gamma^{\alpha_{1'}\alpha_{2'}|\alpha_1\alpha_2}_{\sigma_{1'}\sigma_{2'}|\sigma_1\sigma_2}\left(\nu_{1'},\nu_{2'},\nu_1,\nu_2\right)\right)^* = (-1)^{1+\alpha_{1'}+\alpha_{2'}+\alpha_1+\alpha_2}\Gamma^{\alpha_1\alpha_2|\alpha_{1'}\alpha_{2'}}_{\sigma_1\sigma_2|\sigma_{1'}\sigma_{2'}}\left(\nu_1,\nu_2,\nu_{1'},\nu_{2'}\right) . \tag{3.31}$$

Thus one can relate the action of T_C, defined in Eq. (3.27e) to the action of complex conjugation (hence the C as subscript) as

$$\begin{aligned} T_C\Gamma^{\alpha_{1'}\alpha_{2'}|\alpha_1\alpha_2}_{\sigma_{1'}\sigma_{2'}|\sigma_1\sigma_2}\left(\nu_{1'},\nu_{2'},\nu_1,\nu_2\right) &\overset{\text{Eq. (3.27e)}}{=} \Gamma^{\alpha_1\alpha_2|\alpha_{1'}\alpha_{2'}}_{\sigma_1\sigma_2|\sigma_{1'}\sigma_{2'}}\left(\nu_{1'},\nu_{2'},\nu_1,\nu_2\right) \\ &\overset{!}{=} (-1)^{1+\alpha_{1'}+\alpha_{2'}+\alpha_1+\alpha_2}\left[\Gamma^{\alpha_{1'}\alpha_{2'}|\alpha_1\alpha_2}_{\sigma_{1'}\sigma_{2'}|\sigma_1\sigma_2}\left(\nu_1,\nu_2,\nu_{1'},\nu_{2'}\right)\right]^* . \end{aligned} \tag{3.32}$$

As depicted in Fig. 3.6c, diagrammatic interpretation of T_C is possible as a simultaneous flipping of the directions of all arrows, combined with a reflection on an axis cutting

[3]We point out that this discussion is kept at the level of a diagrammatic interpretation intentionally. A more rigorous analysis making use of the explicit definition of the vertex in field theoretical language, i.e. with equations like $T_1\left\langle\bar{\psi}\left(t'_1\right)\bar{\psi}\left(t'_2\right)\psi\left(t_1\right)\psi\left(t_2\right)\right\rangle = -\left\langle\bar{\psi}\left(t'_1\right)\bar{\psi}\left(t'_2\right)\psi\left(t_2\right)\psi\left(t_1\right)\right\rangle$ is definitely possible. However, the diagrammatic techniques deliver more physical insight and remain correct throughout, making more complex and cumbersome methods unnecessary.

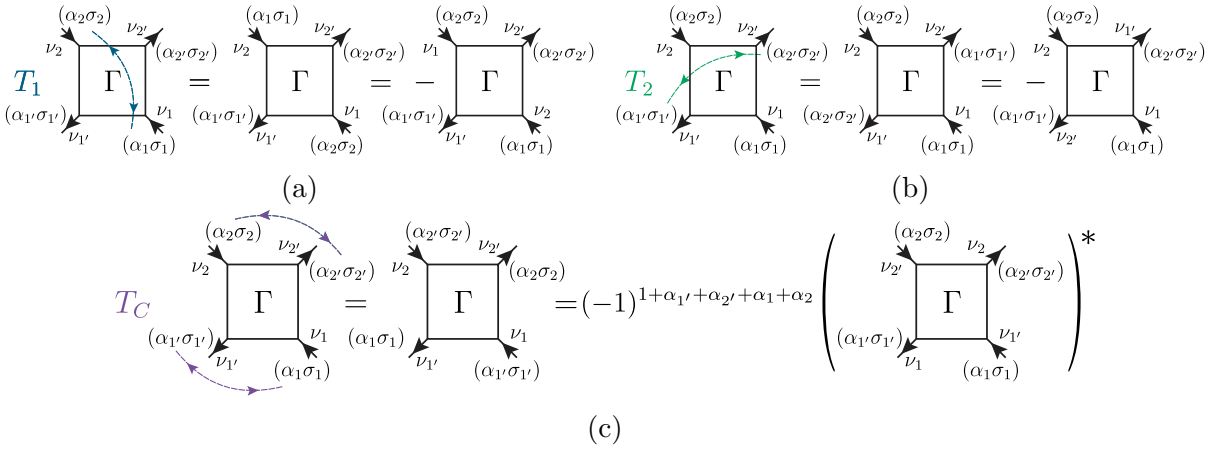

Figure 3.6: Schematic representation of the transformations. Swapping the Keldysh and spin indices of the incoming or outgoing legs and exchanging the incoming or outgoing frequencies are equivalent, up to a minus sign. Time inversion amounts to complex conjugation and the inclusion of a prefactor determined solely by the Keldysh components.

vertically through the diagram. This is usually interpreted as a sort of time reversal symmetry in the diagrammatic sense, though one must be wary of this interpretation in the framework of the Keldysh formalism.

3.3.2 Diagrammatic classes under exchange symmetries and complex conjugation

When considering the diagrammatic classes and the channel decomposition, both decompositions are compatible, not only with one another but also with the underlying Keldysh and spin structure of the vertex. One could also hope that something like this would happen with the diagrammatic classes and the symmetries defined above, i.e. that equations like

$$T_j\left(\mathcal{K}_i^r\left(\nu_{1'},\nu_{2'},\nu_1,\nu_2\right)\right)^{\alpha_{1'}\alpha_{2'}|\alpha_1\alpha_2}_{\sigma_{1'}\sigma_{2'}|\sigma_1\sigma_2} = \left(\mathcal{K}_i^r\right)^{\alpha_{T_j(1')}\alpha_{T_j(2')}|\alpha_{T_j(1)}\alpha_{T_j(2)}}_{\sigma_{T_j(1')}\sigma_{T_j(2')}|\sigma_{T_j(1)}\sigma_{T_j(2)}}\left(\nu_{1'},\nu_{2'},\nu_1,\nu_2\right) \tag{3.33}$$

would hold.

This is however not the case. Thus, we need to delve deeper into the action of the T_j's to derive useful relations within components of the vertex. To do so, we will focus solely on the two spin components of interest, V and $\hat{V}$.

We begin this journey with the action of the whole group on the $\mathcal{K}_i^a$'s and, to do so in a systematic manner, we will go through the generators of $\mathcal{S}$ (see Appendix A), T_1, T_2 and T_C, keeping the discussion as general as possible, as to be able to derive results that apply to all channels or all diagrammatic classes as we go along. First, T_1 on $\mathcal{K}_3^a$. As can be seen in Fig. 3.7a , the swapping of the incoming legs also changes the channel. This is inconvenient, since it means that the diagrammatic classes are not completely compatible

with the physical symmetries of the full vertex. Yet it is also hardly surprising, since the a and t channels are much related to one another [1, 2].

In the case for $\mathcal{K}_2^a$, there are further surprising relations. Note that the defining diagrammatic feature of the $\mathcal{K}_2$ class is that the bare vertex, to the one two outer legs connect to, is on the right side of the diagram (lower part, for t). Thus, when swapping incoming legs from diagrams in the $\mathcal{K}_2^a$, one lands not in the $\mathcal{K}_2^t$ class, but in the $\mathcal{K}_{2'}^t$ class, since the bare vertex ends up in the upper part of the diagram (see Figs. 3.7b and 3.7c).

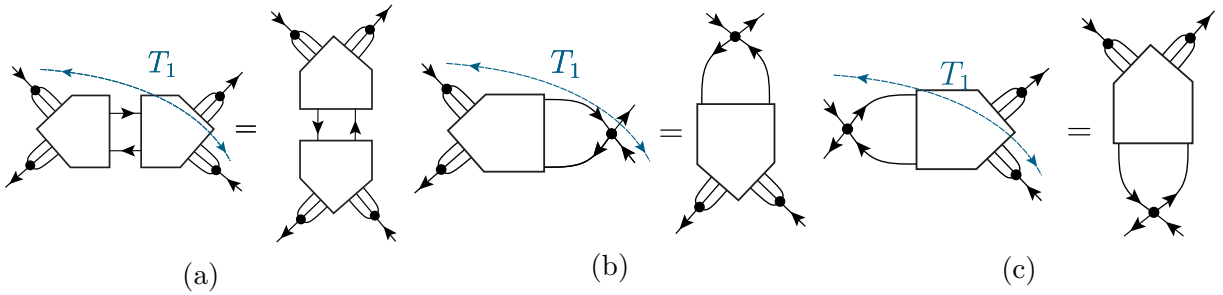

Figure 3.7: Schematic representation of the channel-mixing effect of the T_1 transformation. The Keldysh and spin indices, as well as the input frequencies, transform according to Eq. (3.27b) where special attention has to be paid to the change in frequency parametrization, which is channel dependent.(a) Effect of T_1 on a $\mathcal{K}_3^a$ diagram. (b) T_1 maps $\mathcal{K}_2^a$ to $\mathcal{K}_{2'}^t$. (c) T_1 maps $\mathcal{K}_{2'}^a$ to $\mathcal{K}_2^t$.

Of noticeable importance is the fact that action of T_1 on any $\mathcal{K}_i^r$, not only in the a channel, changes the spin-sector i.e. $T_1(V) \to \hat{V}$ and $T_1(\hat{V}) \to V$, see Fig. 3.8. Phrased mathematically, this is reflected in the fact that

$$T_1(V_i^r)^{\alpha_{1'}\alpha_{2'}|\alpha_1\alpha_2} = T_1\left(\mathcal{K}_i^r\right)^{\alpha_{1'}\alpha_{2'}|\alpha_1\alpha_2}_{\sigma\bar{\sigma}|\sigma\bar{\sigma}} = \left(\mathcal{K}_{T_1(i)}^{T_1(r)}\right)^{\alpha_{1'}\alpha_{2'}|\alpha_2\alpha_1}_{\sigma\bar{\sigma}|\bar{\sigma}\sigma} = (\hat{V}_i^{T_1(r)})^{\alpha_{1'}\alpha_{2'}|\alpha_2\alpha_1} \text{ and} \tag{3.34}$$

$$T_1(\hat{V}_i^r)^{\alpha_{1'}\alpha_{2'}|\alpha_1\alpha_2} = T_1\left(\mathcal{K}_i^r\right)^{\alpha_{1'}\alpha_{2'}|\alpha_1\alpha_2}_{\sigma\bar{\sigma}|\bar{\sigma}\sigma} = \left(\mathcal{K}_{T_1(i)}^{T_1(r)}\right)^{\alpha_{1'}\alpha_{2'}|\alpha_2\alpha_1}_{\sigma\bar{\sigma}|\sigma\bar{\sigma}} = (V_i^{T_1(r)})^{\alpha_{1'}\alpha_{2'}|\alpha_2\alpha_1}\,. \tag{3.35}$$

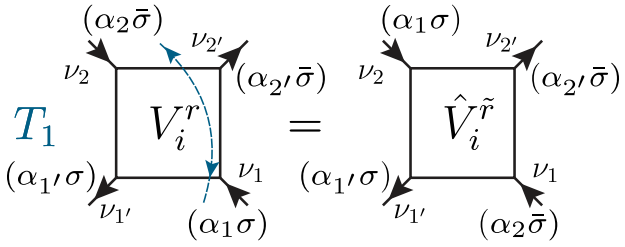

Figure 3.8: Schematic representation of the spin-sector-mixing property of the T_1 transformation. We keep track of the channel-changing properties as well through the inclusion of $\tilde{r} = T_1(r)$, where we abuse the notation of the symmetry to represent the channel to which a diagram of channel r is mapped to.

Regarding T_2, the situation is similar, with the problem that

$$T_2(V_i^r)^{\alpha_{1'}\alpha_{2'}|\alpha_1\alpha_2} = T_2\left(\mathcal{K}_i^r\right)^{\alpha_{1'}\alpha_{2'}|\alpha_1\alpha_2}_{\sigma\bar{\sigma}|\sigma\bar{\sigma}} = \left(\mathcal{K}^{T_2(r)}_{T_2(i)}\right)^{\alpha_{2'}\alpha_{1'}|\alpha_1\alpha_2}_{\bar{\sigma}\sigma|\sigma\bar{\sigma}} \neq (\hat{V}_i^{T_2(r)})^{\alpha_{2'}\alpha_{1'}|\alpha_1\alpha_2} \text{ and} \tag{3.36}$$

$$T_2(\hat{V}_i^r)^{\alpha_{1'}\alpha_{2'}|\alpha_1\alpha_2} = T_2\left(\mathcal{K}_i^r\right)^{\alpha_{1'}\alpha_{2'}|\alpha_1\alpha_2}_{\sigma\bar{\sigma}|\bar{\sigma}\sigma} = \left(\mathcal{K}^{T_2(r)}_{T_2(i)}\right)^{\alpha_{2'}\alpha_{1'}|\alpha_1\alpha_2}_{\bar{\sigma}\sigma|\bar{\sigma}\sigma} \neq (V_i^{T_2(r)})^{\alpha_{2'}\alpha_{1'}|\alpha_1\alpha_2}\,. \tag{3.37}$$

Thus, associated to a T_2 operation must come a T_S operation, so that one safely lands in the V- or the $\hat{V}$-spin sector. Hence, the actual symmetry transformation that needs to be applied is T_ST_2,

$$T_ST_2\left(\mathcal{K}_i^r\right)^{\alpha_{1'}\alpha_{2'}|\alpha_1\alpha_2}_{\sigma\bar{\sigma}|\sigma\bar{\sigma}} = T_S\left(\mathcal{K}^{T_2(r)}_{T_2(i)}\right)^{\alpha_{2'}\alpha_{1'}|\alpha_1\alpha_2}_{\bar{\sigma}\sigma|\sigma\bar{\sigma}} = \left(\mathcal{K}^{T_2(r)}_{T_2(i)}\right)^{\alpha_{2'}\alpha_{1'}|\alpha_1\alpha_2}_{\sigma\bar{\sigma}|\bar{\sigma}\sigma} \text{ and} \tag{3.38}$$

$$T_ST_2\left(\mathcal{K}_i^r\right)^{\alpha'_1\alpha_{2'}|\alpha_1\alpha_2}_{\sigma\bar{\sigma}|\bar{\sigma}\sigma} = T_S\left(\mathcal{K}^{T_2(r)}_{T_2(i)}\right)^{\alpha_{2'}\alpha_{1'}|\alpha_1\alpha_2}_{\bar{\sigma}\sigma|\bar{\sigma}\sigma} = \left(\mathcal{K}^{T_2(r)}_{T_2(i)}\right)^{\alpha_{2'}\alpha_{1'}|\alpha_1\alpha_2}_{\sigma\bar{\sigma}|\sigma\bar{\sigma}}\,. \tag{3.39}$$

Thus, both T_1 and T_ST_2 swap spin sectors. Also easy to see is the case that the composition, namely T_ST_3, does not change the spin sector.

Moreover, for the cases of $\mathcal{K}_1^a$ and $\mathcal{K}_3^a$, one could expect that T_ST_3 maps within the same channel as well, i.e. that $T_ST_3V^a_{1,3} \to V^a_{1,3}$ and the same with $\hat{V}$, which will turn out to be the case. However, we will prove this in due time, when analyzing the orbits of the transformations on the t channel.

To culminate with the generators of $\mathcal{S}$ we follow with the action of T_C acting on $\mathcal{K}_i^a$ As has been mentioned before, T_C as transformation corresponds to flipping the direction of the propagators and, simultaneously, reflecting the diagram with respect to a *vertical* line. Thus, if the diagram has a "bare-vertex asymmetry" in the horizontal direction, T_C will change its character. In the a channel, both the $\mathcal{K}_1$ and the $\mathcal{K}_3$ classes are symmetric in this sense and, thus, $T_C\left(\mathcal{K}^a_{1,3}\right) = \mathcal{K}^a_{1,3}$. This is, however, not the case for the $\mathcal{K}_2^a$ class, which gets mapped to $\mathcal{K}_{2'}^a$ and vice versa, thanks to this asymmetry. Simply said, T_C flips the side at which the bare vertex is and, thus, turns $\mathcal{K}_2^a$ in $\mathcal{K}_{2'}^a$.

Further problematic is the interplay that T_C has with the spin parts. As can be seen in Fig. 3.9a generally T_C maps V to V, but it does not do that for $\hat{V}$. Instead, one needs to include T_S in that case, for it to actually map into $\hat{V}$. This not only carries for the a channel, but is also the case for the other channels.

Now, we have already looked at the generators of $\mathcal{S}$ and characterized their action on the diagrams of the a channel, we are ready to tackle the same challenge regarding the t channel. Given the many similarities between the channels and the fact that already T_1 and T_ST_2 map from a to t, one should expect a similar behavior of the t channel. And, indeed, that is what we observe. As depicted previously on Fig. 3.7a and now also on 3.9b, T_1 and T_ST_2 have the same channel-mapping qualities in the t channel than in the a channel. Thus, one can see that, indeed, $T_ST_3\left(\mathcal{K}_i^{a,t}\right) \to \mathcal{K}_i^{a,t}$, i.e. that T_ST_3 does not mix the channels.

A very subtle but key difference between the a and the t channels comes from the action of T_C. As mentioned before, T_C acts, diagrammatically, by flipping around the arrows and

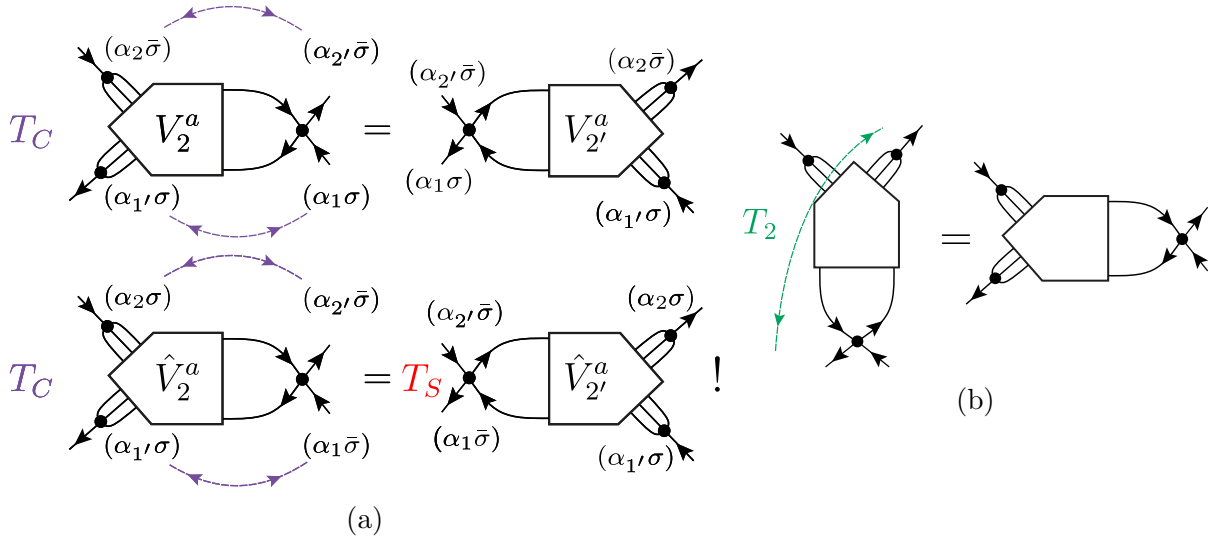

Figure 3.9: (a) Schematic representation of the action of T_C on V_a^a and $\hat{V}_2^a$. (b) Schematic representation of the action of T_2 on a $\mathcal{K}_2^t$ diagram.

mirroring the diagram with respect to a *vertical* line. This implies for the $\mathcal{K}_i^t$ class of diagrams, that there is no mapping from $\mathcal{K}_2^t$ and $\mathcal{K}_{2'}^t$, but rather that

$$\begin{aligned} T_C\mathcal{K}_2^t &\to \mathcal{K}_2^t \text{ and} \\ T_C\mathcal{K}_{2'}^t &\to \mathcal{K}_{2'}^t\,. \end{aligned} \tag{3.40}$$

taking into account which spin sector one starts from. This is consequence of the commutation rule $T_1T_C = T_CT_2$ of these transformations (see App. A).

Lastly, we investigate the action of the transformations on the diagrams of the p channel. Though harder to sketch in the chosen convention (see Fig. 3.10a), T_1, and T_ST_2 do not have a surprising action on $\mathcal{K}_i^p$. This, again, is hardly surprising, since the channel decomposition is exhaustive and the transformations cannot affect the way internal lines lay with respect to one-another i.e. parallel lines remain parallel under the action of any T_i or T_C. Moreover, T_C acts "expectedly" mapping within the bare-vertex-symmetric kinds of diagrams ($\mathcal{K}_1^p$ and $\mathcal{K}_3^p$) and switching between the $\mathcal{K}_2$ and the $\mathcal{K}_{2'}$ classes. Illustration of this action is found in Fig. 3.10c.

3.3.3 Independent Keldysh components of the vertex

The core idea for this section is that the interplay between the Keldysh structure of the bare vertex and the diagrammatic classes may simplify the structure of the vertex and, indeed, it does. Recall that the diagrammatic classes are defined by zero ($\mathcal{K}_3$) , one ($\mathcal{K}_{2^{(\prime)}}$) or two ($\mathcal{K}_1$) pairs of legs connecting to the same bare vertex. Now we recall the Keldysh structure of the bare vertex, introduced in Eq. (2.65). There it was noted that the only requirement for the indices is for the parity of their sum to be odd in order for the bare

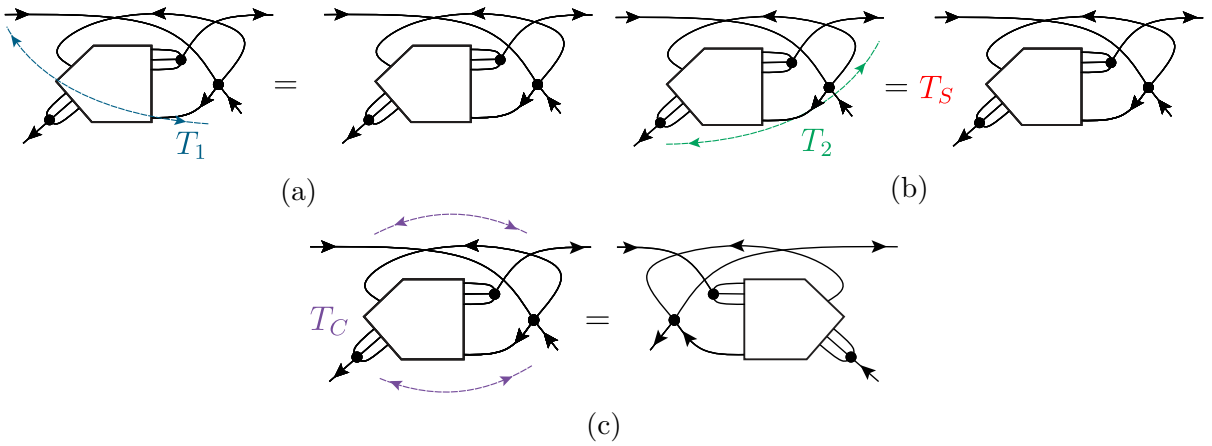

Figure 3.10: Schematic representation of the action of the generators of $\mathcal{S}$ on the $\mathcal{K}_2^p$ class of diagrams.(a) The trivial effect on the structure of T_1 on $\mathcal{K}_{2'}$. (b) The action of $T_S T_2$ preserves the spin structure of the diagram. (c) T_C maps $\mathcal{K}_2^p$ into $\mathcal{K}_{2'}^p$ and vice versa.

vertex to be non-zero. Hence, any change to the indices of the external legs that does not change the parity of the sum is, automatically, a symmetry. Hence, motivated by the respective topological structure of each channel, we define the following six operations on a set of external Keldysh indices of a diagram:

$$\mathcal{P}_L^a\left(\alpha_{1'}\alpha_{2'} \mid \alpha_1\alpha_2\right) = \bar{\alpha}_{1'}\alpha_{2'} \mid \alpha_1\bar{\alpha}_2 \qquad \mathcal{P}_R^a\left(\alpha_{1'}\alpha_{2'} \mid \alpha_1\alpha_2\right) = \alpha_{1'}\bar{\alpha}_{2'} \mid \bar{\alpha}_1\alpha_2 \tag{3.41}$$

$$\mathcal{P}_L^p\left(\alpha_{1'}\alpha_{2'} \mid \alpha_1\alpha_2\right) = \bar{\alpha}_{1'}\bar{\alpha}_{2'} \mid \alpha_1\alpha_2 \qquad \mathcal{P}_R^p\left(\alpha_{1'}\alpha_{2'} \mid \alpha_1\alpha_2\right) = \alpha_{1'}\alpha_{2'} \mid \bar{\alpha}_1\bar{\alpha}_2 \tag{3.42}$$

$$\mathcal{P}_L^t\left(\alpha_{1'}\alpha_{2'} \mid \alpha_1\alpha_2\right) = \alpha_{1'}\bar{\alpha}_{2'} \mid \alpha_1\bar{\alpha}_2 \qquad \mathcal{P}_R^t\left(\alpha_{1'}\alpha_{2'} \mid \alpha_1\alpha_2\right) = \bar{\alpha}_{1'}\alpha_{2'} \mid \bar{\alpha}_1\alpha_2\,. \tag{3.43}$$

In these equations, $\bar{\alpha}_i = 2$ if $\alpha_i = 1$ and vice versa, similar as with $\bar{\sigma}$ and σ. Since any diagram in the t channel does not posses "left" and "right" bare vertices, its "upper" and "lower" vertices are then identified with "left" and "right", respectively, exploiting the $a \leftrightarrow t$ exchange symmetry. This allows for notational simplicity, allowing the grouping $\mathcal{P}_{L/R}^i$.

Clearly, not all classes respect both $\mathcal{P}_{L/R}$ acting on them, but it depends on the sides which have two legs connected to the same bare vertex. We can automatically see that $\mathcal{K}_1$ respects both, $\mathcal{K}_2$ and $\mathcal{K}_{2'}$ respect only $\mathcal{P}_R$ and $\mathcal{P}_L$ respectively and $\mathcal{K}_3$ evidently does not respect these.

These facts imply the following general equations for the vertices:

$$(\mathcal{K}_1^a)^{\alpha_{1'}\alpha_{2'}|\alpha_1\alpha_2} = (\mathcal{K}_1^a)^{\bar{\alpha}_{1'}\alpha_{2'}|\alpha_1\bar{\alpha}_2} = (\mathcal{K}_1^a)^{\alpha_{1'}\bar{\alpha}_{2'}|\bar{\alpha}_1\alpha_2} = (\mathcal{K}_1^a)^{\bar{\alpha}_{1'}\bar{\alpha}_{2'}|\bar{\alpha}_1\bar{\alpha}_2} \tag{3.44a}$$

$$(\mathcal{K}_1^p)^{\alpha_{1'}\alpha_{2'}|\alpha_1\alpha_2} = (\mathcal{K}_1^p)^{\bar{\alpha}_{1'}\bar{\alpha}_{2'}|\alpha_1\alpha_2} = (\mathcal{K}_1^p)^{\alpha_{1'}\alpha_{2'}|\bar{\alpha}_1\bar{\alpha}_2} = (\mathcal{K}_1^p)^{\bar{\alpha}_{1'}\bar{\alpha}_{2'}|\bar{\alpha}_1\bar{\alpha}_2} \tag{3.44b}$$

$$\left(\mathcal{K}_1^t\right)^{\alpha_{1'}\alpha_{2'}|\alpha_1\alpha_2} = \left(\mathcal{K}_1^t\right)^{\alpha_{1'}\bar{\alpha}_{2'}|\alpha_1\bar{\alpha}_2} = \left(\mathcal{K}_1^t\right)^{\bar{\alpha}_{1'}\alpha_{2'}|\bar{\alpha}_1\alpha_2} = \left(\mathcal{K}_1^t\right)^{\bar{\alpha}_{1'}\bar{\alpha}_{2'}|\bar{\alpha}_1\bar{\alpha}_2} \tag{3.44c}$$

$$(\mathcal{K}_2^a)^{\alpha_{1'}\alpha_{2'}|\alpha_1\alpha_2} = (\mathcal{K}_2^a)^{\alpha_{1'}\bar{\alpha}_{2'}|\bar{\alpha}_1\alpha_2} \tag{3.44d}$$

$$(\mathcal{K}_2^p)^{\alpha_{1'}\alpha_{2'}|\alpha_1\alpha_2} = (\mathcal{K}_2^p)^{\alpha_{1'}\alpha_{2'}|\bar{\alpha}_1\bar{\alpha}_2} \tag{3.44e}$$

$$(\mathcal{K}_2^t)^{\alpha_{1'}\alpha_{2'}|\alpha_1\alpha_2} = (\mathcal{K}_2^t)^{\bar{\alpha}_{1'}\alpha_{2'}|\bar{\alpha}_1\alpha_2} \tag{3.44f}$$

$$(\mathcal{K}_{2'}^a)^{\alpha_{1'}\alpha_{2'}|\alpha_1\alpha_2} = (\mathcal{K}_{2'}^a)^{\bar{\alpha}_{1'}\alpha_{2'}|\alpha_1\bar{\alpha}_2} \tag{3.44g}$$

$$(\mathcal{K}_{2'}^p)^{\alpha_{1'}\alpha_{2'}|\alpha_1\alpha_2} = (\mathcal{K}_{2'}^p)^{\bar{\alpha}_{1'}\bar{\alpha}_{2'}|\alpha_1\alpha_2} \tag{3.44h}$$

$$(\mathcal{K}_{2'}^t)^{\alpha_{1'}\alpha_{2'}|\alpha_1\alpha_2} = (\mathcal{K}_{2'}^t)^{\alpha_{1'}\bar{\alpha}_{2'}|\alpha_1\bar{\alpha}_2} \tag{3.44i}$$

Now, this completely exhausts the symmetries, physical or otherwise, that the vertex has in general, though some more exist for more particular cases (particle-hole symmetry and KMS equilibrium conditions, to name two). This means that we are now in the position to combine the action of the T_i and T_C transformations and symmetries with those of $\mathcal{P}^i_{L/R}$ This yields the color-coded Tables 3.1 to 3.5, derived in close collaboration with Elias Walter, of dependent and independent components, with the respective transformations relating them shown whenever needed.

Once one has found which symmetries are respected by the diagrammatic classes and how they behave under their action the derivation and check of this table is, in itself, a straightforward albeit somewhat tedious process. These tables are the main result of this Chapter, since these basically summarize what is needed to be computed in order to have the full information of the Keldysh vertex function. Furthermore, together with the definitions of the symmetries and transformation, they give a thorough guide of the internal Keldysh structure of the full vertex. In the next Chapter, we will then show how we built and implemented a code able to calculate the full vertex and give some technical insights learned in the process, but we first discuss the benefits of doing the tedious work presented here.

Flow equation of the independent Keldysh components As not all Keldysh components are independent, not all of them have to be computed and the convention we settled for is listed in Tables 3.1-3.5. We decided to take this convention in order to give all channels a treatment on equal footing and deal with only one spin component in each. Hence, we now derive the actual flow equations of the relevant components to be calculated.

We consider the spin indices of Eq. (4.6) in the case of it contributing to V_r (the spin components trivially inherit the channel decomposition of the full vertex). Generically,

$$[\dot{\gamma}_r]^{i_0}_{\sigma\bar{\sigma}|\sigma\bar{\sigma}} \equiv \dot{V}_r^{i_0} = \sum_{\sigma_1,\sigma_2} \Gamma_{\sigma\sigma_2|\sigma_1\bar{\sigma}} \circ \left[\dot{\Pi}_r\right]_{\sigma_2,\sigma_1} \circ \Gamma_{\sigma_1,\bar{\sigma}|\sigma\sigma_2} \tag{3.45}$$

Since the full vertex conserves momentum and the propagators are diagonal in spin, the actual way in which the legs are connected and restrict the sum over spins of Eq. (3.45) to either one (in the a and p channels) or two (in the t channel) summands.

For a or p, the flow equation for the independent Keldysh components of the vertex is

$$\dot{V}^{i_0}_{a/p} = \sum_{i_2 \in BK} V^{i_1^r(i_0,i_2)} \circ \dot{\Pi}^{i_2}_{a/p} \circ V^{i_3^r(i_0,i_2)} \,, \tag{3.46}$$

whereas the flow equation for the t channel does include both components

$$\dot{V}^{i_0}_{t} = \sum_{i_2 \in BK} (V+\hat{V})^{i_1^r(i_0,i_2)} \circ \dot{\Pi}^{i_2}_{t} \circ V^{i_3^r(i_0,i_2)} + V^{i_1^r(i_0,i_2)} \circ \dot{\Pi}^{i_2}_{t} \circ (V+\hat{V})^{i_3^r(i_0,i_2)} \,. \tag{3.47}$$

The frequency dependency, as well as which classes contribute in each case are determined above. We note that the form the equation for $\dot{V}_p$ looks is thanks to the assumption of cross symmetry. If we do not make this assumption $\hat{V}$ enters the equation in an analogous manner and each term is then multiplied by a factor of one half. The two last equations are the ones that are actually being calculated in the code. The non-differentiated versions of these see only the removal of the dot on top of Π_r.

		$\sigma\sigma\|\sigma\sigma$			$\sigma\bar{\sigma}\|\sigma\bar{\sigma}$			$\sigma\bar{\sigma}\|\bar{\sigma}\sigma$		
$\mathcal{K}_1$		$(V+\hat{V})^a_1$	$(V+\hat{V})^p_1$	$(V+\hat{V})^t_1$	V^a_1	V^p_1	V^t_1	$\hat{V}^a_1$	$\hat{V}^p_1$	$\hat{V}^t_1$
1111	0	0	0	0	0	0	0	0	0	0
1112	1	B^a_1	B^p_1	B^t_1	$\bar{B}^a_1$	$\bar{B}^p_1$	$\bar{B}^t_1$	$T_S T_2 \bar{B}^t_1$	$T_1 \bar{B}^p_1$	$T_S T_2 \bar{B}^a_1$
1121	2	$T_3 B^a_1$	B^p_1	$T_3 B^t_1$	$T_S T_3 \bar{B}^a_1$	$\bar{B}^p_1$	$T_S T_3 \bar{B}^t_1$	$T_1 \bar{B}^t_1$	$T_1 \bar{B}^p_1$	$T_1 \bar{B}^a_1$
1122	3	C^a_1	0	C^t_1	$\bar{C}^a_1$	0	$\bar{C}^t_1$	$T_1 \bar{C}^t_1$	0	$T_1 \bar{C}^a_1$
1211	4	$T_3 B^a_1$	$T_C B^p_1$	B^t_1	$T_S T_3 \bar{B}^a_1$	$T_C \bar{B}^p_1$	$\bar{B}^t_1$	$T_1 \bar{B}^t_1$	$T_1 T_C \bar{B}^p_1$	$T_S T_2 \bar{B}^a_1$
1212	5	C^a_1	D^p_1	0	$\bar{C}^a_1$	$\bar{D}^p_1$	0	$T_1 \bar{C}^t_1$	$T_1 \bar{D}^p_1$	0
1221	6	0	D^p_1	C^t_1	0	$\bar{D}^p_1$	$\bar{C}^t_1$	0	$T_1 \bar{D}^p_1$	$T_1 \bar{C}^a_1$
1222	7	B^a_1	$T_C B^p_1$	$T_3 B^t_1$	$\bar{B}^a_1$	$T_C \bar{B}^p_1$	$T_S T_3 \bar{B}^t_1$	$T_S T_2 \bar{B}^t_1$	$T_1 T_C \bar{B}^p_1$	$T_1 \bar{B}^a_1$
2111	8	B^a_1	$T_C B^p_1$	$T_3 B^t_1$	$\bar{B}^a_1$	$T_C \bar{B}^p_1$	$T_S T_3 \bar{B}^t_1$	$T_S T_2 \bar{B}^t_1$	$T_1 T_C \bar{B}^p_1$	$T_1 \bar{B}^a_1$
2112	9	0	D^p_1	C^t_1	0	$\bar{D}^p_1$	$\bar{C}^t_1$	0	$T_1 \bar{D}^p_1$	$T_1 \bar{C}^a_1$
2121	10	C^a_1	D^p_1	0	$\bar{C}^a_1$	$\bar{D}^p_1$	0	$T_1 \bar{C}^t_1$	$T_1 \bar{D}^p_1$	0
2122	11	$T_3 B^a_1$	$T_C B^p_1$	B^t_1	$T_S T_3 \bar{B}^a_1$	$T_C \bar{B}^p_1$	$\bar{B}^t_1$	$T_1 \bar{B}^t_1$	$T_1 T_C \bar{B}^p_1$	$T_S T_2 \bar{B}^a_1$
2211	12	C^a_1	0	C^t_1	$\bar{C}^a_1$	0	$\bar{C}^t_1$	$T_1 \bar{C}^t_1$	0	$T_1 \bar{C}^a_1$
2212	13	$T_3 B^a_1$	B^p_1	$T_3 B^t_1$	$T_S T_3 \bar{B}^a_1$	$\bar{B}^p_1$	$T_S T_3 \bar{B}^t_1$	$T_1 \bar{B}^t_1$	$T_1 \bar{B}^p_1$	$T_1 \bar{B}^a_1$
2221	14	B^a_1	B^p_1	B^t_1	$\bar{B}^a_1$	$\bar{B}^p_1$	$\bar{B}^t_1$	$T_S T_2 \bar{B}^t_1$	$T_1 \bar{B}^p_1$	$T_S T_2 \bar{B}^a_1$
2222	15	0	0	0	0	0	0	0	0	0

Table 3.1: Keldysh structure of the $\mathcal{K}_1$ class.

		$\sigma\sigma\|\sigma\sigma$					
$(V+\hat{V})_{2^{(\prime)}}$		$(V+\hat{V})^a_2$	$(V+\hat{V})^a_{2'}$	$(V+\hat{V})^p_2$	$(V+\hat{V})^p_{2'}$	$(V+\hat{V})^t_2$	$(V+\hat{V})^t_{2'}$
1111	0	A^a_2	$T_3A^a_2$	A^p_2	$T_CA^p_2$	$T_2A^a_2$	$T_1A^a_2$
1112	1	B^a_2	$T_3C^a_2$	B^p_2	$T_CC^p_2$	$T_2B^a_2$	$T_1C^a_2$
1121	2	C^a_2	$T_3B^a_2$	B^p_2	$T_CT_3C^p_2$	$T_2C^a_2$	$T_1B^a_2$
1122	3	D^a_2	$T_3D^a_2$	A^p_2	0	$T_2D^a_2$	$T_1D^a_2$
1211	4	C^a_2	$T_CB^a_2$	C^p_2	$T_CB^p_2$	$T_CT_2B^a_2$	$T_1C^a_2$
1212	5	D^a_2	$T_CD^a_2$	D^p_2	$T_CD^p_2$	0	$T_1A^a_2$
1221	6	A^a_2	0	D^p_2	$T_CT_3D^p_2$	$T_CT_2D^a_2$	$T_1D^a_2$
1222	7	B^a_2	$T_3F^a_2$	C^p_2	$T_CF^p_2$	$T_2F^a_2$	$T_1B^a_2$
2111	8	$T_CT_3B^a_2$	$T_3C^a_2$	$T_3C^p_2$	$T_CB^p_2$	$T_2C^a_2$	$T_CT_1B^a_2$
2112	9	0	$T_3A^a_2$	$T_3D^p_2$	$T_CD^p_2$	$T_2D^a_2$	$T_CT_1D^a_2$
2121	10	$T_CT_3D^a_2$	$T_3D^a_2$	$T_3D^p_2$	$T_CT_3D^p_2$	$T_2A^a_2$	0
2122	11	F^a_2	$T_3B^a_2$	$T_3C^p_2$	$T_CF^p_2$	$T_2B^a_2$	$T_1F^a_2$
2211	12	$T_CT_3D^a_2$	$T_CD^a_2$	0	$T_CA^p_2$	$T_CT_2D^a_2$	$T_CT_1D^a_2$
2212	13	F^a_2	$T_CB^a_2$	F^p_2	$T_CC^p_2$	$T_2F^a_2$	$T_CT_1B^a_2$
2221	14	$T_CT_3B^a_2$	$T_3F^a_2$	F^p_2	$T_CT_3C^p_2$	$T_CT_2B^a_2$	$T_1F^a_2$
2222	15	0	0	0	0	0	0

Table 3.2: Keldysh structure of the all-spins-equal component of the $\mathcal{K}_{2^{(\prime)}}$ classes.

$V_{2^{(\prime)}}$		$\sigma\bar{\sigma}\vert\sigma\bar{\sigma}$					
		V_2^a	$V_{2'}^a$	V_2^p	$V_{2'}^p$	V_2^t	$V_{2'}^t$
1111	0	$\bar{A}_2^a$	$T_S T_3 \bar{A}_2^a$	$\bar{A}_2^p$	$T_C \bar{A}_2^p$	$\bar{A}_2^t$	$T_S T_3 \bar{A}_2^t$
1112	1	$\bar{B}_2^a$	$T_S T_3 \bar{C}_2^a$	$\bar{B}_2^p$	$T_C \bar{C}_2^p$	$\bar{B}_2^t$	$T_S T_3 \bar{C}_2^t$
1121	2	$\bar{C}_2^a$	$T_S T_3 \bar{B}_2^a$	$\bar{B}_2^p$	$T_S T_C T_3 \bar{C}_2^p$	$\bar{C}_2^t$	$T_S T_3 \bar{B}_2^t$
1122	3	$\bar{D}_2^a$	$T_S T_3 \bar{D}_2^a$	$\bar{A}_2^p$	0	$\bar{D}_2^t$	$T_S T_3 \bar{D}_2^t$
1211	4	$\bar{C}_2^a$	$T_C \bar{B}_2^a$	$\bar{C}_2^p$	$T_C \bar{B}_2^p$	$T_C \bar{B}_2^t$	$T_S T_3 \bar{C}_2^t$
1212	5	$\bar{D}_2^a$	$T_C \bar{D}_2^a$	$\bar{D}_2^p$	$T_C \bar{D}_2^p$	0	$T_S T_3 \bar{A}_2^t$
1221	6	$\bar{A}_2^a$	0	$\bar{D}_2^p$	$T_S T_C T_3 \bar{D}_2^p$	$T_C \bar{D}_2^t$	$T_S T_3 \bar{D}_2^t$
1222	7	$\bar{B}_2^a$	$T_S T_3 \bar{F}_2^a$	$\bar{C}_2^p$	$T_C \bar{F}_2^p$	$\bar{F}_2^t$	$T_S T_3 \bar{B}_2^t$
2111	8	$T_S T_C T_3 \bar{B}_2^a$	$T_S T_3 \bar{C}_2^a$	$T_S T_3 \bar{C}_2^p$	$T_C \bar{B}_2^p$	$\bar{C}_2^t$	$T_S T_C T_3 \bar{B}_2^t$
2112	9	0	$T_S T_3 \bar{A}_2^a$	$T_S T_3 \bar{D}_2^p$	$T_C \bar{D}_2^p$	$\bar{D}_2^t$	$T_S T_C T_3 \bar{D}_2^t$
2121	10	$T_S T_C T_3 \bar{D}_2^a$	$T_S T_3 \bar{D}_2^a$	$T_S T_3 \bar{D}_2^p$	$T_S T_C T_3 \bar{D}_2^p$	$\bar{A}_2^t$	0
2122	11	$\bar{F}_2^a$	$T_S T_3 \bar{B}_2^a$	$T_S T_3 \bar{C}_2^p$	$T_C \bar{F}_2^p$	$\bar{B}_2^t$	$T_S T_3 \bar{F}_2^t$
2211	12	$T_S T_C T_3 \bar{D}_2^a$	$T_C \bar{D}_2^a$	0	$T_C \bar{A}_2^p$	$T_C \bar{D}_2^t$	$T_S T_C T_3 \bar{D}_2^t$
2212	13	$\bar{F}_2^a$	$T_C \bar{B}_2^a$	$\bar{F}_2^p$	$T_C \bar{C}_2^p$	$\bar{F}_2^t$	$T_S T_C T_3 \bar{B}_2^t$
2221	14	$T_S T_C T_3 \bar{B}_2^a$	$T_S T_3 \bar{F}_2^a$	$\bar{F}_2^p$	$T_S T_C T_3 \bar{C}_2^p$	$T_C \bar{B}_2^t$	$T_S T_3 \bar{F}_2^t$
2222	15	0	0	0	0	0	0

Table 3.3: Keldysh structure of the V spin component of the $\mathcal{K}_{2'}$ classes.

$\hat{V}_{2^{(\prime)}}$		$\sigma\bar{\sigma}\vert\bar{\sigma}\sigma$					
		$\hat{V}_2^a$	$\hat{V}_{2'}^a$	$\hat{V}_2^p$	$\hat{V}_{2'}^p$	$\hat{V}_2^t$	$\hat{V}_{2'}^t$
1111	0	$T_S T_2 \bar{A}_2^t$	$T_1 \bar{A}_2^t$	$T_1 \bar{A}_2^p$	$T_S T_C T_1 \bar{A}_2^p$	$T_S T_2 \bar{A}_2^a$	$T_1 \bar{A}_2^a$
1112	1	$T_S T_2 \bar{B}_2^t$	$T_1 \bar{C}_2^t$	$T_1 \bar{B}_2^p$	$T_S T_C T_1 \bar{C}_2^p$	$T_S T_2 \bar{B}_2^a$	$T_1 \bar{C}_2^a$
1121	2	$T_S T_2 \bar{C}_2^t$	$T_1 \bar{B}_2^t$	$T_1 \bar{B}_2^p$	$T_1 T_C \bar{C}_2^p$	$T_S T_2 \bar{C}_2^a$	$T_1 \bar{B}_2^a$
1122	3	$T_S T_2 \bar{D}_2^t$	$T_1 \bar{D}_2^t$	$T_1 \bar{A}_2^p$	0	$T_S T_2 \bar{D}_2^a$	$T_1 \bar{D}_2^a$
1211	4	$T_S T_2 \bar{C}_2^t$	$T_1 T_C \bar{B}_2^t$	$T_1 \bar{C}_2^p$	$T_1 T_C \bar{B}_2^p$	$T_1 T_C \bar{B}_2^a$	$T_1 \bar{C}_2^a$
1212	5	$T_S T_2 \bar{D}_2^t$	$T_1 T_C \bar{D}_2^t$	$T_1 \bar{D}_2^p$	$T_S T_C T_1 \bar{D}_2^p$	0	$T_1 \bar{A}_2^a$
1221	6	$T_S T_2 \bar{A}_2^t$	0	$T_1 \bar{D}_2^p$	$T_1 T_C \bar{D}_2^p$	$T_1 T_C \bar{D}_2^a$	$T_1 \bar{D}_2^a$
1222	7	$T_S T_2 \bar{B}_2^t$	$T_1 \bar{F}_2^t$	$T_1 \bar{C}_2^p$	$T_S T_C T_1 \bar{F}_2^p$	$T_S T_2 \bar{F}_2^a$	$T_1 \bar{B}_2^a$
2111	8	$T_S T_C T_1 \bar{B}_2^t$	$T_1 \bar{C}_2^t$	$T_S T_2 \bar{C}_2^p$	$T_1 T_C \bar{B}_2^p$	$T_S T_2 \bar{C}_2^a$	$T_S T_C T_1 \bar{B}_2^a$
2112	9	0	$T_1 \bar{A}_2^t$	$T_S T_2 \bar{D}_2^p$	$T_S T_C T_1 \bar{D}_2^p$	$T_S T_2 \bar{D}_2^a$	$T_S T_C T_1 \bar{D}_2^a$
2121	10	$T_S T_C T_1 \bar{D}_2^t$	$T_1 \bar{D}_2^t$	$T_S T_2 \bar{D}_2^p$	$T_1 T_C \bar{D}_2^p$	$T_S T_2 \bar{A}_2^a$	0
2122	11	$T_S T_2 \bar{F}_2^t$	$T_1 \bar{B}_2^t$	$T_S T_2 \bar{C}_2^p$	$T_S T_C T_1 \bar{F}_2^p$	$T_S T_2 \bar{B}_2^a$	$T_1 \bar{F}_2^a$
2211	12	$T_S T_C T_1 \bar{D}_2^t$	$T_1 T_C \bar{D}_2^t$	0	$T_S T_C T_1 \bar{A}_2^p$	$T_1 T_C \bar{D}_2^a$	$T_S T_C T_1 \bar{D}_2^a$
2212	13	$T_S T_2 \bar{F}_2^t$	$T_1 T_C \bar{B}_2^t$	$T_1 \bar{F}_2^p$	$T_S T_C T_1 \bar{C}_2^p$	$T_S T_2 \bar{F}_2^a$	$T_S T_C T_1 \bar{B}_2^a$
2221	14	$T_S T_C T_1 \bar{B}_2^t$	$T_1 \bar{F}_2^t$	$T_1 \bar{F}_2^p$	$T_1 T_C \bar{C}_2^p$	$T_1 T_C \bar{B}_2^a$	$T_1 \bar{F}_2^a$
2222	15	0	0	0	0	0	0

Table 3.4: Keldysh structure of the $\hat{V}$ spin component of the $\mathcal{K}_{2^{(\prime)}}$ classes.

		$\sigma\sigma\|\sigma\sigma$			$\sigma\bar{\sigma}\|\sigma\bar{\sigma}$			$\sigma\bar{\sigma}\|\bar{\sigma}\sigma$		
$\mathcal{K}_3$		$(V+\hat{V})_3^a$	$(V+\hat{V})_3^p$	$(V+\hat{V})_3^t$	V_3^a	V_3^p	V_3^t	$\hat{V}_3^a$	$\hat{V}_3^p$	$\hat{V}_3^p$
1111	0	A_3^a	A_3^p	$T_2A_3^a$	$\bar{A}_3^a$	$\bar{A}_3^p$	$\bar{A}_3^t$	$T_1\bar{A}_3^t$	$T_1\bar{A}_3^p$	$T_1\bar{A}_3^a$
1112	1	B_3^a	B_3^p	$T_2B_3^a$	$\bar{B}_3^a$	$\bar{B}_3^p$	$\bar{B}_3^t$	$T_ST_2\bar{B}_3^t$	$T_ST_2\bar{B}_3^p$	$T_ST_2\bar{B}_3^a$
1121	2	$T_3B_3^a$	$T_3B_3^p$	$T_1B_3^a$	$T_ST_3\bar{B}_3^a$	$T_ST_3\bar{B}_3^p$	$T_ST_3\bar{B}_3^t$	$T_1\bar{B}_3^t$	$T_1\bar{B}_3^p$	$T_1\bar{B}_3^a$
1122	3	C_3^a	C_3^p	$T_2C_3^a$	$\bar{C}_3^a$	$\bar{C}_3^p$	$\bar{C}_3^t$	$T_1\bar{C}_3^t$	$T_1\bar{C}_3^p$	$T_1\bar{C}_3^a$
1211	4	$T_CB_3^a$	$T_CB_3^p$	$T_1T_CB_3^a$	$T_C\bar{B}_3^a$	$T_C\bar{B}_3^p$	$T_C\bar{B}_3^t$	$T_1T_C\bar{B}_3^t$	$T_1T_C\bar{B}_3^p$	$T_1T_C\bar{B}_3^a$
1212	5	D_3^a	D_3^p	D_3^t	$\bar{D}_3^a$	$\bar{D}_3^p$	$\bar{D}_3^t$	$T_1\bar{E}_3^t$	$T_1\bar{E}_3^p$	$T_1\bar{E}_3^a$
1221	6	$T_1D_3^t$	$T_1D_3^p$	$T_1D_3^a$	$\bar{E}_3^a$	$\bar{E}_3^p$	$\bar{E}_3^t$	$T_1\bar{D}_3^t$	$T_1\bar{D}_3^p$	$T_1\bar{D}_3^a$
1222	7	F_3^a	F_3^p	$T_1F_3^a$	$\bar{F}_3^a$	$\bar{F}_3^p$	$\bar{F}_3^t$	$T_1\bar{F}_3^t$	$T_1\bar{F}_3^p$	$T_1\bar{F}_3^a$
2111	8	$T_CT_3B_3^a$	$T_CT_3B_3^p$	$T_CT_1B_3^a$	$T_ST_CT_3\bar{B}_3^a$	$T_ST_CT_3\bar{B}_3^p$	$T_ST_CT_3\bar{B}_3^t$	$T_ST_CT_2\bar{B}_3^t$	$T_ST_CT_2\bar{B}_3^p$	$T_ST_CT_2\bar{B}_3^a$
2112	9	$T_2D_3^t$	$T_2D_3^p$	$T_2D_3^a$	$T_ST_3\bar{E}_3^a$	$T_ST_3\bar{E}_3^p$	$T_ST_3\bar{E}_3^t$	$T_ST_2\bar{D}_3^t$	$T_ST_2\bar{D}_3^p$	$T_ST_2\bar{D}_3^a$
2121	10	$T_3D_3^a$	$T_3D_3^p$	$T_3D_3^t$	$T_ST_3\bar{D}_3^a$	$T_ST_3\bar{D}_3^p$	$T_ST_3\bar{D}_3^t$	$T_ST_2\bar{E}_3^t$	$T_ST_2\bar{E}_3^p$	$T_ST_2\bar{E}_3^a$
2122	11	$T_3F_3^a$	$T_3F_3^p$	$T_2F_3^a$	$T_ST_3\bar{F}_3^a$	$T_ST_3\bar{F}_3^p$	$T_ST_3\bar{F}_3^t$	$T_ST_2\bar{F}_3^t$	$T_ST_2\bar{F}_3^p$	$T_ST_2\bar{F}_3^a$
2211	12	$T_CC_3^a$	$T_CC_3^p$	$T_1T_CC_3^a$	$T_C\bar{C}_3^a$	$T_C\bar{C}_3^p$	$T_C\bar{C}_3^t$	$T_1T_C\bar{C}_3^t$	$T_1T_C\bar{C}_3^p$	$T_1T_C\bar{C}_3^a$
2212	13	$T_CF_3^a$	$T_CF_3^p$	$T_2T_CF_3^a$	$T_C\bar{F}_3^a$	$T_C\bar{F}_3^p$	$T_C\bar{F}_3^t$	$T_ST_CT_2\bar{F}_3^t$	$T_ST_CT_2\bar{F}_3^p$	$T_ST_CT_2\bar{F}_3^a$
2221	14	$T_CT_3F_3^a$	$T_CT_3F_3^p$	$T_CT_2F_3^a$	$T_ST_CT_3\bar{F}_3^a$	$T_ST_CT_3\bar{F}_3^p$	$T_ST_CT_3\bar{F}_3^t$	$T_1T_C\bar{F}_3^t$	$T_1T_C\bar{F}_3^p$	$T_1T_C\bar{F}_3^a$
2222	15	0	0	0	0	0	0	0	0	0

Table 3.5: Keldysh structure of the $\mathcal{K}_3$ class.

3.4 Numerical gain

The numerical complexity of the vertex is very high, as was stated at the beginning of the chapter. This is partly due to the fact that it scales multiplicatively with the number of frequency grid points one chooses for every frequency type, be it bosonic or fermionic, but factors as spin components and Keldysh structure also play an important role. Suppose we sample the bosonic frequencies ω_r from a frequency grid with N_{bos} points, the fermionic ones ν_r and ν'_r from one with N_{fer} points and have number of integration points capped by N_{int}, then the naive complexity of the full vertex scales as $\mathcal{O}\left(15 \cdot 3 \cdot N_{\text{bos}} \cdot N_{\text{fer}}^2 \cdot N_{\text{int}}\right)$ since the value of the vertex function, with 15 Keldysh and 3 spin components, must be determined for every point in the three-dimensional frequency box and one integration must be performed at every one of these points.

Reducing the number of spin components from three to two then means a mean speed-up of 2/3; reducing the number of Keldysh components form 15 to the maximally 6 of the $\mathcal{K}_3$ class means an additional speed-up of 2/5, so an overall factor of 4/15 is yielded by these two reductions.

Limiting the amount of frequencies an object depends on yields then a much lower complexity, with the $\mathcal{K}_{2^{(\prime)}}$ classes scaling like $\mathcal{O}\left(N_{\text{bos}} \cdot N_{\text{fer}}\right)$ and the $\mathcal{K}_1$ class only like $\mathcal{O}\left(N_{\text{bos}}\right)$. Thus, a natural hierarchy of numerical complexity is established, with computation times comparing as

$$\frac{\tau_{\mathcal{K}_1}}{\tau_{\mathcal{K}_3}} \sim \frac{1}{\mathcal{O}\left(N_{\text{fer}}^2\right)} \tag{3.48}$$

$$\frac{\tau_{\mathcal{K}_2}}{\tau_{\mathcal{K}_3}} \sim \frac{1}{\mathcal{O}\left(N_{\text{fer}}\right)}, \tag{3.49}$$

meaning that the calculations of the $\mathcal{K}_1$ class are *much* faster than those for the $\mathcal{K}_2$ class. Now, since the $\mathcal{K}_3 \sim \mathcal{O}\left(U^4\right)$ and $\mathcal{K}_{2^{(\prime)}} \sim \mathcal{O}\left(U^3\right)$, if U is sufficiently small, one can neglect the contributions of one or both of these classes, yielding a speedup in the calculation of several orders of magnitudes (as measured in seconds). This is a not a very general simplification, since we do not necessarily want to limit ourselves to the $U \ll 1$ case. Nonetheless, this decomposition is also useful for its physical interpretation.

The realizations above then give us a clue on how to speed-up the calculations of the $\mathcal{K}_{2'}$ and the $\mathcal{K}_3$ classes: have class-dependent frequency grids with different number of points, i.e. $N_{\text{fer}}^{(2)} \sim N_{\text{bos}}^{(2)} \ll N_{\text{bos}}^{(1)} := N_{\text{bos}}$. This trick does not change the scaling of the complexity of $\mathcal{K}_{2^{(\prime)}}$ or $\mathcal{K}_3$, but does reduce the required computational time greatly. The challenge then shifts to laying these fewer frequencies in such a way, that the main features of the respective classes are nonetheless captured.

In contrast to the vertex, the self-energy has a complexity $\mathcal{O}\left(2 \cdot N_{\text{fer}}\right)$, so it is similar to a $\mathcal{K}_1$ object, since $N_{\text{bos}} \sim N_{\text{fer}}$. This means that there is no need to parametrize it in an efficient way and our particular focus with the vertex is justified. This remark concludes our discussion of the parametrization of the vertex. In the next chapter, we turn our attention to how one may approach the implementation of a code to make these calculations.

Chapter 4

Implementation

In this Chapter we will discuss a C++ code capable of numerically determining both the self-energy and the vertex with full frequency dependence for the single-impurity model, the challenges it poses, data flows that allow for a more efficient calculation and considerations relevant for generalizing it to more general, higher dimensional models. We assume some familiarity with C++ or, at least, an object-oriented programming language as well as with the parallelization tools OpenMP as well as MPI, though most of the Chapter can be understood on the basis of the physical equations being programmed.

4.1 Structure

To explain the structure of the code, we opt for a bottom-up approach, i.e. we begin with the simplest classes and structures in the code and work our way up to the most complex ones, trying to give the clearest overview possible of the dependencies of these objects on one another. We also give a step-by-step guide for the implementation and a visualization of the code structure in App. B. Though the central aspect of this work revolves around mfRG flows, we give the overview of the code structure for both flowing and non-flowing calculations, since the latter have some important caveats and are fundamental in the development of such a code, both for benchmarking and result-producing purposes. For this discussion we will differentiate between physical concepts and computational instances by writing the latter in typewriter font. Hence a `self-energy` models the physical self-energy Σ.

4.1.1 Global parameters

Any calculation must start with the definition of the global parameters describing both the physical system and the numerical aspects of the simulation. The global parameters hence fall into five main categories: physical parameters, frequency grid parameters, flow grid parameters, Keldysh and spin structure parameters and technical parameters.

Physical parameters These make reference to the values which enter the single-impurity Anderson model, i.e. in our case, the numerical value of the level broadening Γ, the interaction strength U, the temperature of the system T, the chemical potential μ (which we always set to zero), the onsite energy of the local level ϵ and the bias voltage V across the impurity. The equilibrium case corresponds with $V = 0$. Calculations outside of equilibrium mean a voltage offset is present. We choose this offset to be symmetrically split between both leads, i.e. we adjust the chemical potentials of the leads to $\pm V/2$.

For our units we make the conventional choices $k_{\mathrm{B}} = e = \hbar = 1$. Further, to set an energy scale, we choose $U = 1$. The reason behind this is that, with this choice, a hybridization flow in $U/(\Gamma + \Lambda) = U/\Gamma_{\mathrm{eff}}$ yields results, in *one* run, for all interaction strengths between $U/([\Gamma_{\mathrm{eff}}]_{\mathrm{ini}}) \approx 0$ and $U/\Gamma = \Gamma^{-1}$. This implies a massive reduction in computation times, but it relies heavily on the fact that every point in a fRG-hybridization flow corresponds to a physical system at the respective interaction strength. We actually go one step further and exploit the way Yamada writes the propagators [16] (recall Eq. 2.50), and implement the flow $\Lambda \to 0$ actually as $\Delta \to \Gamma$, and think of the effective interaction strength as U/Δ. This is advantageous for comparing our results with ones produced with methods like NRG, where the energy units are set through the bandwidth Δ. Hence, and thanks to our conventions regarding the definition of Γ [7], $\Delta_{\mathrm{NRG}} = 1/2$ and, hence, a simple conversion rule can be derived

$$\begin{aligned} \frac{U_{\mathrm{NRG}}}{\Delta_{\mathrm{NRG}}} &= \frac{U_{\mathrm{fRG}}}{\Delta_{\mathrm{fRG}}} \\ \frac{U_{\mathrm{NRG}}}{1/2} &= \frac{1}{\Delta_{\mathrm{fRG}}} \\ \Rightarrow U_{\mathrm{NRG}} &= \frac{1}{2\Delta_{\mathrm{fRG}}} \end{aligned} \tag{4.1}$$

where we have $U_{\mathrm{fRG}} = 1$ by our convention, $\Delta_{\mathrm{NRG}} = 1/2$ and $\Delta_{\mathrm{fRG}} = \frac{\Gamma+\Lambda}{2}$, as defined in Chap. 2. Equation (4.1) implies that for every U_{NRG}, there exists a corresponding Λ along the fRG-flow so that the physical system described by both methods is the same. Due to the huge gain that it implies being able to probe interaction strengths from zero up to U/Γ in one run, we adopt this convention at the expense of having a separate one from the conventional one used for NRG. Notice that similar unit-conversion calculations must be made for every relevant energy scale in the system (T/U or V/U in our case).

Frequency grid parameters The end points Ω^- and Ω^+ of the sampling intervals $[-\Omega^-, \Omega^+]$, and the number of points to have per grid and per kind of grid: $N^{(1)}_{\mathrm{bos}}$, $N^{(2)}_{\mathrm{bos}}$, $N^{(3)}_{\mathrm{bos}}$ for the bosonic grids and similarly $N^{(1)}_{\mathrm{fer}}$, $N^{(2)}_{\mathrm{fer}}$, $N^{(3)}_{\mathrm{fer}}$ for the fermionic ones. For simplicity, we usually choose $\Omega^- = \Omega^+$ in order to have symmetric frequency grids and $N^{(i)}_{\mathrm{bos}} = N^{(i)}_{\mathrm{fer}}$, as to have equal bosonic and fermionic frequency grids, though the possibility for different values here is supported. Our implementation requires $\Omega^{\pm} > 0$, since we want to always include a neighborhood of points around zero.

A naive approach to sampling the points in the interval $[-\Omega^-, \Omega^+]$ would be a linear distribution of the points between the limits. However, experience showed this to be extremely inefficient since the features of both the self-energy and the vertex are centered around $\nu = 0$ and $\omega = 0$. Hence, a higher density of sample point is needed around the origin and fewer must be taken the further ν or ω is from zero.

To this end we rely on a similar trick to the one used to map an open interval to $\mathbb{R}$. Our proceeding is taking a function f, defined as

$$f(\omega) = \frac{\Omega_{\text{scale}}\omega|\omega|}{\sqrt{1-\omega^2}} \tag{4.2}$$

to map only the limits $\pm\Omega^\pm$ with the inverse function of f to $X^\pm := f^{-1}(\pm\Omega^\pm) \in (-1, 1)$, then choosing $N^{(i)}_{\text{bos/fer}}$ points evenly distributed between these two and then mapping them under f^{-1} back to the original interval. Notice this strategy guarantees that, if $\Omega^+ = \Omega^-$ and the number of sampling points is odd, 0 will be contained in the final grid.

The form of f ensures that the density of points around 0 and until $|\omega| \lesssim \Omega_{\text{scale}}$ increases quadratically as $|\omega| \to 0$. Note that Ω_{scale} must be carefully selected, for a too high density of points around zero implies a too narrow resolution for the tails at large absolute values of the frequencies.

Flow grid parameters Apart from the frequency grid, we also have a fixed Λ-grid for the integration of the ODE. This integration is done with a regular 4^{th}-order Runge–Kutta algorithm. However, to cover many orders of magnitude in energy, start at a high-enough energy scale and be able to resolve with the required precision at the end of the flow, we implement a logarithmic grid for this purpose.

The mapping strategy is similar as that of the frequency grids, namely define Λ_{ini} and Λ_{fin}, map these to the open interval $[0, 1)$ with the inverse of a carefully chosen function g, lay a linear grid of nODE points between these two and then map all of these back to the original interval with g. For our work, we always have $\Lambda_{\text{fin}} = 0$, since that scale represents the full solution of the model at interaction strength U/Γ (since the units are set by $U = 1$, the only other energy remaining at $\Lambda = 0$ is Γ).

The function we use for this mapping is

$$g(\Lambda) = \log_{10}\left(1 + \frac{\Lambda}{\Lambda_{\text{scale}}}\right), \tag{4.3}$$

where Λ_{scale} must also be picked to carefully as to yield many-but-no-more-than-needed points in the vicinity of $\Lambda \to 0$, where the calculations take the longest.

Keldysh and spin parameters This set of parameters fixes the number of Keldysh components for the computation and includes the lists of the corresponding indices that are independent, based on the tables presented last chapter. Also, here are included the fixed combinations of indices that yield an odd sum of Keldysh indices for the efficient handling

of the bare vertex. The indices for non-zero entries of the bubbles are also included here (named BK in Chap. 2). Since the aim of the code is to be generalizable to more complex and, maybe, not SU(2)-spin-symmetric systems, we also include a spin index, which is the number of required pair of spin components needed. For the SIAM, this is set to 1 since we have V and $\hat{V}$. This structure allows us to implement the T_i transformations of Chapter 3 more efficiently than if we did not store the spin components in pairs.

Technical parameters The technical parameters concern technical details of the computation. Most of them are preprocessor macros that allow for some simplified run, or for the turning on and off of diagrammatic classes and setting the number of loops. These ones also include tolerance of the integrator, a component of the code which will be discussed later, and the one for the interpolating functions, since experience showed that this could be a bug-prone component of the code when running it on different architectures.

The other technical parameters of importance are the ones defining the flow, i.e. the regulator to be used. Until now, the only one that has been implemented is the hybridization flow, i.e. $\frac{\Gamma}{2} \to \frac{\Gamma+\Lambda}{2}$ in the denominator of G^Λ, which was discussed in Chapter 2[1]. Since the mfRG should be regulator independent, implementation of various regulator possibilities to test this hypothesis is still needed, yet it is already supported.

4.1.2 The `self-energy` class and the `loop` function

The `self-energy` class is defined by one vector of length $2 \cdot N_{\text{fer}}^{(1)}$, which is a placeholder for the retarded self-energy in the first half and the Keldysh component in the second half, and a complex value, which is the Hartree shift of Σ^R, noted Σ^H, and is independent of ν and Λ.

Calculating Σ^H is not as straightforward as a naive calculation would suggest and for the details thereof we refer the reader to either [6] or [7]. Taking causality into account, the result is then proportional to the integral over the *lesser* Green's function $G^<$, which can be analytically carried out in the particle-hole-symmetric case. Then, $\Sigma^H = U/2$. Note that there is no Hartree contribution to Σ^K.

Every `self-energy` has a value setting and two value reading functions, one discrete and one continuous. The continuous, value-reading one receives a real frequency ν as input and, depending on whether $\nu \in [-\Omega^-, \Omega^+]$ or not, it interpolates linearly between the saved values, returned by the discrete value-reading function, or it returns Σ^H in the retarded case or 0 for the Keldysh component. The value setting function stores the results of the `loop` function in the right component of the vector of the `self-energy`.

The `loop` function calculates the L function of Eq. (2.22). In order to do so, the function requires a `fullvert` (an object to be described later), a `propagator` (discussed next) and a boolean, specifying which spin components appear in the calculation. Due to the vertex's internal symmetries and the mappings these do to the frequencies, the limits of

[1] Notice that this replacement looks trivial if one writes it in terms of Δ, namely $\Delta \to \Delta^\Lambda$.

the integral of the implementation of the `loop` function depend on the frequency at which the result is being calculated, and looks as follows

$$\Sigma(\nu) = \mathtt{L}(\Gamma, G) = -\frac{1}{2\pi \mathrm{i}} \int_{-\Omega^- - |\nu|}^{\Omega^+ + |\nu|} \mathrm{d}\nu' \Gamma(\nu, \nu', \nu) \circ G(\nu') \,, \tag{4.4}$$

where we have omitted the Keldysh indices for simplicity. These turn out to be good-enough numerical approximations of the analytic limits, which are $\pm\infty$, since in our implementation the vertex is only stored on the frequency grids and is assumed to have decayed enough to be negligible outside of these. These limits however imply that large values of ν see integration intervals $[-2\Omega^-, 2\Omega^+]$.

The last parameter which `L` receives is notably not present in Eq. (2.22) and its inclusion is based on the need of having non-flowing calculations. The spin components of the vertex that enter the calculation are different depending on the calculation: the static case only needs V, whereas both V and $\Gamma_{\sigma\sigma|\sigma\sigma} = V + \hat{V}$ enter in the flowing scenario to yield a total vertex contribution of $2V + \hat{V}$.

4.1.3 The `propagator` class

A `propagator` object is defined with a Λ scale, two `self-energies` and a char encoding the type. The two `self-energies` are required for generality, since a differentiated propagator will include dependencies on Σ^Λ as well as on $\dot{\Sigma}^\Lambda$.

The different types of propagator the class supports are: (a) the regular propagator G^Λ; (b) the single-scale propagator S^Λ; and (c) the Katanin extension $\dot{G}^\Lambda = S + G \cdot \dot{\Sigma} \cdot G$ For each one of these, the constructor of the Propagator only initializes with a non-zero value the required self-energies. For G and S the differentiated Self-energy $\dot{\Sigma}$ remains uninitialized but it is required for initialization of G.

The class also provides the objects with an evaluating function, which returns the value of the retarded or Keldysh component at a frequency ν. This function computes the values according to Eqs. (2.54) or (2.55) or the respective formulas for S or $\dot{G}$. Hence it is imperative to initialize the `propagators` with the corresponding Λ scale at which they are to be calculated. Since in the mfRG formalism we include regulators in the propagators, the implementation of the evaluation functions depends on the regulator choice.

Taking advantage of the fact that the `self-energy`'s interpolating function handles all the cases of frequencies, the interpolating function of the `propagator` then simply returns

$$\begin{aligned} G^R(\nu) &= G^R\left(\nu; \Sigma^R(\nu)\right) \qquad \text{or} \\ G^K(\nu) &= G^K\left(\nu; \Sigma^R(\nu), \Sigma^K(\nu)\right) \,. \end{aligned} \tag{4.5}$$

4.1.4 The `bubble` class and the `bubble` function

A `bubble` object is, as well as Π_r is, an aide in the calculations. It is comprised of two *references* to two `propagators` and a boolean, to handle both differentiated and regular

bubbles. In the first case, the `propagators` must be of the right type to yield either $GS + SG$ or $G\dot{G} + \dot{G}G$. The objective of storing only the references to the objects and not the objects themselves is to optimize both creation and evaluation time, as the information must not be reallocated in this case.

As the `loop` function was the code implementation of L, the same is true for the `bubble` function and B_r. As such, the `bubble` function takes two `fullverts`, two `propagators` to create the bubble, a `char` signaling the channel of the bubble and a `bool` marking whether the bubble is differentiated or not.

The bubble function then defines the prefactors that accompany each term in the bubble sum. Both the a and p channels have a prefactor of 1, whereas the t channel includes a -1, product of the exchange symmetry with the a channel. Here, we're explicitly assuming that the contributions of the p channel are cross-symmetric and hence, due to the addition over spins, we automatically include twice the usual 1/2. Should cross-symmetry not be respected, the code is made as to allow a simple change to the inclusion of the right contributions.

Afterwards comes the parallel calculation of the actual contributions to the vertices, i.e. equations with a RHS of the form

$$\dot{\gamma}_r^{i_0}\left(\omega_r, \nu_r, \nu_r'\right) = \sum_{i_2 \in BK} \int \frac{\mathrm{d}\nu_r''}{2\pi \mathrm{i}} \Gamma^{i_1^r(i_0,i_2)}\left(\omega_r, \nu_r, \nu_r''\right) \dot{\Pi}_r^{i_2}\left(\nu_1^r, \nu_2^r\right) \Gamma^{i_3^r(i_0,i_2)}\left(\omega_r, \nu_r'', \nu_r'\right) \tag{4.6}$$

or the non-flowing version without the derivatives, and i_1 and i_3 are the functions defined in Eq. (2.71).

Now we look at how the *diagrammatic* decomposition of Eq. (4.6) looks like, i.e. given that $\dot{\gamma}_r = \sum_i \mathcal{K}_i^r$, what the diagrammatic classes are that contribute to each of these derivatives. Notice that not all classes can contribute to all derivatives, since, for instance, diagrams in the $\mathcal{K}_3$ class, by definition, do not fulfill the requirement of having, say, two lines connected to the same vertex on one side. Thus, no terms with $\mathcal{K}_3$ can appear in calculations pertaining to the $\mathcal{K}_1$ class. We hence classify what classes fulfill the requirements to contribute to the flow of which others. Our results of this analysis are summarized in Table 4.1.

	L	R
SV	$\Gamma_0, \mathcal{K}_1^r, \mathcal{K}_{2'}^r$	$\Gamma_0, \mathcal{K}_1^r, \mathcal{K}_2^r$
DV	$\mathcal{K}_2^r, \mathcal{K}_3^r, \gamma_{\bar{r}}$	$\mathcal{K}_{2'}^r, \mathcal{K}_3^r, \gamma_{\bar{r}}$

Table 4.1: Categorization of diagrammatic classes.

Here, SV and DV stand for "same vertex" and "different vertices", alluding to whether or not both lines to the left (L) or the right (R) of the vertex connect to the same or to different vertices. The inclusion of $\gamma_{\bar{r}} = \sum_{r' \neq r} \gamma_{r'}$ is due to the multiloop feed-back of diagrams of channels r' to calculate higher order contributions to channel r. Through this, one then gets Table 4.2 for the contributions to $\dot{\mathcal{K}}_i^r$.

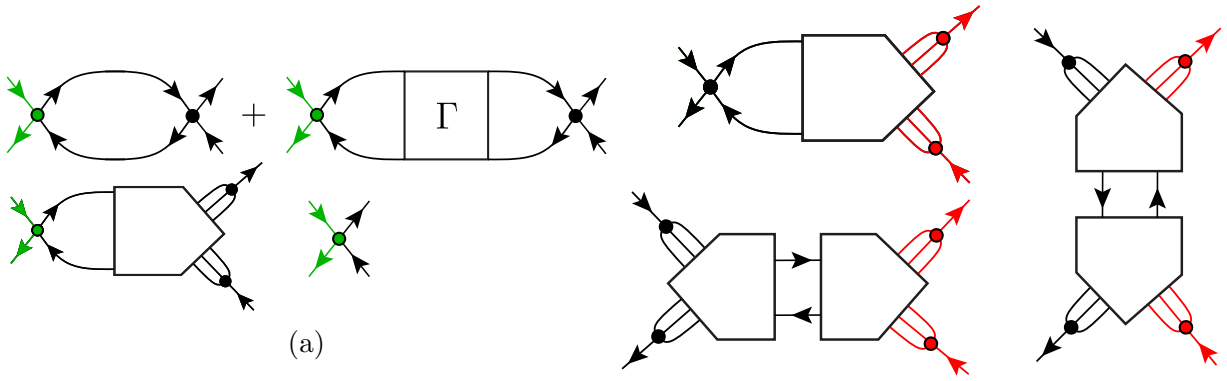

Figure 4.1: Visualization of the diagrammatic classes that enter into the flow equations of the others, both in the a channel. (a) Combinations that have two lines connected to the left bare vertex and, hence, correspond to the entry in the first column and first row of Table 4.1. (b) Diagrams that have two legs on the right side connected to different bare vertices. The $\mathcal{K}_3^t$ aids to visualize the contributions of $\gamma_{\bar{a}}$.

	L	R
$\dot{\mathcal{K}}_1^r$	$\Gamma_0, \mathcal{K}_1^r, \mathcal{K}_{2'}^r$	$\Gamma_0, \mathcal{K}_1^r, \mathcal{K}_2^r$
$\dot{\mathcal{K}}_2^r$	$\mathcal{K}_2^r, \mathcal{K}_3^r, \gamma_{\bar{r}}$	$\Gamma_0, \mathcal{K}_1^r, \mathcal{K}_2^r$
$\dot{\mathcal{K}}_{2'}^r$	$\Gamma_0, \mathcal{K}_1^r, \mathcal{K}_2^r$	$\mathcal{K}_{2'}^r, \mathcal{K}_3^r, \gamma_{\bar{r}}$
$\dot{\mathcal{K}}_3^r$	$\mathcal{K}_2^r, \mathcal{K}_3^r, \gamma_{\bar{r}}$	$\mathcal{K}_{2'}^r, \mathcal{K}_3^r, \gamma_{\bar{r}}$

Table 4.2: Contributions of diagrammatic classes to the flow equation of others.

Notice that flowing calculations do not need to ever make calculations of non-differentiated $\mathcal{K}_1$-objects, since non-differentiated objects only appear in the multiloop corrections and nested loop integrals appear exclusively in diagrams including $\mathcal{K}_{2(\prime)}, \mathcal{K}_3$ and $\gamma_{\bar{r}}$ contributions.

4.1.5 The `vertex` class and its subclasses

After having performed the calculations of the bubbles, i.e. the contributions that define the values of the independent components of the vertex, the task of storing them is in order. This takes place in the very large placeholder which is the `vertex` class. In essence, the purpose of this class is to most efficiently store and make accessible for read-out the information stored in it.

In order to do so, the `vertex` class stores a vector of `fullvert` objects, which are full vertices with two spin components, related to one another. The advantage of this structure is that it allows for a quick generalization of the code (for when, for example, SU(2)-spin symmetry is broken), where the `vertices` may have more than one pair of interdependent

spin components. Hence, in our implementation and for the SIAM, the computational object that actually has the information of the (physical) vertex is a `fullvert`, which is in turn a collection of smaller, vertex-type objects: an `irreducible` vertex, an `avert`, a `pvert` and a `tvert`.

Clearly, the `rverts` (with `r` $\in$ {`a, p, t`}) represent the γ_r, whereas the `irreducible` vertex is the fully irreducible part R. Since we are working in the parquet approximation, the `irreducible` vertex is, basically, just a 16-entry vector per spin component with values $U/2$ or $-U/2$ according to Eq. (2.65).

The `rverts` have much more structure. Aside from each one of them having a $\mathcal{K}_1$, a $\mathcal{K}_2$ and a $\mathcal{K}_3$ vector for the independent components (remember the $\mathcal{K}_{2'}$ class has no independent components of its own), each one also contains lists that codify the information reported in Tables 3.1-3.5. These objects have value-setting and both discrete and continuous value-reading functions. An important aspect of this function is that it delivers 0 if any one of the input frequencies is outside of the saved interval.

When evaluating any `rvert` at a combination of frequencies $(\omega_r, \nu_r, \nu'_r)$ (i.e. already conveniently parametrized for an `rvert`), the process is split for each one of the classes. The evaluating function of any class will first determine, for a given spin and Keldysh index input, which independent component the combination refers to and, based on which list (of the stored ones in each `rvert`) these indices are in, the transformations that must be carried out on the set $(\omega_r, \nu_r, \nu'_r)$ are performed. These transformations are the ones we explained in Chap. 3 and in App. A. Once this has happened and it has been determined whether it is necessary to complex conjugate the result or swap the channel in which it is necessary to read out, the required numerical value is calculated by an interpolating function (linear, i-dimensional for $\mathcal{K}_i$) and returned. Since these functions are called, typically, hundreds of thousands of times in a run, an efficient implementation is paramount.

Naturally, the `rvert` classes allow for a readout of the value for frequencies which are not in the r channel parametrization. This is handled so that the transformations cited between Eq. (3.2) and Eq. (3.7) are used whenever needed. This is specially useful for handling expressions like $\gamma_{r'}(\omega_r, \nu_r, \nu'_r)$ efficiently, which is of extreme importance since these kinds of terms and cross-channel contributions appear in the flow equations of the vertex.

4.1.6 The `State` class

A `State` is, as it name should suggest, a physical state of the system, which encompasses an energy scale Λ, a `self-energy` and a `vertex`. If one has a full `State` at a given Λ, this then contains the whole information of the system at that scale. States themselves do not have much functionality, as they work only as placeholders of the whole physical information, but play the role of being an information-carrier class.

4.2 Technical details

In this section we will discuss some of the most technical details of the code implementation, mostly having to do with locations in which the code can be parallelized and how it is implemented.

4.2.1 Parallelization

Parallel computing is a very useful and important tool in high-performance computing nowadays. The results presented in this thesis could not have been accomplished without parallelization. We assume the reader has some basic knowledge on parallelization schemes and tools and thus neither MPI or OpenMP need an introduction.

In the whole code, there are mainly two locations in which the code runs in parallel: the `loop` and the `bubble` functions. Both have in common that the same information must be used for several, procedurally-equal, disjoint processes i.e. none of the processes depend on any result of the others.

Given the relative simplicity of calculating the values of the `self-energy` (which scales like $\mathcal{O}(N_{\text{fer}}^{(1)})$), we only make use of OpenMP at this stage to avoid the overhead associated to the MPI information-gathering operation `MPI_Allgather`.

The part of the code doing the calculation of the bubbles is parallelized using both MPI and OpenMP. The MPI parallelization is done only over the two independent Keldysh indices of the LHS for the $\mathcal{K}_1$ class, whereas for the $\mathcal{K}_2$ and $\mathcal{K}_3$ classes it is implemented so as to run over the five or six Keldysh indices and also over the bosonic frequencies. The remaining points are taken over by OpenMP. Thus, one master index is defined and run over all possible combinations and the calculation goes over one long vector per MPI-thread, which at the end must be sorted into the right order. The master index must be converted to a combination of Keldysh and frequency indices. This is done with a generalization of counting-basis-change calculation, in which the base is different for every unit, i.e. units are counted up to a different number than the tens are and so on (somewhat similar to the imperial system of units).

This conversion is programmed in the following form, in order to avoid the computationally expensive *modulo* calculation. Let $B = \{b_1, b_2, \ldots, b_n\}$ be a set of positive integers, where each b_i is the basis of the i-th unit. Also, let $I \in \{1, 2, \ldots, b_1 \cdot b_2 \cdot \ldots \cdot b_n\}$ be a master index. Clearly, if the 1-st units (from left to right) are counted in base b_1, the 2-nd in base b_2 and so on, I takes values in all the possible combinations of numbers defined by the counting bases B. Define then a multi index $i = (i_1, i_2, \ldots, i_n)$, so that $1 \leq i_j \leq b_j$ for each $j \in \{1, \ldots, n\}$. Thus,

$$i_1 = \left\lfloor \frac{I}{b_2 \cdot \ldots \cdot b_n} \right\rfloor , \tag{4.7}$$

since an increment of one in b_1-units needs $b_2 \cdot \ldots \cdot b_n$ unitary increments. For i_2 the calculation is similar, but one needs to remove all the already achieved b_2 units, counted

by i_1. Hence, one obtains

$$i_2 = \left\lfloor \frac{I}{b_3 \cdot \ldots \cdot b_n} \right\rfloor - i_1 b_2 \,. \tag{4.8}$$

A straightforward calculation then yields the generalization

$$i_k = \left\lfloor \frac{I}{b_{k+1} \cdot \ldots \cdot b_n} \right\rfloor - \sum_{j=1}^{k-1} \left(i_j \prod_{l=j+1}^{k-1} b_l \right) \tag{4.9}$$

This implementation is needed in order to avoid the *modulo* operation and, also, have a vectorized operation, which can be parallelized.

4.2.2 HDF5 data format

In order to store the data, we use the hierarchical data format HDF5. Its benefits are speed in saving newly calculated results as well as in reading out saved data. The "multi-dimensional" system allows for several layers of data, stored hierarchically, making use of the natural structure that the `State` uses. We store the information in the form of a self-energy and a vertex, which is then further separated by channel and by diagrammatic class for every scale Λ at which one decides to export the data. This decomposition makes possible the study of pairing-channel instabilities and gives a tool, together with the physical interpretation of the diagrammatic classes, to analyze these instabilities, should they arise. The appearance of a divergence (or a numerical signal for it) in a particular channel would mark some interactions as being more important than others in the description of the physical behavior of the system. A specific class diverging would give information on the origin of the instabilities, since these posses also a physical interpretation. Therefore the access to this sorted information is of remarkable importance for the study of more general models. Regarding implementation, we used the same structure as [25], which is a standard way of achieving maximum flexibility with the handling of the data.

4.2.3 Integrator

One of the most important and recurrently used parts of the code is the integrator. As with most numerical integrations, the problem of achieving a high accuracy with the least amount of sample points was a major issue of the work. Through trial-and-error we ended up settling for a slightly modified version of a standard adaptive integrator which applies the 13-point Kronrod extension to the standard 4-point Gauss–Lobatto quadrature on every subinterval whenever needed, according to what is presented in [26].

The recipe for this integrator is straightforward: for a given interval, evaluate the function at thirteen points, weigh the results according to the fixed weights of the Kronrod quadrature and compare the result to applying the same quadrature to five subintervals of equal length. If the absolute value of the difference of the results is within the tolerance bounds, the result is accepted and returned. Otherwise, the routine is started in each one

of the five subintervals, until convergence or until the point separation becomes smaller than the tolerance.

A very positive aspect of this integrator is its speed in comparison to others that we tested. Due to the fact that we work with complex-valued functions, regular library-integrators (like GSL) require that the integrand be split into real and imaginary part, so as to have real-valued functions. However, since we use the absolute value of the difference of the results, we just integrate once and directly obtain the result, even when this is complex.

4.3 Data analysis

In this section we cover the checks and analyses that we perform once an mfRG flow has been run. These checks are divided into three main categories: direct, derived and fulfillment checks.

Direct checks verify physical conditions that the quantities computed directly must fulfill (which are not already imposed by the implementation). Important examples are the conditions $\mathrm{Re}\Sigma^K(\nu) = 0$ implied by the fluctuation-dissipation theorem (FDT) and $\mathrm{Im}\Sigma^R(\nu) < 0$ required by causality. The susceptibilities must also fulfill the bosonic version of the FDT [14]. More generally, the real part of the Keldysh component of any two-particle correlator must vanish. Checking these conditions turns out to be an efficient tool for debugging the code.

Derived checks make up the second category of tests. They are performed on quantities derived from those computed by the code. Examples are checks on normalization of the spectral function $\mathcal{A}(\nu)$ or on its value at zero frequency, which is known analytically. Since $\mathcal{A}(\nu)$ is the local density of states at a frequency ν and each point of an mfRG-flow represents a solution to the model at the given energy scale, the integral of the spectral function must remain constant, regardless of the conditions imposed on the system. Also, for calculations in equilibrium, the Friedel summation rule implies that the value of $\mathcal{A}(0)$ is fixed and, thus, it should not change during the flow [27]. Now, note that $\mathcal{A}(\nu) = -\frac{1}{\pi}\mathrm{Im}G^R(\nu)$, thus $\mathcal{A}(0) = \frac{1}{\pi\Delta}$ effectively checks that $\Sigma^R(0) = \Sigma^H$, i.e. that the mean field solution is not renormalized along the flow. Since the addition of a bias voltage would cause transport through the impurity, one would expect $\mathcal{A}|_{V\neq 0}(0) < \mathcal{A}|_{V=0}(0)$.

The third type of check establish how well the equations that we are actually trying to solve are fulfilled. We take Γ_{fRG} and Σ_{fRG} from our results and use them to calculate

$$\Gamma^\Lambda_{\mathrm{BS}} = \Gamma_0 + \left[\gamma^\Lambda_r\right]_{\mathrm{BS}} \tag{4.10}$$

with

$$\left[\gamma^\Lambda_r\right]_{\mathrm{BS}} = B_r\left(\Gamma^\Lambda_{\mathrm{fRG}}, \left[I^\Lambda_r\right]_{\mathrm{fRG}}\right) \tag{4.11}$$

and

$$\Sigma^\Lambda_{\mathrm{SD}} = L(\Gamma_0, G) + L\left(B_p\left(\Gamma_0, \Gamma^\Lambda_{\mathrm{fRG}}\right), G\right). \tag{4.12}$$

Note that everything on the right-hand-side of Eqs. (4.11) and (4.12) is extracted from the results obtained through a mfRG-flow. Thus, a qualitative and quantitative comparison between the thus obtained "parquet" objects Γ_{BS} and Σ_{SD} allows us to draw conclusions on how well our code solves the equations of the parquet formalism.

To this end, we define at this stage norms for the objects being considered. For this purpose, two natural choices exist since numerical functions have a certain duality to them. If one thinks of $\Gamma = \Gamma_0 + \sum_{r\in\{a,p,t\}} \sum_{i\in 1,2,3} \mathcal{K}_i^r$ and $\Sigma^{R/K}$ as *vectors* storing some values, then a linear-algebra-motivated vector norm $||\cdot||_p$ is sensible. However, thinking of this functions as integrable *functions* would motivate some kind of L_p-norm based on integrability, which is guaranteed as long as the system does not undergo a phase transition [28]. We point out that, though both norms are equivalent for arguments of convergence of sequences (as this is a topological property), they are *not* equivalent for quantitatively analyzing the data, with the finite-dimensional vector-space norm giving more importance to features concentrated around zero, since in our implementation most of the $N^{(i)}_{\mathrm{bos/fer}}$ are below Ω_{scale}.

Given that our interest is to benchmark our method and subject it to strong tests, we opt for the vector-norm, since for frequencies around and close to $\nu = 0$ and $\omega = 0$ is where correctly calculating the behavior of both self-energy and vertex is the hardest. Hence, we opt for the following definition of a p-norm for self-energy and vertex, thinking of them as vectors

$$||\Sigma||_p = \left(\sum_{i_K=R,K} \sum_{\nu_i} |\Sigma^{i_K}(\nu_i)|^p \right)^{1/p} \tag{4.13a}$$

$$||\mathcal{K}_1||_p = \left(\sum_{i_K=\mathcal{K}_1^{\mathrm{indep}}} \sum_{r\in\{a,p,t\}} \sum_{\omega_i} |[\mathcal{K}_1^r(\omega_i)]^{i_K}|^p \right)^{1/p} \tag{4.13b}$$

$$||\mathcal{K}_2||_p = \left(\sum_{i_K=\mathcal{K}_2^{\mathrm{indep}}} \sum_{r\in\{a,p,t\}} \sum_{\omega_i,\nu_j} |[\mathcal{K}_2^r(\omega_i,\nu_j)]^{i_K}|^p \right)^{1/p} \tag{4.13c}$$

$$||\mathcal{K}_3||_p = \left(\sum_{i_K=\mathcal{K}_3^{\mathrm{indep}}} \sum_{r\in\{a,p,t\}} \sum_{\omega_i,\nu_j,\nu'_k} |[\mathcal{K}_3^r(\omega_i,\nu_j,\nu'_k)]^{i_K}|^p \right)^{1/p}, \tag{4.13d}$$

where $\mathcal{K}_i^{\mathrm{indep}}$ is the set of indices of the independent components of the vertex, and the frequencies ν_i, ω_i, ν_j and ν'_k are sampled from the corresponding frequency grids. Notice we include automatically the whole information of all channels and all independent Keldysh components in the vertices, in order to have a single number per diagrammatic class. The parameter p is completely free in our implementation. We also include support for the limit $p \to \infty$, which represents the maximum norm. Throughout this work we use the choice $p = 2$ for the Euclidean norm and thus omit the subscript.

This concludes our discussion of the implementation of the code and we now turn to the presentation of the results obtained.

Chapter 5

Results

In this chapter we present and analyze the results our code is able to produce. We divide the Chapter into five parts: (i) a discussion on the specifications used for the productions of results; (ii) the presentation of calculations in equilibrium; (iii) an analysis of these according to the criteria presented in Sec. 4.3; (iv) an analysis of how the error of our computations scale; and (v) a brief overview of the results we obtain for non-equilibrium calculations and for different temperatures. Since the code is still in development and the project is ongoing, we only present results which include up to the $\mathcal{K}_2$ class and that go up to two loops. However this incomplete flow already allows us to get a glimpse at the capabilities of the mfRG. We also compare our results with previous advances done in the field of fRG, reported in [6], which we briefly introduce here.

Static-feedback fRG Conventional fRG, as was mentioned in Chap. 2, has some bias towards ladder-type diagrams, since these are the ones which are calculated fully along a fRG flow, whereas diagrams that include channel-mixing are computed only partially. Hence, a way to improve on the conventional fRG without fully extending the formalism is then to statically simulate the contributions of the complementary channels r' in calculations for channel r. This is, in essence, what the static-feedback approximation, as used in [6], does. Since the approximation does not improve on the frequency parametrization of the vertex, it can only be meaningfully implemented in our case for calculations including the $\mathcal{K}_1$ class *only*[1]. For details on the derivation see Chap. 6 of [6].

The important result for us is that, to statically include the contributions of the complementary channels, an extra constant term must be added to the value of the vertex. For channels a and t, $\mathcal{K}_1^{a/t}(\omega = 0)$ must be added. The p channel behaves slightly differently, with the static contributions being $\mathcal{K}_1^{p}(\omega = 2\mu)$. Hence, a fRG calculation in the static-feedback approximation would see the following replacements on the right hind side of the

[1] Calculations that include either up to $\mathcal{K}_2$ or to $\mathcal{K}_3$ automatically include fully frequency-dependent channel mixing diagrams and, hence, automatically improve on the static-feedback approximation.

flow equations:

$$\begin{aligned}\mathcal{K}_1^a(\omega_a) &\to \mathcal{K}_1^a(\omega_a) + \mathcal{K}_1^p(2\mu) + \mathcal{K}_1^t(0)\,,\\ \mathcal{K}_1^p(\omega_p) &\to \mathcal{K}_1^a(0) + \mathcal{K}_1^p(\omega_p) + \mathcal{K}_1^t(0)\,,\\ \mathcal{K}_1^t(\omega_t) &\to \mathcal{K}_1^a(0) + \mathcal{K}_1^p(2\mu) + \mathcal{K}_1^t(\omega_t)\,.\end{aligned} \tag{5.1}$$

Having introduced this approximation, we are now ready to present our obtained results.

5.1 Specifications of the calculations

Whenever one develops a new tool of study, its effectiveness at predicting results in known regimes must be tested. Hence, we first present our results for cases in which the solution of the SIAM is known. This means we contrast our obtained results with those that the numerical renormalization group (NRG) [12, 29] provides. The NRG has, since its introduction by Wilson in 1975, been a standard tool for solving quantum impurity systems, since it is specially tailored for this purpose. Hence, we regard it as our benchmark standard.

5.1.1 Values for the constants

In order to have a standardized testing ground for our method, we defined fixed values for all of the parameters named at the beginning of Chapter 4. We provide Table 5.1 for reference of the chosen values.

5.1.2 Initialization

The initialization of the flow is a very important specification for the analysis of the results, since it yields the starting point of the calculations. In theory, one would wish to start the flow at $\Lambda \to \infty$ or, equivalently, at $U/\Delta = 0$. At this point, initializing the `fullvert` to have only the `irred` vector different from zero containing the physical information of Γ_0 and the `self-energy` to the Hartree term Σ^H would be ideal. Since we are however limited by floating-point arithmetic, we must start the flow at finite Λ_{ini}, which means we need to make pre-start computations to initialize the self-energy and the vertex from. This we do using second-order perturbation theory. Hence, both the vertex and the self-energy are non-trivial at the beginning, with the exact values following:

$$\mathcal{K}_1^r = B_r(\Gamma_0, \Gamma_0)\,, \tag{5.2a}$$

$$\mathcal{K}_2^r = 0\,, \tag{5.2b}$$

$$\begin{aligned}\Sigma &= \Sigma^H + L(B_a(\Gamma_0, \Gamma_0), G)\\ &\equiv \Sigma^H + \frac{1}{2} L(B_p(\Gamma_0, \Gamma_0), G)\,.\end{aligned} \tag{5.2c}$$

	Parameter	Value
Physical parameters	T	0.01
	μ	0
	U	1
	Γ	$\frac{1}{3}$
	V	0
Freq. grid	$\Omega := \Omega^+ = \Omega^-$	300
	Ω_{scale}	25
	$N_{\text{fer}}^{(1)} = N_{\text{bos}}^{(1)}$	301
	$N_{\text{fer}}^{(2)} = N_{\text{bos}}^{(2)}$	201
ODE **flow. grid**	Λ_{ini}	1000
	Λ_{fin}	0
	Λ_{scale}	$\frac{1}{200}$
	nODE	50
Technical parameters	`interpolate_tol`	10^{-9}
	`integrator_tol`	10^{-6}

Table 5.1: Table of values of parameters used for result production runs. Setting $U = 1$ means that energy, temperature and frequency are measured in units of U.

Here the retarded component of Σ^H is $U/2$ and its Keldysh component vanishes. Note that the constraint of spin conservation implies that $B_t(\Gamma_0, \Gamma_0) = 0$, which yields a null $\mathcal{K}_1^t$ at the beginning of the flow.

The assumption behind this truncation at second order is that, given that $U/\Delta \approx 1/500$ at this stage, the incursion in an error of order $\mathcal{O}\left((U/\Delta)^3\right)$ is acceptable. This is further supported by the fact that we have $\Omega \ll \Lambda_{\text{ini}}$ (cf. Table 5.1), which means that, at initialization, both the vertex and the self-energy will not have completely decayed to a negligible value, in comparison to their maximal ones, inside the sampling intervals. However, since at Λ_{ini} the absolute values of these functions is small (remember we would start from these being exactly zero), we tolerate the starting error for this work. Extending the sampling intervals implies having to increase the number of sampling points to still be able to resolve the sharp features, which develop near to $\nu = 0$ and $\omega = 0$ as the flow progresses. This means a much higher numerical cost, which we seek to avoid. Another possibility to avoid this caveat is to reduce Λ_{ini} to match the scale of Ω. However, this turns out to yield a higher error at the beginning than our current version. A solution to this trade-off problem can be to implement an adaptive frequency grid, which scales the limits of the sampling intervals according to Λ along the flow. Another option is the implementation of initialization conditions more consistent with the parquet equations. This could be achieved by increasing the order of the perturbation theory calculated or iterating the

initial condition until self-consistency is achieved. This second option is specially powerful, since if ensures that the solutions generated by the code fulfill the parquet equations along the flow for as long as the interaction strengths remain low enough for the multiloop fRG not to break down.

5.2 Equilibrium results

In this section we present the main results of this work. These comprise the *independent* components of the vertex with a physical interpretation as well as the self-energy. As two-particle bosonic objects, the susceptibilities and, equivalently, the two independent $\mathcal{K}_1^r$ components of the vertex also turn out to have exact analytical properties that allow us to call them retarded[2] and Keldysh. The retarded component of the vertex, at $\mathcal{K}_1$ level, corresponds to $\mathcal{K}_1^{11|21}$ for all channels and the Keldysh one to $\mathcal{K}_1^{11|22}$ for the a and t channels and $\mathcal{K}_1^{12|12}$ for the p channel.

5.2.1 Susceptibilities

We begin by presenting the results of the spin susceptibility, which is, according to what was discussed in Chapter 3, directly related to the values of $\mathcal{K}_1/U^2$.

Figure 5.1 shows that, as expected for small interaction strengths, $U/\Delta \lesssim 1$, the conventional Keldysh fRG scheme, i.e. only including the $\mathcal{K}_1$ classes performs pretty well, as do also the flows including the $\mathcal{K}_2$ classes. The static-feedback approximation, which starts to deviate already at low interaction strengths, will be analyzed later. That the results with and without the $\mathcal{K}_2$ class are similar in this regime is hardly surprising, since diagrams in the $\mathcal{K}_2$ class are of order $\sim \mathcal{O}\left((U/\Delta)^3\right)$. We expect these contributions to act as small corrections, mostly around $\omega = 0$, where the solutions indeed separate. At intermediate interaction strengths $1 \lesssim U/\Delta \lesssim 4$, these results allow us to confidently assert that the conventional fRG breaks down. Panel (b) of Fig. 5.1 clearly shows that the results of the $\mathcal{K}_1$ run strongly deviate from those of NRG. However, it is promising to see that: (a) the inclusion of the $\mathcal{K}_2$ class, i.e. using a more complex frequency parametrization and including channel mixing, improves drastically the behavior of the susceptibility; and (b) the inclusion of higher loop corrections further improve on the approximation.

The inclusion of the $\mathcal{K}_2$ class, first at one-loop level, amounts to including diagrams which are left out in the conventional fRG. An example of these are eye-diagrams of Ref. [5]. These are the kinds of diagrams that make up the building blocks of the diagrams that are partially computed in this scheme, as are the simple loops in the case of the conventional fRG. The extension of this truncation to include 2-loop diagrams calculates these diagrams fully. In terms of what was said in Chapter 2, this amounts to partially simulating the

[2]Since we decided our convention for saving independent components in order of appearance on Table 3.1, we actually save *advanced* objects but through a simple complex conjugation we obtain the results for the retarded objects we present here.

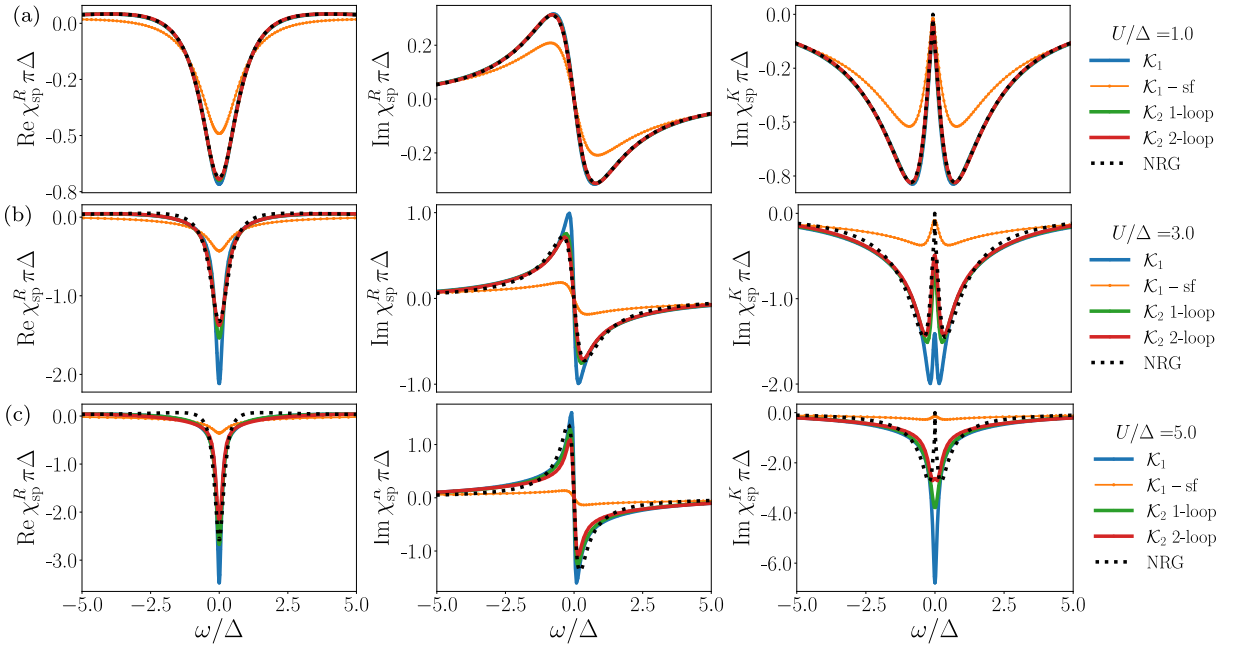

Figure 5.1: χ_{sp} at three values of the effective interaction strength. A FDT requires that $\mathrm{Re}\chi^K_{\mathrm{sp}} = 0$. We omit plots for it, since it remains below 10^{-12} for all interaction strengths and all kinds of flows.

contributions of the $\Gamma^{(6)}$ vertex. Of all the results presented here, only the ones for 2-loop calculations do this and, hence, really start to represent the capabilities of the mfRG.

Leaving out the $\mathcal{K}_3$ class means that we are still not fully computing *all* diagrams that are generated along the fRG flow. This then leads us to incur in an error of order $\mathcal{O}\left((U/\Delta)^4\right)$, which scales similarly as the error of the parquet approximation (recall Sec. 2.2). This is then what implies the breakdown of all approximations for high interaction strengths $U/\Delta \gtrsim 4$. Important to point out is that with the current version of the code, instabilities arising from the breakdown of the physical approximation cause the code to idle and not converge anymore. This happens for $U/\Delta \approx 5.9$ for $\mathcal{K}_2$ 2-loop; shortly after the results of that run become non-physical.

Notably, the static-feedback approximation consistently underestimates the value of χ_{sp}, be it the retarded or the Keldysh component. Moreover it slightly violates the fluctuation dissipation theorem (FDT), with $\mathrm{Re}[\chi^K_{\mathrm{sp}}]^{\mathrm{sf}} \sim 10^{-10}$ in the worst case, several orders or magnitude larger than numerical zero[3] and the other results, yet still negligibly small. This may lie in the kind of processes that the static-feedback approximation takes most heavily into account, since it tries to account for a whole RPA-ladder for each channel and add this contribution to the others.

[3]Floating point decimal expansion, the format of numbers used by computers [30], allows, with the double precision format of C++ , to confidently say that anything below 10^{-16} is equivalent to zero.

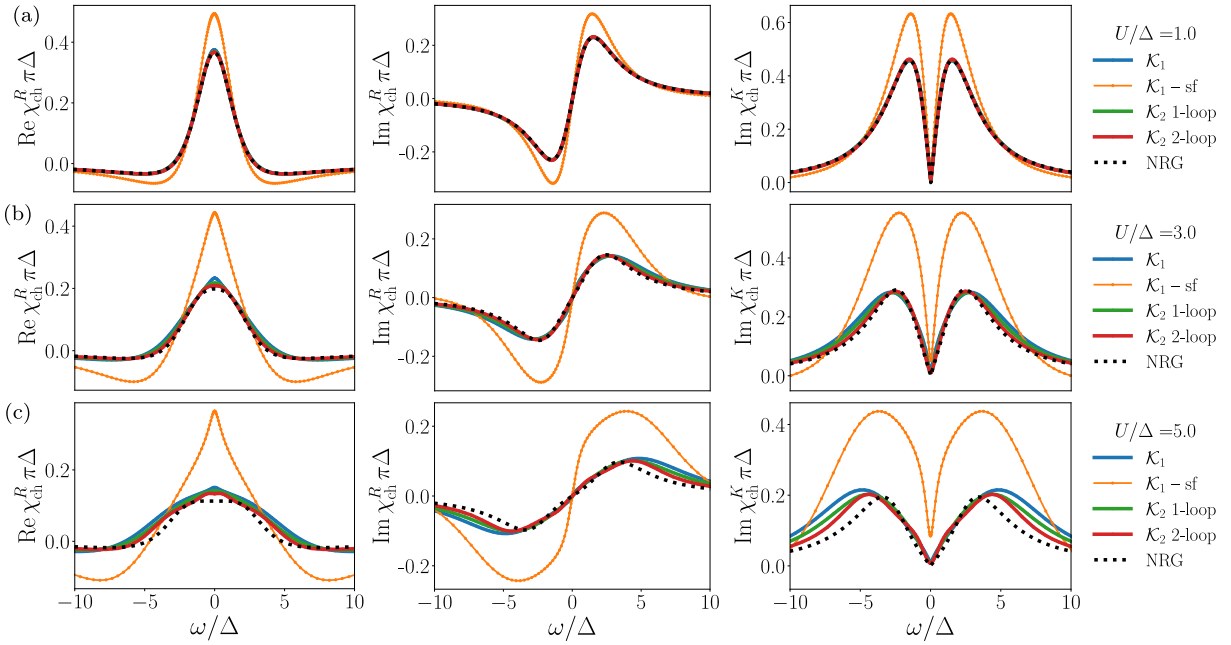

Figure 5.2: χ^K_{ch} at three three values of the effective interaction strength. A FDT requires that $\mathrm{Re}\chi^K_{\mathrm{ch}} = 0$. We omit plots for it, since it remains below 10^{-12} for all interaction strengths and all kinds of flows.

Turning now over to the charge susceptibility (Fig. 5.2) we see a similar behavior as with the spin susceptibility, which is quite encouraging. As well as before, the requirement of the FDT ($\mathrm{Re}\chi^K_{\mathrm{ch}} = 0$) is broken most strongly by the calculations with the static approximation, but remain negligibly small. Curiously, the static-feedback approximation has in this case the tendency to *overshoot* on the value of χ_{ch}. Together with the previous results, this indicates that the static inclusion of the complementary channels actually increases the bias of fRG towards some specific kinds of processes. It also indicates that the approximation fails strongly at resolving the vertex correctly. However, as will be seen later, it still produces good results for Σ and $\mathcal{A}$, so it retains a certain relevance. Notably, no comment is made in [6] about the quality of the approximation in regard to the accuracy of the vertex.

As noted in Chap. 3 and in [23], the charge susceptibility can be computed as $2\mathcal{K}^t_1 - \mathcal{K}^a_1$. We observe that in the particle-hole symmetric case, $\chi_{\mathrm{ch}} = \mathcal{K}^p_1$. This component of the vertex always corresponds to the pairing susceptibility χ_{pair} [20] but, in the case we consider, these two susceptibilities turn out to be exactly equal. This we observe for runs of all configurations. A plausibility argument for this behavior in our case comes from the last appendix of Ref. [4]. The authors provide there a proof for the equivalence of the charge- and pairing susceptibilities for the 2-D Hubbard model for the case of half-filling, i.e. particle-hole symmetric, evaluated at specific momentum values. Since the SIAM has no momentum dependence, we expect the same kind of argument to apply for our case,

specially since we observe the equivalence for equilibrium and non-equilibrium calculations alike.

This match between the $\mathcal{K}_1$ components of the vertex yields an interesting and quite useful relation between them: in the particle-hole symmetric case, one of the $\mathcal{K}_1$'s is redundant. Hence, if performing calculations in a particle-hole symmetric setting, one can save computation time exploiting this symmetry. Further, if the cross-symmetry of the p channel is also respected, the more expensive computation of the t vertex can be avoided (recall that the equation for $\dot{V}^t$ included evaluations of both V and $\hat{V}$, whereas $\dot{V}^{a/p}$ only depend on V). This could then effectively cut the computation time of the $\mathcal{K}_1$ class in half. However, one must also consider, according to what was said in Sec. 3.4, that the computation times of $\mathcal{K}_1$ are negligible in comparison to those of any of the $\mathcal{K}_2^r$. Although not yet tested, we hypothesize that a similar relation holds for the more complex diagrammatic classes. However, should this be the case, it will probably mix Keldysh components, since the causal structure of the components does not correspond to simply retarded/advanced or Keldysh.

5.2.2 Self-energy

Now we turn to the other directly calculated quantity, the self energy. By having only one propagator in its flow equation and integration intervals of up to double the length of the sampling intervals, there are several contentious points for the self-energy that must be taken into account. First, since we take the vertex to be zero outside of the sampling intervals, contributions of high-energy modes are not completely accounted for, leading to unphysical behavior of the self-energy at the beginning of the flow. Thus, we observe that $\mathrm{Im}\Sigma^R(\nu \approx 0) > 0$ at the beginning of the flow, which breaks causality. However, this error *diminishes* during the first steps of flow because, quite rapidly, the features of both the self-energy and the vertex are completely contained in the sampling interval, as $\Lambda < \Omega^+$. Thus, though in Fig. 5.3, very much at the beginning of the flow, we observe that causality is broken in every case, further down in the flow this is corrected. We actually see this already be solved at scale of $U/\Delta \lesssim 2$. We note that this issue, as well as that of a proper initialization, could be solved by the implementation of an adaptive frequency grid, currently under implementation. Another possibility is to analytically account for the relevant high-energy asymptotic contributions to the integrals of the vertex. We actually explored this possibility but these turn out to trigger strong instabilities at more interesting interaction strength regimes.

A noteworthy detail is how well the $\mathcal{K}_2$ 2-loop results behave at intermediate/large interaction strengths ($U/\Delta \approx 4$) for small frequencies. This frequency range is notoriously hard to calculate correctly, yet these results agree perfectly with NRG. However, for intermediate values of the frequencies, $\mathcal{K}_2$ 1-loop seems to fit better to the actual results, indicating that there is room for improvement in the calculation of the mfRG loop corrections. This is also exemplified in the appearance of unphysical features in the results from the $\mathcal{K}_2$ 2-loop flow. The bottom row of Fig. 5.3 shows that the self-energy develops causality-breaking features, namely $\mathrm{Im}\Sigma^R \not< 0$ and $\mathrm{Im}\Sigma^K(\nu \gtrsim 0) \not< 0$. These unphysical

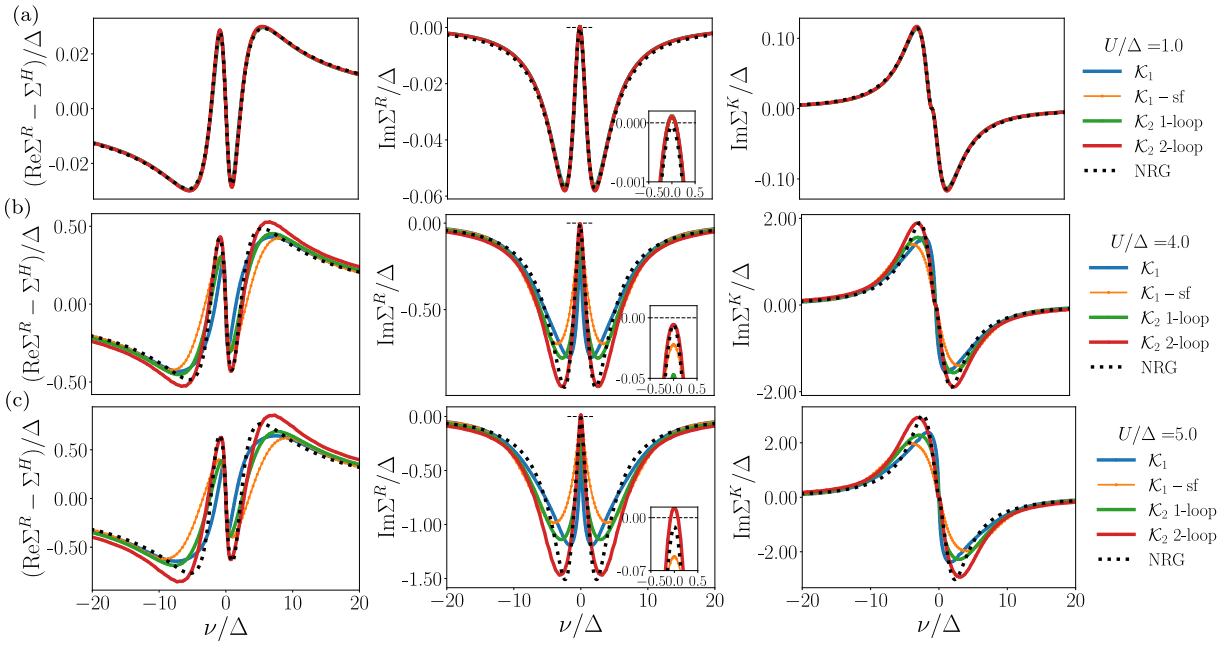

Figure 5.3: Σ at three values of the effective interaction strength. Notice the violation of causality for high values of U/Δ as $\mathrm{Im}\Sigma^R > 0$. $\mathrm{Re}\Sigma^K < 10^{-12}$ throughout and is, hence, omitted from the plots.

behaviors quickly translate into large discontinuities of the functions, leading to the integrator failing to converge and the calculations to fully break down. These features may be caused by insufficient accuracy in resolving the high-frequency asymptotic behavior of the vertex. Note that, in the Keldysh formalism, it is much harder to determine how the components of the vertex decay than in the Matsubara case, where all components of the vertex follow a simple inverse power law.

An equally remarkable fact is that, although the static-feedback approximation fails to improve on conventional fRG for the calculation of the vertex function, it does so on its calculation of both components of Σ. This is striking, given that it fails to determine correctly *all* components of the vertex (disagreement with both susceptibilities presented previously imply this thanks to their relationships with the $\mathcal{K}_1$ components of the vertex). It even fares better than the $\mathcal{K}_2$ 1-loop calculation for small frequencies and intermediate/large interaction strengths. This may, however, be more a coincidence than an actual achievement of the method since one would rather lean towards discarding a solely $\mathcal{K}_1$-based approach at these interaction strengths.

5.2.3 Spectral function

Having presented and discussed the results we obtain for the directly calculated quantities, we now turn to the derived one: the spectral function. This is a very important quantity, since it describes the excitation spectrum, i.e. the local density of states of the system. As

mentioned in Sec. 4.3, Friedel's sum rule fixes $\mathcal{A}(\nu = 0) = \frac{1}{\pi\Delta}$ and the integral of $\mathcal{A}$ over all frequencies must be conserved throughout the entire flow. Hence, we define a way to measure the latter condition as

$$\mathcal{N}(U/\Delta) := \int \mathrm{d}\nu \mathcal{A}^{U/\Delta}(\nu)\,. \tag{5.3}$$

Hence, the closer the normalization $\mathcal{N}$ is to 1, the better the condition on normalization of the spectral function is fulfilled.

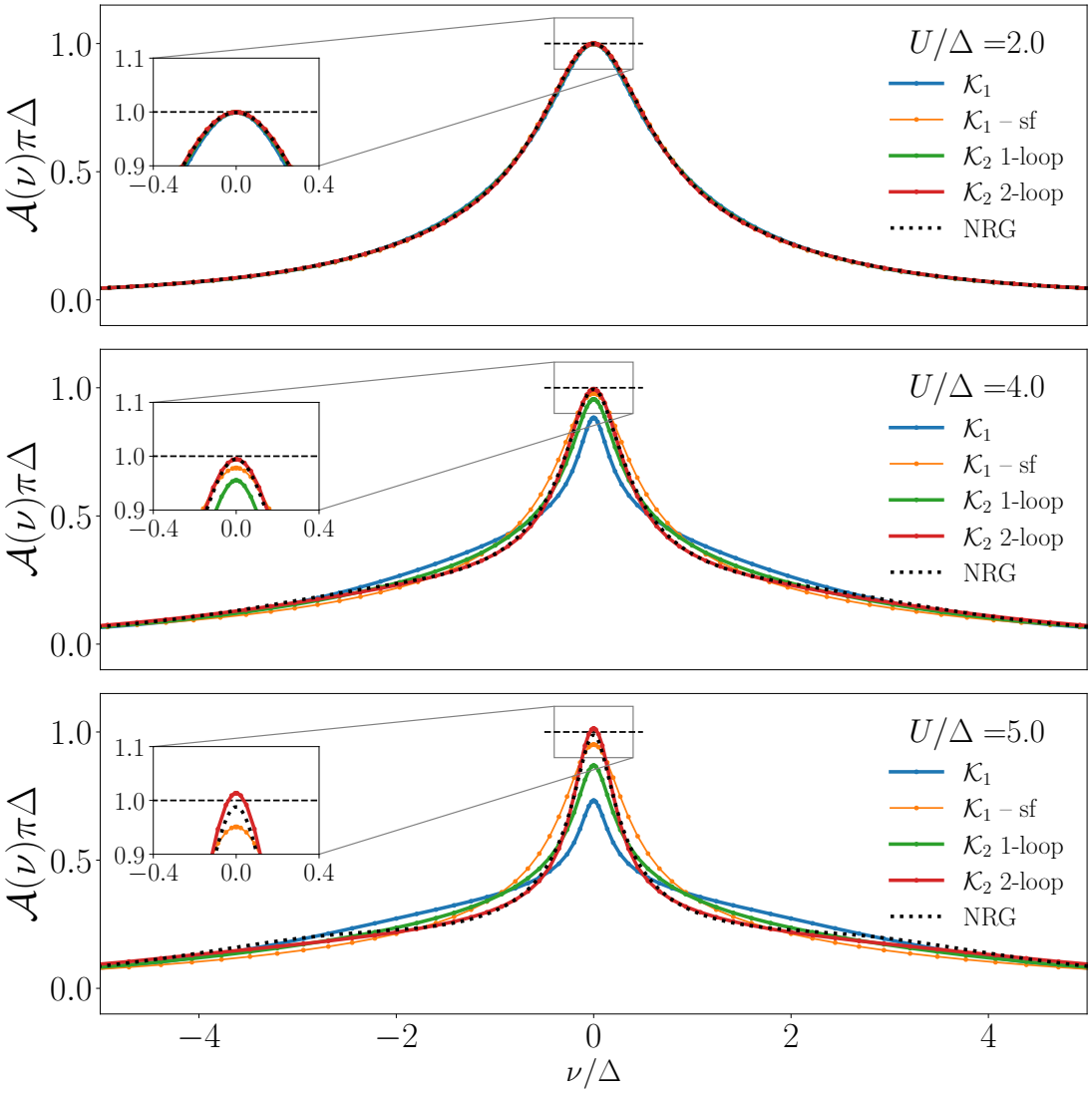

Figure 5.4: $\mathcal{A}$ at three values of the effective interaction strength. Notice the slight hint of the NRG results to show Hubbard bands, notably missing in all of our results, probably due to the absence of the $\mathcal{K}_3$ class.

As before with the self-energy and the susceptibilities, we see in Fig. 5.4 an increase in performance of the mfRG solutions as one includes more and more components into the

calculation. Notable is that all four methods give very good results for low to intermediate values of U/Δ, even when the self-energy already shows stronger deviations in this regime. This is, however, due to the decreasing impact that the values of the self-energy have on the spectral function as $|\nu|$ increases. To see this, consider the full expression for the spectral function

$$\begin{aligned}\mathcal{A}(\nu) &= -\frac{1}{\pi}\mathrm{Im}G^R(\nu) \\ &= \frac{1}{\pi}\frac{\Delta - \mathrm{Im}\Sigma^R}{\left[\left(\nu - (\mathrm{Re}\Sigma^R - \Sigma^H)\right)^2 + \left(\Delta - \mathrm{Im}\Sigma^R\right)^2\right]} \\ &= \frac{1}{\pi\Delta}\frac{\left(1 - \frac{\mathrm{Im}\Sigma^R}{\Delta}\right)}{\left[\left(1 - \frac{\mathrm{Im}\Sigma^R}{\Delta}\right)^2 + \left(\frac{\nu}{\Delta}\right)^2\left(1 - \frac{\mathrm{Re}(\Sigma^R - \Sigma^H)}{\nu}\right)^2\right]}.\end{aligned} \tag{5.4}$$

As both components of the self-energy decay to either Σ^H or to 0 as $|\nu|$ increases, we see that the terms including Σ^R fade away as $|\nu| \to \infty$.

Shown in Fig. 5.4 for this low/intermediate regime is only $U/\Delta \geq 2$ but Friedel's sum rule is fulfilled for all values below this. Notice that the initial unphysicalities of $\mathrm{Im}\Sigma^R > 0$ around $\nu = 0$ are the ones that can affect this, and their effect here is negligibly small. This is due to the fact that the absolute value of $\mathrm{Im}\Sigma^R(0)$ at the beginning of the flow is small in comparison to the initial value of $\Delta_{\mathrm{ini}} = \frac{\Gamma + \Lambda_{\mathrm{ini}}}{2} = \frac{1/3 + 1000}{2} \approx 500 \gg 10^{-4}$ and, hence, $\frac{\mathrm{Im}\Sigma^R}{\Delta} \approx 0$. Hence, both terms $\left(1 - \mathrm{Im}\Sigma^R/\Delta\right)$ in Eq. (5.4) basically reduce to a 1, while the value of $\mathrm{Re}\Sigma^R(0)$, although equal to Σ^H, is irrelevant thanks to the prefactor $(\nu/\Delta)^2$. Notice this consideration is rendered mute with increased resolution in the calculations.

The fact that the $\mathcal{K}_2$ 2-loop run develops a non-small positive $\mathrm{Im}\Sigma^R$ for high U/Δ is then translated at this level to the breaking of the Friedel's sum rule and $\mathcal{A}_{\mathcal{K}_2\ \text{2-loop}}(0) > \frac{1}{\pi\Delta}$.

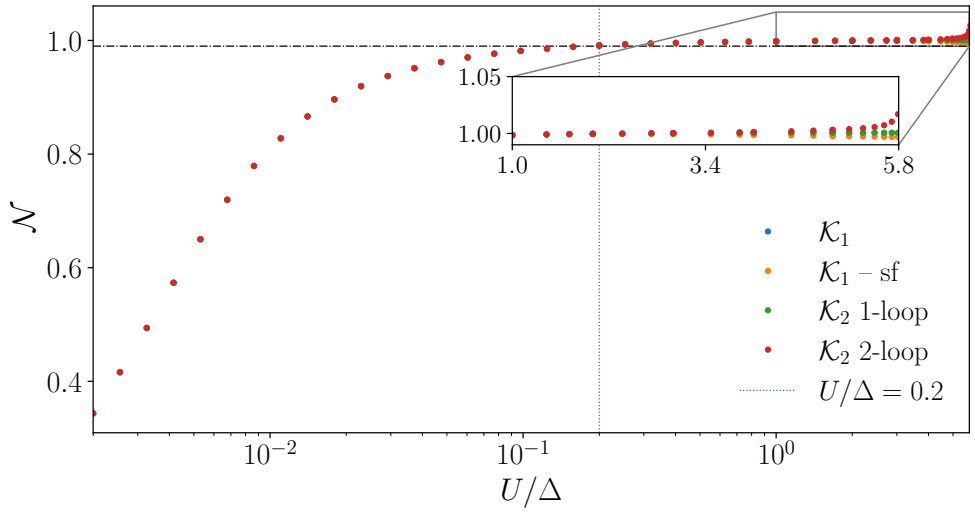

Figure 5.5: Evolution of the normalization of the spectral function along the flow.

Now we analyze the evolution of $\mathcal{N}$ throughout the flow. For this purpose we present Fig. (5.5). Here we see a striking behavior. The first ~ 20 points are below the dotted horizontal line of $\mathcal{N} = 0.99$, with $U/\Delta = 0.2$ being the first point at which $\mathcal{N}$ is within 1% of its theoretical value. This may be worrying at first glance since, for the first points of the flow, the spectral function is far from being properly normalized. Again, the reason here is the discrepancy between the scales set by Λ_{ini} and Ω, equivalent to a lack of resolution at the beginning of the flow. Until the features of the self-energy are not fully contained inside of the sampling interval, the spectral function is only partially resolved and, hence, many physical states are not counted into the integral. This can also be understood in terms of the dimensionless variable ν/Δ. At the beginning of the flow, its possible interval is shortened to $[-\Omega^-/\Delta_{\text{ini}}, \Omega^+/\Delta_{\text{ini}}] \sim [-3/5, 3/5]$. Clearly, including only frequencies fulfilling $|\nu/\Delta| \lesssim 3/5$ is far from sufficing in resolving the spectral function. Hence, only for $U/\Delta \gtrsim 0.2$ does the dimensionless frequency interval become big enough, so that one can safely neglect the contribution of the tails of $\mathcal{A}$ to the integral. Once again, this issue could be resolved by the implementation of an adaptive frequency grid. With it, th sampling interval stays wide enough at arbitrarily high Λ_{ini} while retaining the ability to, later in the flow, fully resolve the sharp features around the origin. Work in this direction is currently in progress.

Though this problem is recurring, we point out that it is due to the necessary trade-off that a static frequency grid implies. No static frequency grid, subject to limited computing resources, can possibly resolve both extremely smeared objects at arbitrarily high Λ_{ini} while simultaneously offering a high-enough sampling-point density around $\nu = 0$ and $\omega = 0$ for the sharp features of both the vertex and the self-energy at the later stages of the flow, as $\Lambda \to 0$. Thus, we opted for giving the latter a much more prominent role, which allows us to reach intermediate/high interaction strengths of $U/\Delta \approx 5$ for $\mathcal{K}_2$ 2-loop calculations stably and reliably. Optimizing for perfect agreement at the beginning of the flow leads to a too-low density of sampling points, which reduces reliability of the results and requires higher $N^{(i)}_{\text{bos/fer}}$ values, drastically increasing computing times. Thus, since the slight errors at the beginning of the flow are resolved before the intermediate regime of interactions strengths $1 \lesssim U/\Delta \lesssim 4$ is reached, and these do not majorly affect any physical quantity being calculated, we stand by our compromise, knowing also that the way to improve on it is the implementation of adaptive frequency grids.

Notably, we do not observe the appearance of Hubbard bands or of a hint thereof for $\mathcal{A}$ at any interaction strength U/Δ shown here. However, this may be due to the omission of the $\mathcal{K}_3$ class, since the development of said bands is expected at $U/\Delta > 1$, where the contributions due to these kinds of diagrams gain importance. We actually do observe the formation of shallow and broad peaks for $U/\Delta > 5$, which is a regime in which we expect all of our results to not be valid anymore. This points to the fact that the exclusion of the $\mathcal{K}_3$ class from the calculations rather delays the formation of these structures, which are anyway only slightly noticeable in the NRG results in the shown interaction strength regime.

5.2.4 Parquet equations

Having looked at the spectral function, we now investigate to what extent our (m)fRG solutions solve the equations of the parquet formalism (recall Chap. 2). To do so, we make use of the norm defined in Sec. 4.3 and we look at how the norms of both the (m)fRG results as well as that of the quantities calculated according to Eqs. (4.11) and (4.12) evolve during the flow, at how the norm of the difference scales and at how the relative error behaves. For this analysis we omit results obtained using the static-feedback approximation, since the aim of this scheme is not to better solve the parquet equations.

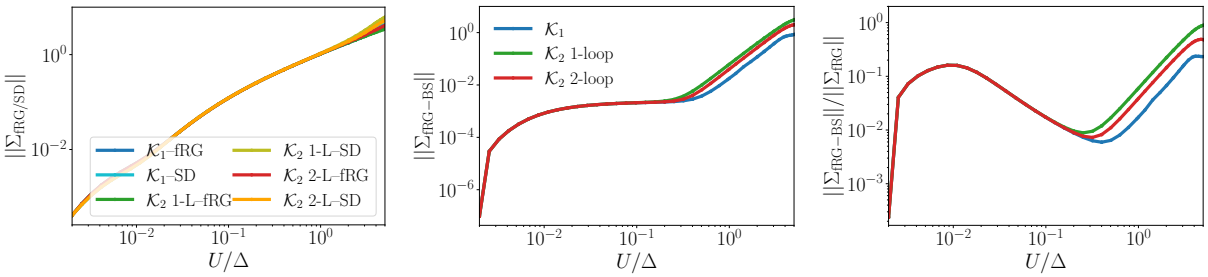

Figure 5.6: Error analysis of the self-energy. Evolution of (a) the norms of; (b) the difference between and; (c) the relative error between the fRG and Schwinger–Dyson self-energies along the flow.

We begin by analyzing the behavior of the self-energy. Notice in Fig. 5.6 how at the beginning of the flow the long-range features of the self-energy that are not fully contained in the sampling intervals cause both the absolute and, hence, also the relative error to grow quickly. This increase is however halted at roughly $U/\Delta = 0.01$, after which the increase in norm does not outpace the growth of the absolute error. Thanks to the latter growing slowly for $0.01 \lesssim U/\Delta \lesssim 0.3$, the relative error even decreases in this regime, which reflects the fact that, for low interaction strengths, we expect both conventional fRG and mfRG to perform rather well and solve the self-consistent equations of the parquet formalism correctly. For the intermediate and strong interaction-strength regimes we see that the relative error increases roughly equally for all flows. Notice that the $\mathcal{K}_2$ 2-loop flow better solves the Schwinger–Dyson equation than the 1-loop truncation at every step of the flow in this regime. That $\mathcal{K}_1$ fares comparatively better here in comparison to both $\mathcal{K}_2$ flows is not relevant, since, as Fig. 5.3 shows, a sole-$\mathcal{K}_1$ flow deviates too strongly from the NRG solution to be seriously considered. However, it is interesting to see that the inaccurate flow still retains consistency with respect to the parquet equations.

Following with the $\mathcal{K}_1$ part of the vertex in Fig. 5.7, we see, based on the first points of the flow, that results obtained with second-order perturbation theory fare well in solving the parquet equations, a claim we base on the low absolute and relative errors that are seen at the beginning of the flow. Then, until roughly $U/\Delta = 0.2$, all three solutions behave similarly. At this point in the flow, both errors for the $\mathcal{K}_2$ flows shoot up and $\mathcal{K}_1$'s remains

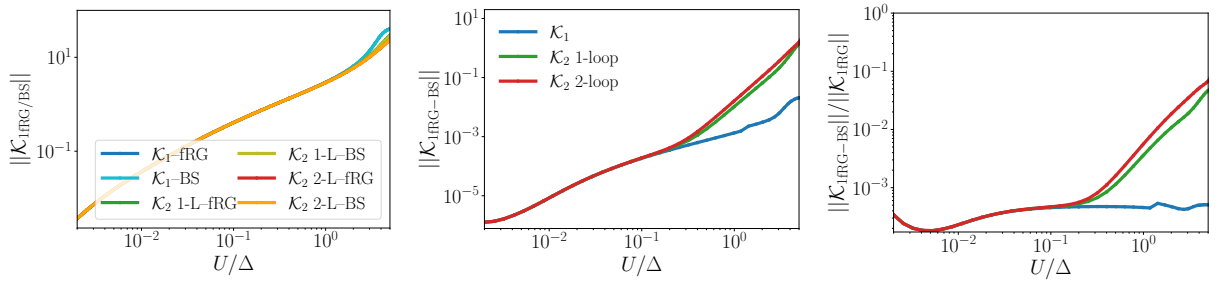

Figure 5.7: Error analysis of the $\mathcal{K}_1$ class. Evolution of (a) the norm of; (b) the difference between, and (c) the relative error between the fRG and the $\mathcal{K}_1$ contributions to the vertex, calculated using the Bethe–Salpeter equations.

low, again signaling that, although inaccurate when comparing the solution with NRG, a conventional fRG flow remains surprisingly consistent in solving the parquet equations, though, according to what was mentioned above, this is no reason to regard this flow as correct or complete. For the case of the $\mathcal{K}_2$ flows, we see an inverted behavior as with the self-energy, with $\mathcal{K}_2$ 1-loop yielding a more parquet consistent $\mathcal{K}_{1\mathrm{BS}}$ than what $\mathcal{K}_2$ 2-loop gives at every step of the flow. This is a rather surprising behavior, mostly due to the fact that the results of the $\mathcal{K}_2$ 2-loop flow are closer to NRG than the $\mathcal{K}_2$ 1-loop in this regime of interaction strengths. Further, as we discuss below, the 2-loop results show a better parquet-consistency than the 1-loop results for the $\mathcal{K}_2$ class. It may be that the way in which the multi-loop corrections affect the values of the $\mathcal{K}_2$ class cause the resulting $\mathcal{K}_{1\mathrm{BS}}$ to differ stronger from the calculated $\mathcal{K}_{1\mathrm{fRG}}$, but a more thorough analysis should be done on this point to explain this discrepancy.

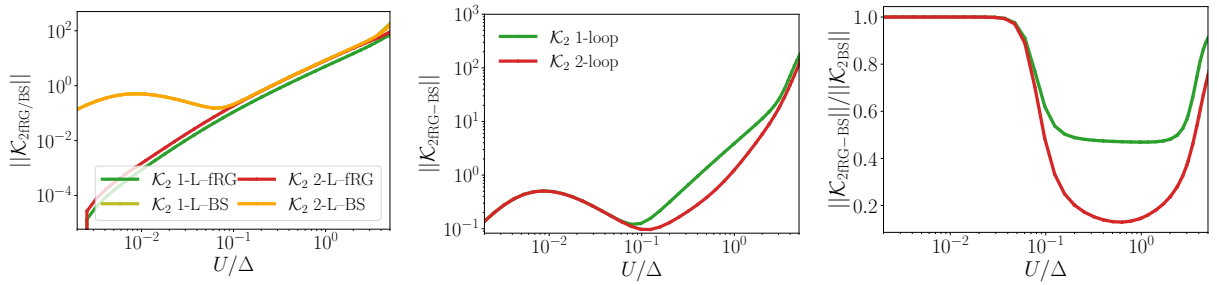

Figure 5.8: Error analysis of the $\mathcal{K}_2$ class. Evolution of (a) the norm of; (b) the difference between, and (c) the relative error between the fRG and the $\mathcal{K}_2$ contributions to the vertex, calculated using the Bethe–Salpeter equations.

Lastly we come to the $\mathcal{K}_2$ part of the vertex. In Fig. 5.8a we see the effects of the SOPT initialization we use: the $\mathcal{K}_{2\mathrm{fRG}}$ component of the vertex is completely zero. This is highly inconsistent with the Bethe–Salpeter equations, which is evidenced in the fact that

$||\mathcal{K}_{2\mathrm{BS}}|| \gg ||\mathcal{K}_{2\mathrm{fRG}}|| \sim 0$ at the beginning of the flow. This is also to be expected, since, at any $\Lambda < \infty$, the vertex will have developed non-zero features in all diagrammatic classes. This naturally implies that the relative error will be quite large for this initial values. Because of this we norm the relative error for $\mathcal{K}_2$ with respect to $||\mathcal{K}_{2\mathrm{BS}}||$ as opposed to the fRG norm we used for the other two objects. Notice that, as the flow progresses and the corresponding features are developed, the fRG solution catches up with the Bethe–Salpeter result for the $\mathcal{K}_2$ vertex. This indicates the fact that during these early stages of the flow the most important contributions come from the $\mathcal{K}_1$ class, in accordance with expectations, since $U/\Delta \ll 1$. However, as $||\mathcal{K}_{2\mathrm{fRG}}||$ becomes comparable to $||\mathcal{K}_{1\mathrm{fRG}}||$ and, hence, the contributions of the $\mathcal{K}_2$ class gain importance, we see that the absolute and relative errors of the $\mathcal{K}_2$ results plunge down. Here, we point out to the fact that, in relative terms, $\mathcal{K}_2$ 2-loop strongly outperforms the one loop variant of the flow, showing proof of the fact that the multiloop corrections yield quantitatively better results than conventional fRG does.

5.2.5 Error scaling

A last point we analyze of these equilibrium solutions is the scaling of the error with U/Δ. To do this, we look at how three telltale quantities evolve during the flow and compare to reference NRG values. These are the value at the origin of $\chi^{\mathrm{R}}_{\mathrm{sp/ch}}(\omega = 0)$ and Z, a standard quantity in contexts of renormalization [11, 31], defined as

$$Z := \left(1 - \partial_\nu \Sigma^R|_{\nu=0}\right)^{-1} . \tag{5.5}$$

These are natural choices of simple quantities that allow us to easily see how the error with respect to NRG behaves along the flow. As for the parquet checks before this, we omit the static-feedback approximation.

To this end, we present Fig. 5.9. Here we adhere to the convention that $\chi_{\mathrm{ch/sp}}(\omega = 0) > 0$, so we actually flip the sign of χ_{sp} with respect to the results shown previously. As one could expect from of previous discussion, $\mathcal{K}_2$ 2-loop fares in all cases much better than the other two kinds of flows. Also, that both $\mathcal{K}_2$ flows are closer to NRG throughout the flow than the $\mathcal{K}_1$ results is in accordance to what we previously observe. What is most interesting about these plots (especially noticeable in the left graph of Fig. 5.9) is the evolution of the *separation* of the lines. The $\mathcal{K}_1$ flow not only deviates first but also the strongest from the benchmark, which indicates the expected early breakdown of the approximation. The flows which include $\mathcal{K}_2$ performs much better, with the difference remaining minor for both flows for most of the flow until $U/\Delta = 5$.

Due to the fact that a $\mathcal{K}_2$ 2-loop flow generates and fully computes all diagrams to order $\mathcal{O}\left((U/\Delta)^3\right)$, we expect the error of the results associated to its flow to scale like $\mathcal{O}\left((U/\Delta)^4\right)$. A similar statement can be said about the flow of $\mathcal{K}_1$, with the powers replaced by 2 and 3, respectively. The case for $\mathcal{K}_2$ 1-loop is not as straightforward, since it includes diagrams in $\mathcal{O}\left((U/\Delta)^3\right)$, but these are computed only partially, leading to an error scaling also of order $\mathcal{O}\left((U/\Delta)^3\right)$. However, this is not exactly the case here, where we obtain the susceptibilities by dividing the relevant $\mathcal{K}_1$ component by U^2. Hence, we actually have errors scaling like

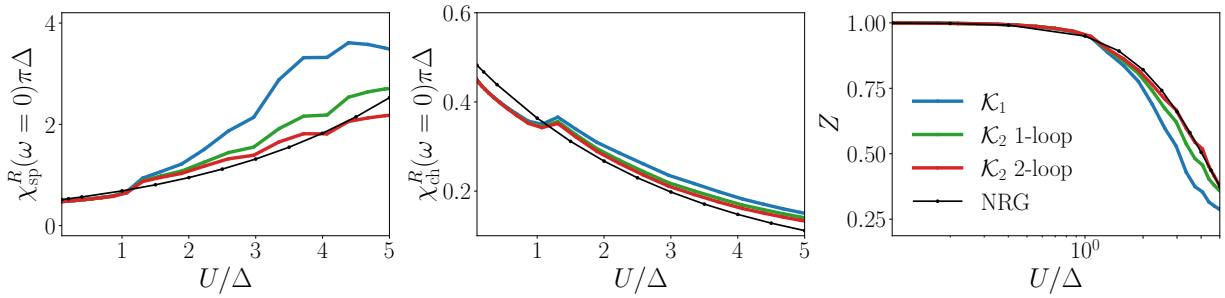

Figure 5.9: Evolution of the error of $\chi^R_{\mathrm{ch/sp}}(\omega = 0)$ and of Z along the flow.

$\mathcal{O}\left((U/\Delta)^1\right)$ and $\mathcal{O}\left((U/\Delta)^2\right)$. Thus, to improve on this, we leave to the future of the project an implementation of an explicit calculation of the susceptibilities, which yields them with a better error scaling. In other words, the implementation of a module that explicitly calculates the susceptibilities and differentiates them from the "flowing susceptibilities" we are currently working with, is a logical step forward for this project. Further, this way of calculating susceptibilities can provide a consistency check for a more advanced mfRG code since, once loop conversion is reached, the results of the flowing and the explicitly calculated susceptibilities should be equal.

An interesting check on the fulfillment of Ward identities can be done by comparing

$$\chi_{\mathrm{e}} := \frac{1}{2}\left(\chi_{\mathrm{sp}} + \chi_{\mathrm{ch}}\right) \tag{5.6}$$

with Z^{-1}. According to [16], a Ward identity implies that

$$\chi_{\mathrm{e}}(0) = Z^{-1}\,. \tag{5.7}$$

Hence, having all three quantities available, we show in Fig. 5.10 how these two quantities, calculated for each one of our flows, compare. Notably, and in accordance with what was said in Chap. 2 regarding the implications of truncation of the infinite hierarchy of Eq. (2.10), conventional fRG results violate the Ward identity much stronger than our multiloop results. This is very encouraging to see, since the mfRG should aid in the restoring of, at least, one-particle conservation laws.

Notice that in the left plot of Fig. 5.10 all (m)fRG-flows start the flow breaking the Ward identity, at $U/\Delta \ll 1$, and all do so similarly as bad. This has again to do with the discrepancy between Λ_{ini} and Ω, which affects disproportionately the calculation of $\chi_{\mathrm{ch/sp}}(\omega = 0)$ in comparison to the effect this has on the *derivative* of Σ^R at $\nu = 0$. Hence, Z^{-1} behaves much better for the (m)fRG results than χ_{e}.

On the right side of Fig. 5.10 we also include a plot for

$$\chi_{\mathrm{o}} := \frac{1}{2}\left(\chi_{\mathrm{sp}} - \chi_{\mathrm{ch}}\right)\,, \tag{5.8}$$

which is involved in another implied equality due to another Ward identity [16]. This one involves $\chi_o(0)$ and $\Gamma(0,0,0)/\Delta$, though which Keldysh components enter in this identity

is unclear. Further work can be done in this direction, but it remains outside ot the scope of the present one. We now pass on to describe our results outside of equilibrium.

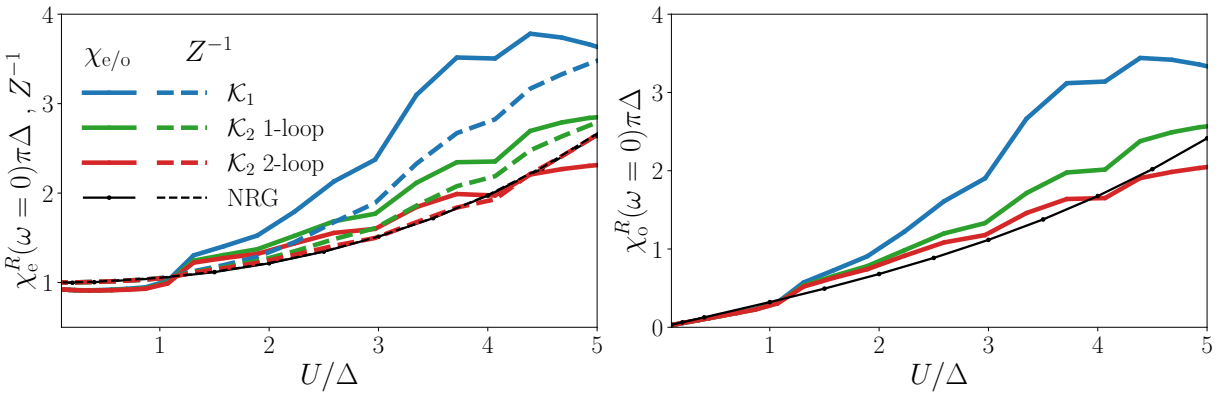

Figure 5.10: Evolution of $\chi_{e/o}$ and Z^{-1}. The closer χ_e is to Z^{-1} the better Ward identities are fulfilled. The value of χ_o is related to $\Gamma(0,0,0)/\Delta$ by another Ward identity.

5.3 Non-equilibrium

Following the thorough discussion of our results for equilibrium calculations, we now present what we obtain for different bias voltages. Though the static-feedback approximation can also be used in this setting, we do not consider it here. The specifications for the runs are equal to those used for equilibrium calculations, with the obvious difference that V/U is now set to different values. Since there are no previous results in this area regarding the susceptibilities to compare ours to, we leave them out of our discussion and thus begin with the self-energy. We show results only for $\mathcal{K}_2$ 2-loop flows since, according to the discussion preceding this section, these give the best results.

Figure 5.11 shows how the self-energy is affected by the inclusion of a bias voltage. The retarded component shows a merger of peaks through smearing caused by V/U and the Keldysh component gets washed off for large voltages, yet remains relatively unchanged in the low/intermediate regime for all interaction strengths. Both real and imaginary components of Σ^R show a strong reduction of the main features for $U/\Delta = 1$ and $V/U \geq 1$ and a full wash-off by $U/\Delta = 3.0$ and the same regime of voltages. For small value of V/U, the changes to any component of Σ are barely noticeable, except at small frequencies, where they still remain small, regardless of interaction strength U/Δ.

The FDT condition $\mathrm{Re}\Sigma^K \stackrel{!}{=} 0$ is more strongly violated for larger bias voltages. However, these contributions remain negligible, at absolute values of order 10^{-11} and, hence, deserve no further comment.

Note that, regardless of interaction strength, results for $V/U \geq 1$ show self-energy components with washed-off features, in strong contrast to what we see for $V/U < 0.1$, where the objects barely change with respect to their equilibrium counterparts. This points

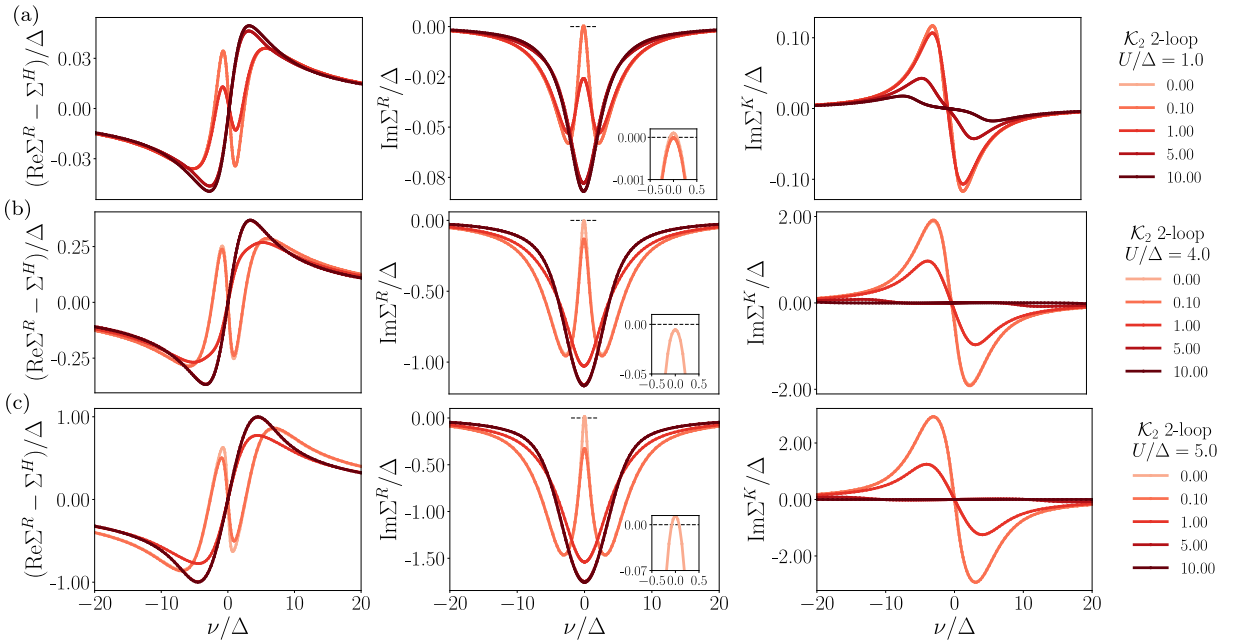

Figure 5.11: Variable voltage results for Σ. Note the strong smearing effect that $V \neq 0$ has on the features of the self-energy. Legend gives V/U.

to a low/high V/U behavior of the system. Particularly the fact that $\mathrm{Im}\Sigma^K(\nu = 0)$ change so drastically, from a value close to zero for $V/U < 0.1$ to a relatively large value for $V/U > 1$ indicates that the behavior of the system changes and that transport through the dot becomes the driving force behind the behavior of the system. Hence we recognize in our results a low V/U-regime, in which transport through the dot is unimportant or does not effectively drive the system to a state outside of equilibrium, i.e. an interaction-driven regime, where U/Δ dictates the behavior, and a high V/U-regime, in which transport through the impurity due to the bias voltage and the onset of decoherent processes are the driving factors..

This is also reflected in Fig. 5.12, for which we see that the spectral function reflects small changes for small values of V/U and a dramatic broadening of the central peak for $V/U > 1$, evidencing the effect of decoherent processes due to a large voltage. As in the equilibrium case, in the non-equilibrium calculations we do not see the formation of clear Hubbard bands, probably again because of the omission of the $\mathcal{K}_3$ class. One also expects the central resonance to split into two well-defined, symmetrically-placed peaks at large values of V/U. We also do not observe this behavior, which we suspect is due to the same factor as before.

Before passing onto the conclusion of this work we point out that we also performed calculations at different temperatures to see how these compare with the standard we defined at $T = 0.01$. We note that our calculations for variable temperature do *not* constitute results outside of thermodynamic equilibrium, since we set $V = 0$ and we take both leads to be at the same temperature. However, we present them here, after results

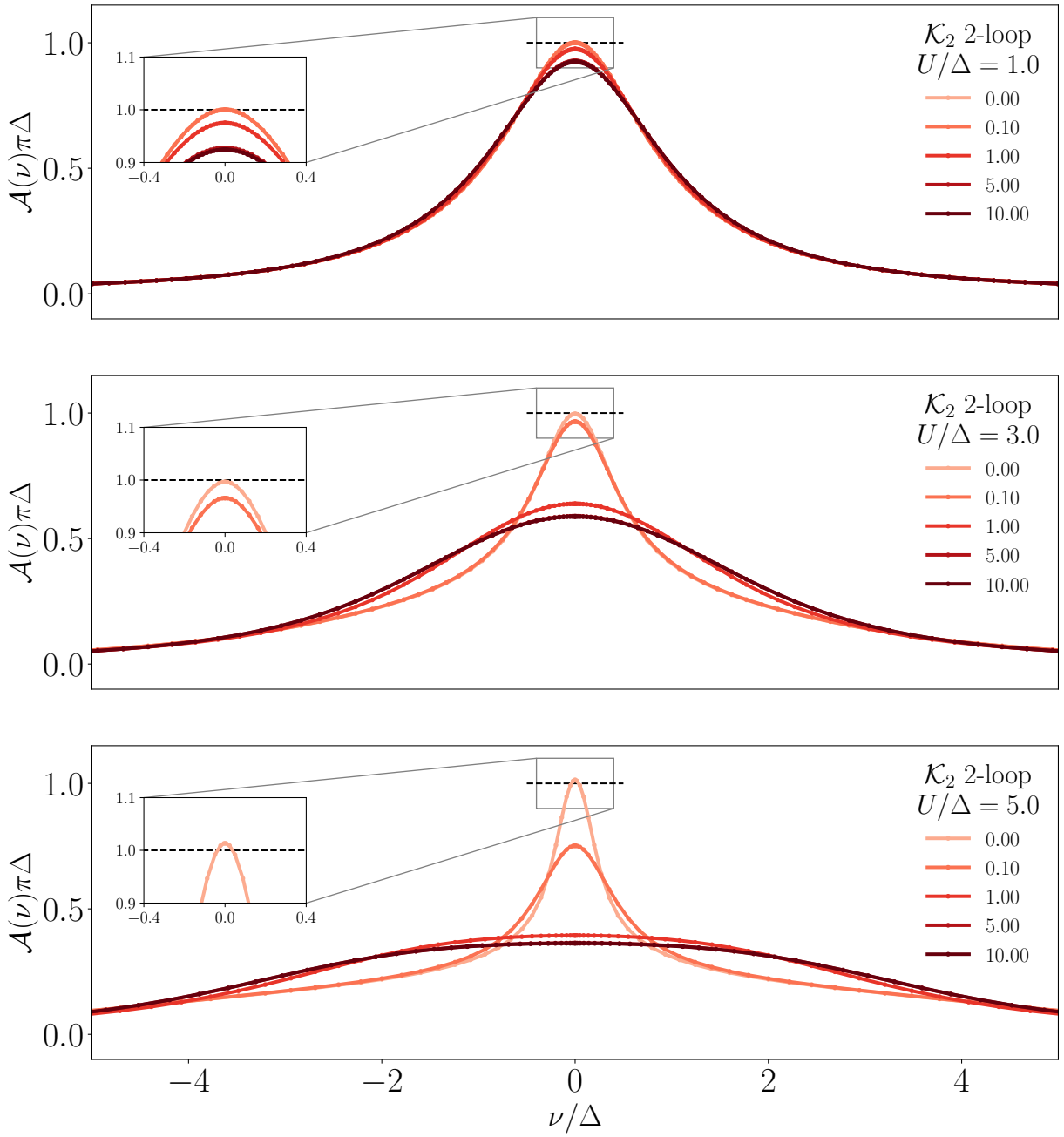

Figure 5.12: Variable voltage results for t$\mathcal{A}$ at different values of U/Δ. Legend gives V/U.

of variable V have been presented, to verify that temperature increase also has a similar smearing effect as the voltage, due to the increased number of decoherent processes it causes. As can be seen in Fig. 5.13, increasing the temperature simply washes-off and broadens the features seen in the plots above but show no behavior of particular interest.

A more interesting goal would be to enhance the code to probe Kondo physics at much lower temperatures. However, due to the discreteness associated to the frequency grid, if the density of points around $\nu = 0$ or $\omega = 0$ is not drastically increased, a fictitious temperature of the order of the difference

$$\delta\omega = \omega_{(N_{\mathrm{bos/fer}}-1)/2+1} - \underbrace{\omega_{(N_{\mathrm{bos/fer}}-1)/2}}_{=0} \tag{5.9}$$

is artificially introduced. Therefore, a high-enough density of points, in accordance to T_K, which decreases exponentially in U, is needed to probe this physics. The problem is then that we would need to be able to reliably and efficiently reach higher values of U/Δ as we currently do, so that T_K becomes significantly smaller than all other energy scales. Note that these are very technical aspects that make it extremely hard numerically probing the Kondo scale with an mfRG code. This goal remains well outside of our current reach, but could become a feasible goal once other technical hurdles are overcome.

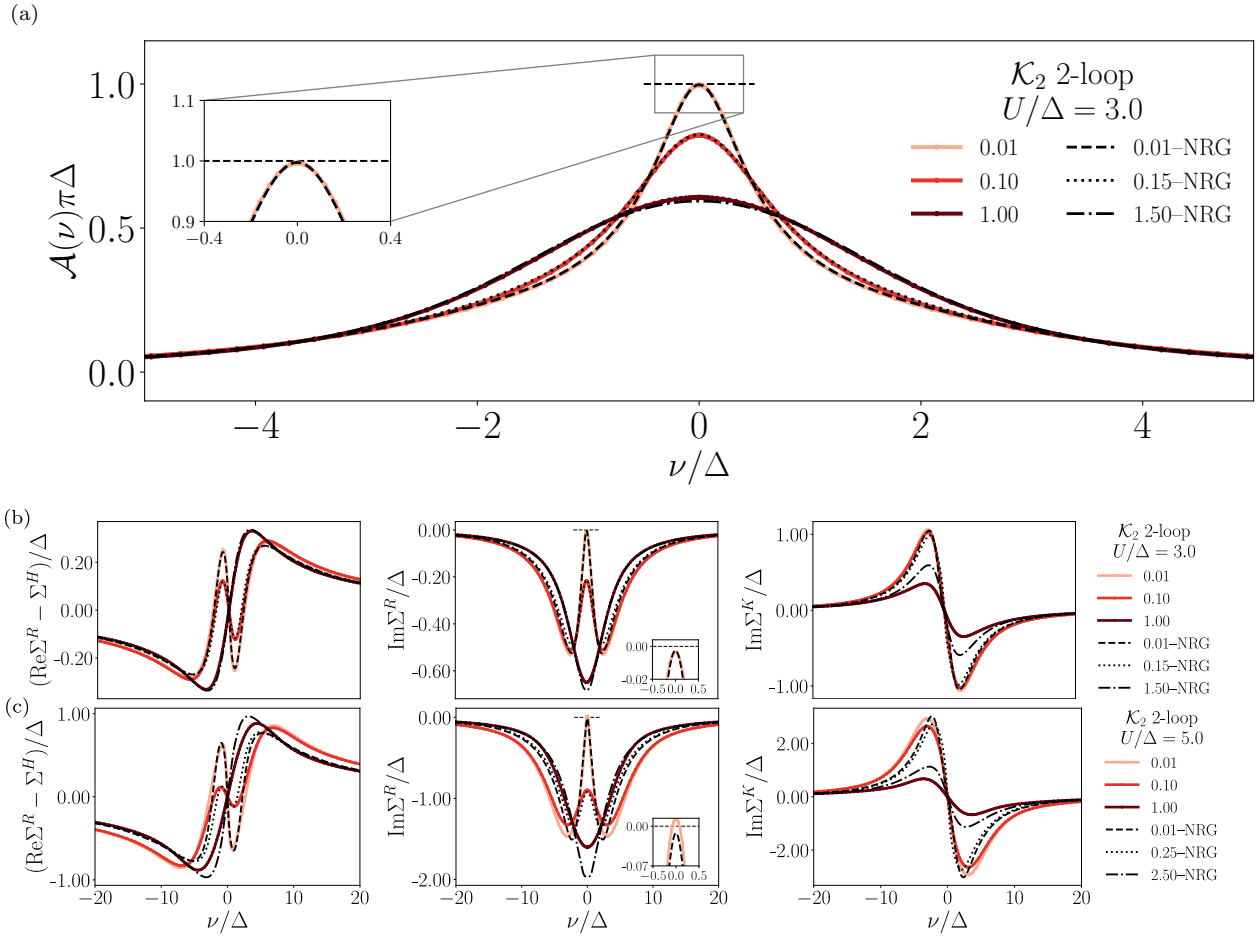

Figure 5.13: Variable temperature results for the spectral function at $U/\Delta = 3.0$ and the self-energy at $U/\Delta = 3.0$ and $U/\Delta = 5.0$. Legend gives T/U.

Chapter 6

Conclusion & Outlook

In this thesis we developed a code to perform calculations of a quantum impurity in the Keldysh formalism using the newly developed multiloop functional renormalization group. To this purpose, we thoroughly studied the internal structure of the vertex, its decomposition into interaction channels and diagrammatic classes and, most crucially, the interplay these structures have with its internal Keldysh structure. Furthermore, we tested and benchmarked this code against NRG, analyzed how well it solves the equations of the parquet formalism and looked at how violation of Ward identities is improved on. Lastly, we presented variable bias voltage results including a vertex function with complete frequency parametrization which had, to our knowledge, not yet been done.

Although the results we showed do not include the $\mathcal{K}_3$ class and are therefore preliminary, we can confidently say that the mfRG does prove to be a major improvement on the fRG. We observed that calculations performed using both the complete frequency parametrization of the vertex as well as the multiloop corrections to the flow equation of the vertex fare consistently better than both the conventional fRG as well as the common simplification of static-feedback approximation [6]. The latter we showed to have very large problems when calculating the vertex itself, regardless of the regime of interaction strengths, but remains as interesting and useful tool due to the low computation times it offers in comparison to more complex approaches.

We observe our results for $\mathcal{K}_2$ 2-loop flows to behave according to expectations, improving both on the fulfillment of Ward identities as well as on the solution of the self-consistent parquet equations. It also increases the range of interaction strengths at which the mfRG can reliably be applied, in comparison to conventional fRG. We also see that our results outside of thermodynamic equilibrium conform with expectations. Though not definitive, this achievement gives us confidence in the range of applicability of a Keldysh mfRG code.

Notably, though we see our method already deliver an improvement in comparison to the conventional methods, we remark that these are only partial results of a much larger project. As noted several times in the last chapter, several improvements at technical and physical level must still be done for the project to be complete. The first on the technical side is the implementation of an adaptive frequency grid. With it we should be able to include all relevant features inside of the sampling intervals at every step of the flow and,

hence, avoid unphysical behaviors due to lack of resolution of the high-frequency regime. Furthermore, a grid of this kind allows for a reduction of the number of needed sampling points, which is a major concern for the success of this project, since the computation times of the $\mathcal{K}_3$ class scale dramatically faster than those we saw for the results presented here.

A more physical improvement, which could be done still at the level of numerical complexity of the $\mathcal{K}_2$ class, is the support for a higher number of loops than two. Currently, our code does not support calculations of the type required by the central term in the multiloop corrections of the flow equations (recall Eq. (2.25)), since some intermediate vertex-objects needed for the typical computation strategy of center terms through either left or right differentiated ones poses additional difficulties. The reason is that these auxiliary objects turn out *not* to fully respect the symmetries discussed in Chapter 3. Implementation of a class of `vertex`-type that does not explicitly need these transformations is planned, but not yet underway.

Another physical improvement which will be tackled in the future is the initialization condition. Though good enough for our benchmarking goals, initializing the flow from a second-order perturbation theory calculation has some deficiencies. Doing this leads to large discrepancies in the $\mathcal{K}_2$ class of the flowing results with respect to those yielded by the parquet equations. A similar phenomenon would also be observed for the $\mathcal{K}_3$ class. Hence, implementation of an initialization code that guarantees a parquet-consistent starting point would be a good step forward.

An interesting point of inquiry that arises from our results is if there are still some simplifications and symmetries to be made use of, at least in the particle-hole symmetric case. We see the number diagrammatic classes reduce by one in the $\mathcal{K}_1$ level, which has huge impacts on the computation times of this class. Whether a similar identity holds for the more complex classes, at least in this special case of particle-hole symmetric systems, is a matter that deserves attention, both from the numerical as from the analytical perspective.

Through inclusion of the multiloop corrections, the mfRG promises to restore both one-particle conservation laws as well as regulator independence. Further work on this project could be to compare how different regulators behave along the flow and to test for fulfillment of conservation laws and of Ward identities as more loops are calculated. A hint of checks of the latter kind was given in Sec. 5.2.5, but certainly a lot more can be done and investigated in this direction.

More ambitious projects that can follow and build on this one include the application of these kinds of treatments to more complex, extended systems. This could encompass Luttinger liquids, thanks to their interesting behavior in perturbative regimes yet relative simplicity thanks to translation invariance, quantum point contacts, thought of as 1D-chains of interacting impurities, and studies of many-body localization, where interactions and disorder freeze out the dynamics and the system never thermalizes.

Beyond these systems, there are multiple fields of study in which a Keldysh mfRG framework can be a powerful tool of study. These include, particularly, two fields. The first one is that of pseudofermion-fRG, a field in which some advances have been made in the Matsubara formalism [32]. Here, a Keldysh mfRG code can provide the possibility of

calculation dynamical quantities directly, which is not possible in the Matsubara formalism. The second is the combination of mfRG with the well-known dynamical mean-field theory (DMFT), expanding the already existing DMF^{2}RG to include the multiloop corrections. This union would improve heavily on the restrictive PA approximation. This mixed framework can provide an initialization of the irreducible part of the vertex calculated within DMFT, instead of truncating it to equal the bare vertex. These various possibilities make of the mfRG a potentially very powerful tool of study, which is a statement backed by the results we show in here. This work should be regarded as a first step into the development of a tool capable of treating those more physically rich systems.

Appendix A

Group structure of the vertex's internal symmetries

In Chapter 3 we introduce transformations T_1, T_2, T_3, T_C and T_S as operations that can be performed simultaneously to the Keldysh and spin indices. As such, this set of operations can be thought of as a group of symmetries $\mathcal{S}$, where we understand these symmetries as an equivalence between the vertex evaluated at different combinations of Keldysh and spin indices and at different frequencies. Here we study the internal structure of $\mathcal{S}$, independently of the dependencies between vertex components it causes.

To fulfill the axioms of a group, we introduce the trivial transformation T_0, which is our identity element. Through Eqs. 3.27a-3.27e, we see that each one of these has order 2, which means $T_k^2 = T_0$, $\forall k \in \{1, 2, 3, C, S\}$ and every one of these is its own inverse.

In terms of actions on the Keldysh and/or spin indices of the vertex, it is clear that at least fours different possibilities exist, namely exchange of incoming (T_1) and outgoing (T_2) indices among themselves, exchange of incoming and outgoing with one another (T_C) and only flipping on kind of index (T_S, with spin). Notice this is exhaustive due to σ_i and α_i taking values in fields of characteristic two.

We now look at the existing sub-groups. Almost trivially, due to the order of each generator being two,

$$g_k := \langle T_0, T_k \rangle = \{T_0, T_k\} < \mathcal{S}\,, \forall k \in \{1, 2, C, S\}\,, \tag{A.1}$$

i.e. each generator together with the identity generates its own subgroup, which we call g_k. Notice that $g_k \cap g_{k'} = \{T_0\}\,, \forall k \neq k'$.

Motivated by the action $T_{1/2}$ have on incoming/outgoing legs, we now consider

$$K := \langle T_0, T_1, T_2 \rangle = \{T_0, T_1, T_2, T_3 = T_1 \circ T_2 = T_2 \circ T_1\}\,. \tag{A.2}$$

Since the action of T_1 and T_2 is on non-overlapping indices, it is clear that these commute and, hence $|K| = 4$. Further,

$$\begin{aligned} T_3 \circ T_3 &= (T_1 \circ T_2) \circ (T_1 \circ T_2) \\ &= T_1 \circ \underbrace{T_2 \circ T_2}_{T_0} T_1 \\ &= T_1 \circ T_1 = T_0 \end{aligned} \tag{A.3}$$

proves that T_3 also has order 2. Thus K is isomorphic to the Klein group K_4 [33]. This is reasonable, since $K_4 = \{(), (1,2)(3,4), (1,3)(2,4), (1,4)(2,3)\}$ as permutations and this is exactly what the operations T_0, T_1, T_2 and T_3 do on the Keldysh and spin indices of the vertex.

We now analyze the inclusion of T_C. To this end, we consider the abstract action of the T_i's as permutations on a set of cardinality 4. Expressing Eqs. 3.27b-3.27e like this, we obtain

$$T_1(1234) = (1243) \tag{A.4a}$$
$$T_2(1234) = (2134) \tag{A.4b}$$
$$T_3(1234) = (2143) \tag{A.4c}$$
$$T_C(1234) = (3412)\,. \tag{A.4d}$$

Thus, we see that

$$T_1 \circ T_C(1234) = T_1(3412) = (3421) \tag{A.5a}$$
$$T_C \circ T_2(1234) = T_C(2134) = (3421)\,, \tag{A.5b}$$

and

$$T_2 \circ T_C(1234) = T_2(3412) = (4312) \tag{A.6a}$$
$$T_C \circ T_1(1234) = T_C(1243) = (4312)\,. \tag{A.6b}$$

Thus, $T_C \circ T_1 = T_2 \circ T_C$ and $T_C \circ T_2 = T_1 \circ T_C$. These relations imply that the inclusion of T_C makes the group non-abelian i.e. T_C does not commute with T_1 or T_2. However it does commute with T_3, since

$$T_3 \circ T_C = T_1 \circ T_2 \circ T_C = T_1 \circ T_C \circ T_1 = T_C \circ T_2 \circ T_1 = T_C \circ T_3\,. \tag{A.7}$$

Hence we obtain the symmetry group of a spinless vertex

$$H = \langle T_0, T_1, T_C \rangle = \{T_0, T_1, T_2, T_3, T_1 \circ T_C, T_2 \circ T_C, T_3 \circ T_C\}\,. \tag{A.8}$$

Equations A.5 and A.6 imply then, that one can always permute T_C to be the first or the last operation performed, which is useful when implementing the relations of Tables 3.1 to 3.5 in a code. This further leads to rendering T_2 unnecessary as generator, since

$$T_C \circ T_1 \circ T_C = T_2 \circ T_C \circ T_C = T_2\,. \tag{A.9}$$

As such, $|H| = 8$ and is non-abelian and has exactly three generators. Hence, it is isomorphic to the Dihedral group of order 8 D_8 [33].

The inclusion of T_S is trivial, since is affects the spin indices of the vertex in a completely different way than the others transformations do. Hence, the full group is

$$\mathcal{S} = \langle T_0, T_1, T_C, T_S \rangle = H \times \{T_S\} \,. \tag{A.10}$$

T_S clearly commutes with all elements and, hence, is the only non-trivial element in the center of the group. $|\mathcal{S}| = 16$ and is, as is H, non-abelian. Due to the multiplicative structure of $\mathcal{S}$ with $g_S \simeq \mathbb{Z}_2$ [33],

$$\mathcal{S} \simeq D_8 \times \mathbb{Z}_2 \simeq G_{16}^{11} \,. \tag{A.11}$$

Since we are interested in an efficient implementation of the symmetries of the vertex, we restrict the number of symmetry operations to be performed by two, i.e. we allow combinations of the generators of $\mathcal{S}$ up to length two. Hence, expressions of the form $T_1 \circ T_C \circ T_1 \equiv T_2$ can only be included if one considers T_2 as a generator. Hence, we regard it as such in the discussion of Chap. 3.

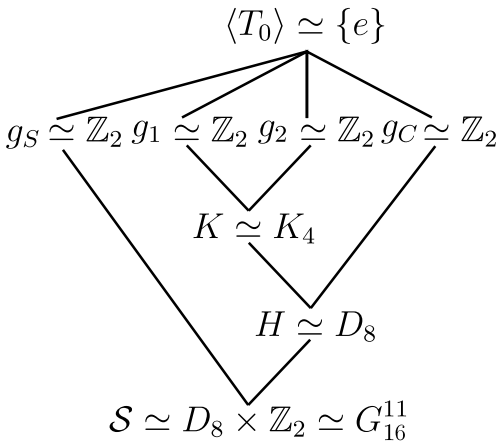

Figure A.1: Simplified graph of the subgroup structure of $\mathcal{S}$. Notice this is not exhaustive and illustrates only the dependencies and inclusions relevant for our work.

Appendix B

Recipe for an object-oriented Keldysh mfRG code

The present Appendix aims to be a guide to building up, testing and maintaining a code like ours from scratch. Based on our experience, gained over the year and a half that Elias Walter and myself have been working on the code, we present a step-by-step suggestion on how to approach the task of setting up a Keldysh mfRG code.

According to the problems and hurdles we had to overcome, we firmly believe that modularity, testability and simplicity are the cornerstones of a good code. For a very good introduction into these and also other extremely helpful concepts, we refer the reader to [34]. Modularity helps the code to be separated into coherent, cohesive units, that are conceptually linked and, roughly, at the same level of abstraction. We strongly suggest keeping these distinct layers separated from one another e.g. the `State` class is in its own file, which imports code from separated files for the `self-energy` and for the `fullvert`. Testability can be understood as the ability to test any function implemented, as well as its interplay with functions that will be using the outputs of it. We learned the hard way that, at the complexity level of a Keldysh mfRG code, one that cannot be properly and simply tested, function by function and module by module, is not useful. As stated in [34], implementation tests should be implemented *before* the function it is supposed to verify is written. Furthermore, there should be tests for each function and each module and all of them should be quick to run. Lastly, simplicity is needed to keep a reasonable overview of the code. In our experience, a long code is a breeding ground for bugs. Keeping the functions as short as possible and reducing the number of modules as much as the physics allows helps debugging processes, since there are less lines of code in which there can be a mistake. A golden rule any coder should abide by is "*never copy and paste code*". However simple, these three principles can make the process of setting up such a code an easier task. For other helpful yet more general principles, we seriously encourage the reader to take a look at [34]. At a certain point in code complexity, which lies below the one a Keldysh mfRG code has, strongly adhering to principles of software engineering becomes a necessity rather than a choice.

Having said this, we now discuss our proposed implementation order. It should be evident that not all modules can be implemented at the same time and that there are better orders than others to do this.

1. Basic data structures module. For instance, C++ does not provide a fast-and-easy way to handle vectors of complex numbers or to operate them.

2. Simple data-output module. As stated in Chap. 4, we use HDF5 to write out our results based on the structure of the `State` class, the most complex class we have in terms of dependencies. Hence, having a way to quickly output data produced by the code, in the format that will be used for the whole project, turns out to be extremely helpful.

3. Integrator. The integrator is one of the most important parts of out code and, with certainty, of any implementation of a Keldysh mfRG. Crucially, it must be adaptive, since a static integrator has been proven, time and again, to be too slow and inefficient to accurately, reliably and correctly resolve sharp features of strongly peaked integrands. In our experience, no results can be trusted until there is full confidence in the stability of the integrator. It should not be tailored for a specific kind of integrand but should be as flexible as possible. Implementing this module early makes sense for testing purposes.

4. Interpolation and general functionality functions. 1-, 2- and 3-dimensional interpolators for given grids of points, as well as functions that generate these sampling grids in a standard manner should be implemented next. General functionality functions include also ones of the sort of $n_F(\nu) = (\exp((\nu-\mu)/T)+1)^{-1} \equiv \frac{1}{2}(1-\tanh((\nu-\mu)/2T)$. Notice that with functions like this there are issues of numerical stability of the implementation that need to be taken into account [30].

5. Basic, independent modules. As was discussed in Chap. 4 and is shown in Fig. B.1, there are some classes that do *not* depend on any other module or structure other than the basic ones and, hence, should be implemented next. These include the `self-energy` as well as the `rverts` and the `irreducible` vertices. In our case, the implementation of the `rverts` proved to be one of the most difficult tasks.

6. More complex classes. With the simplest classes implemented, the classes that directly depend on these can then be implemented. These include the `propagator` and `bubble` as well as the `fullvert` classes in our implementation.

7. Wrapper classes and actual data-output module. Implementation of the most complex class, the `State`, should, of course, happen at the end. Once this is taken care of, the whole skeleton of the code stands and then the main functions should be implemented.

8. `loop` and `bubble` functions. The implementation of these functions should be as short as possible, taking advantage of both OpenMP and MPI parallelization whenever

reasonable and possible. Although only relevant at this stage, parallelization plays an important role in the whole code, since the basic structures should be compatible with both schemes, if one wants to take advantage of both.

9. ODE-integrator. Once a `State` can be computed, then the integration of the ODE is in order. In our experience, at least a conventional 4^{th}-order Runge–Kutta is necessary. An adaptive ODE-integrator helps optimize the overall performance of the code but its, however, not a must in a first implementation. The same comment applies to frequency grids. However, as this is ultimately the required kind of tools, the implementation should be aimed to support an upgrade with the least amount of effort. Notably, a modular approach yields naturally a structure compatible with this.

10. Checks. Here we do not mean implementation or unit tests, which should be implemented alongside the modules, but physical checks for the results produced. These can include tests for fulfillment of the parquet equations or of Ward identities. It is much more efficient to program these in a low-level language, as C++ , as have them in a higher-level language as, e.g. Python.

To better illustrate the dependencies described here, we present Fig. B.1.

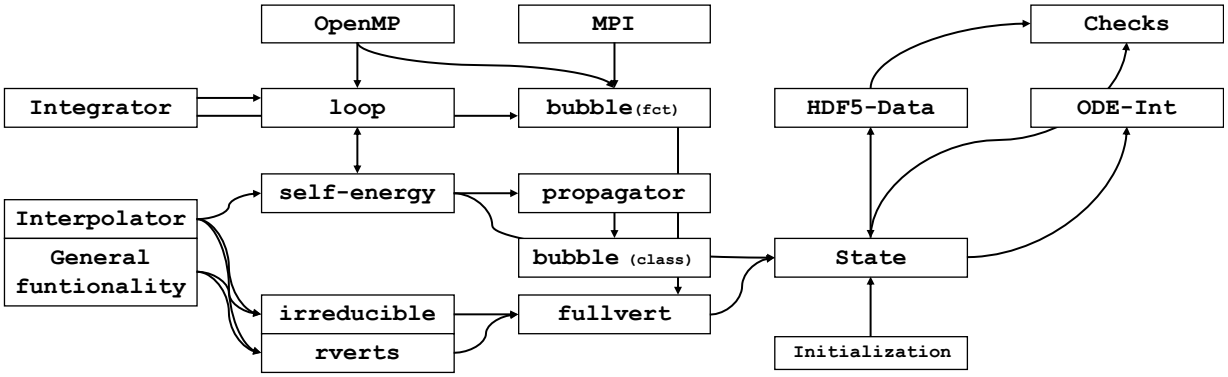

Figure B.1: Visualization of the structure of our implementation. We omit the basic data structure module, since it is embedded into the implementation of all other modules, and the basic.

Certificate of authorship

I, Santiago Aguirre Lamus, hereby certify that the present work is my own original work. Whenever external input was used or needed, it has been dully cited.

Munich, the 14$^{\text{th}}$ of October, 2020

Santiago Aguirre Lamus

Bibliography

[1] Fabian B. Kugler and Jan von Delft. "Multiloop functional renormalization group for general models". In: *Phys. Rev. B* 97 (3 Jan. 2018), p. 035162. DOI: 10.1103/PhysRevB.97.035162. URL: https://link.aps.org/doi/10.1103/PhysRevB.97.035162.

[2] Fabian B. Kugler and Jan von Delft. "Multiloop functional renormalization group that sums up all parquet diagrams". In: *Phys. Rev. Lett.* 120 (5 Jan. 2018), p. 057403. DOI: 10.1103/PhysRevLett.120.057403. URL: https://link.aps.org/doi/10.1103/PhysRevLett.120.057403.

[3] Agnese Tagliavini et al. "Multiloop functional renormalization group for the two-dimensional Hubbard model: Loop convergence of the response functions". In: *SciPost Phys.* 6 (1 2019), p. 9. DOI: 10.21468/SciPostPhys.6.1.009. URL: https://scipost.org/10.21468/SciPostPhys.6.1.009.

[4] Cornelia Hille et al. "Quantitative functional renormalization group description of the two-dimensional Hubbard model". In: *Phys. Rev. Research* 2 (3 Sept. 2020), p. 033372. DOI: 10.1103/PhysRevResearch.2.033372. URL: https://link.aps.org/doi/10.1103/PhysRevResearch.2.033372.

[5] Nils Wentzell et al. "High-frequency asymptotics of the vertex function: diagrammatic parametrization and algorithmic implementation". In: *Phys. Rev. B* 102 (8 Aug. 2020), p. 085106. DOI: 10.1103/PhysRevB.102.085106. URL: https://link.aps.org/doi/10.1103/PhysRevB.102.085106.

[6] Severin Jakobs. "Functional renormalization group studies of quantum transport through mesoscopic systems". PhD thesis. RWTH Aachen, Dec. 2010.

[7] Severin G. Jakobs, Mikhail Pletyukhov, and Herbert Schoeller. "Nonequilibrium functional renormalization group with frequency-dependent vertex function: A study of the single-impurity Anderson model". In: *Phys. Rev. B* 81 (19 May 2010), p. 195109. DOI: 10.1103/PhysRevB.81.195109. URL: https://link.aps.org/doi/10.1103/PhysRevB.81.195109.

[8] Walter Metzner et al. "Functional renormalization group approach to correlated fermion systems". In: *Rev. Mod. Phys.* 84 (1 Mar. 2012), pp. 299–352. DOI: 10.1103/RevModPhys.84.299. URL: https://link.aps.org/doi/10.1103/RevModPhys.84.299.

[9] P. Strack, R. Gersch, and W. Metzner. "Renormalization group flow for fermionic superfluids at zero temperature". In: *Phys. Rev. B* 78 (1 July 2008), p. 014522. DOI: 10.1103/PhysRevB.78.014522. URL: https://link.aps.org/doi/10.1103/PhysRevB.78.014522.

[10] S. Andergassen et al. "Functional renormalization group for Luttinger liquids with impurities". In: *Phys. Rev. B* 70 (7 Aug. 2004), p. 075102. DOI: 10.1103/PhysRevB.70.075102. URL: https://link.aps.org/doi/10.1103/PhysRevB.70.075102.

[11] Peter Kopietz, Lorenz Bartosch, and Florian Schütz. *Introduction to the functional renormalization group*. 798. Springer-Verlag Berlin Heidelberg, 2010. DOI: 10.1007/978-3-642-05094-7.

[12] Kenneth G. Wilson. "The renormalization group: critical phenomena and the Kondo problem". In: *Rev. Mod. Phys.* 47 (4 Oct. 1975), pp. 773–840. DOI: 10.1103/RevModPhys.47.773. URL: https://link.aps.org/doi/10.1103/RevModPhys.47.773.

[13] Leonid V. Keldysh. "Diagram technique for nonequilibrium processes". In: *J. Exp. Theor. Phys.* 20 (4 1965), pp. 1018–1026.

[14] Alex Kamenev. *Field theory of non-equilibrium systems*. Cambridge University Press, 2011. DOI: 10.1017/CBO9781139003667.

[15] P. W. Anderson. "Localized magnetic states in metals". In: *Phys. Rev.* 124 (1 Oct. 1961), pp. 41–53. DOI: 10.1103/PhysRev.124.41. URL: https://link.aps.org/doi/10.1103/PhysRev.124.41.

[16] Kosaku Yamada. "Perturbation expansion for the Anderson Hamiltonian. II". In: *Prog. Theor. Phys.* 53 (4 Apr. 1975), pp. 970–986. DOI: https://doi.org/10.1143/PTP.53.970. URL: https://academic.oup.com/ptp/article/53/4/970/1925516.

[17] Kei Yosida and Kosaku Yamada. "Perturbation Expansion for the Anderson Hamiltonian. III". In: *Progress of Theoretical Physics* 53.5 (May 1975), pp. 1286–1301. ISSN: 0033-068X. DOI: 10.1143/PTP.53.1286. eprint: https://academic.oup.com/ptp/article-pdf/53/5/1286/5156622/53-5-1286.pdf. URL: https://doi.org/10.1143/PTP.53.1286.

[18] Kosaku Yamada. "Perturbation Expansion for the Anderson Hamiltonian. IV". In: *Progress of Theoretical Physics* 54.2 (Aug. 1975), pp. 316–324. ISSN: 0033-068X. DOI: 10.1143/PTP.54.316. eprint: https://academic.oup.com/ptp/article-pdf/54/2/316/5180357/54-2-316.pdf. URL: https://doi.org/10.1143/PTP.54.316.

[19] Fabian Kugler and Jan Delft. "Derivation of exact flow equations from the self-consistent parquet relations". In: *New J. of Phys.* 20 (Dec. 2018). DOI: 10.1088/1367-2630/aaf65f.

[20] G. Rohringer, A. Valli, and A. Toschi. "Local electronic correlation at the two-particle level". In: *Phys. Rev. B* 86 (12 Sept. 2012), p. 125114. DOI: 10.1103/PhysRevB.86.125114. URL: https://link.aps.org/doi/10.1103/PhysRevB.86.125114.

[21] A. A. Katanin. "Fulfillment of Ward identities in the functional renormalization group approach". In: *Phys. Rev. B* 70 (11 Sept. 2004), p. 115109. DOI: 10.1103/PhysRevB.70.115109. URL: https://link.aps.org/doi/10.1103/PhysRevB.70.115109.

[22] David Senechal, Andre-Marie Tremblay, and Claude Bourbonais. *Theoretical methods for strongly correlated electrons*. Springer-Verlag New York, 2004. DOI: 10.1007/b97552.

[23] Y. M. Vilk and A.-M.S. Tremblay. "Non-perturbative many-body approach to the Hubbard model and single-particle pseudogap". In: *J. Phys. I France* 7 (11 July 1997), pp. 1309–1368. DOI: https://doi.org/10.1051/jp1:1997135. URL: https://jp1.journaldephysique.org/articles/jp1/abs/1997/11/jp1v7p1309/jp1v7p1309.html.

[24] Dennis Hank Schimmel. "Transport through inhomogeneous interacting low-dimensional systems". PhD thesis. Ludwig-Maximilians-Universität, Nov. 2017.

[25] Julian Thönniß. "Multiloop functional renormalization group studies of Heisenberg models on the Kagome lattice". MA thesis. Ludwig-Maximilians-Universität, Sept. 2019.

[26] William H. Press et al. *Numerical recipes in C++*. 2nd ed. Cambridge University Press, 2002.

[27] J. M. Ziman. *Principles of the theory of solids*. 2nd ed. Cambridge University Press, 1972. DOI: 10.1017/CBO9781139644075.

[28] Mehran Kardar. *Statistical Physics of Fields*. Cambridge University Press, 2007. DOI: 10.1017/CBO9780511815881.

[29] *Correlated electrons: from models to materials*. Lecture notes of the Autumn School Correlated Electrons 2012. Sept. 2012. URL: https://www.cond-mat.de/events/correl12/manuscripts/correl12.pdf.

[30] Reinhard Leidl. *M4: Numerische Mathematik für Studierende der Physik (SoSe2020)*. Lecture notes on the course for Numerical Mathematics for Physicists. Aug. 2020. URL: https://uni2work.ifi.lmu.de/course/S20/MI/NuMaM4/file/Vorlesungsskript%20Gesamtversion/download/NuMa_SoSe2020_Gesamt.pdf.

[31] Alexander Altland and Ben D. Simons. *Condensed matter field theory*. 2nd ed. Cambridge University Press, 2010. DOI: 10.1017/CBO9780511789984.

[32] Finn Lasse Buessen and Simon Trebst. "Competing magnetic orders and spin liquids in two- and three-dimensional kagome systems: Pseudofermion functional renormalization group perspective". In: *Phys. Rev. B* 94 (23 Dec. 2016), p. 235138. DOI: 10.1103/PhysRevB.94.235138. URL: https://link.aps.org/doi/10.1103/PhysRevB.94.235138.

[33] A. Zee. *Group theory in a nutshell for physicists*. In a Nutshell. Princeton University Press, 2016. ISBN: 9780691162690. URL: https://books.google.de/books?id=DmuYDwAAQBAJ.

[34] Roobert C. Martin. *Clean code: a handbook of agile software craftmanship*. Clean Code. Prentice Hall, Aug. 2008. ISBN: 9780136083238.